

Investigation of Two-Dimensional Electron Gases with Angular Resolved Photoemission Spectroscopy

THÈSE N° 4970 (2011)

PRÉSENTÉE LE 31 MARS 2011

À LA FACULTÉ SCIENCES DE BASE

LABORATOIRE DE SCIENCE À L'ÉCHELLE NANOMÉTRIQUE

PROGRAMME DOCTORAL EN PHYSIQUE

ÉCOLE POLYTECHNIQUE FÉDÉRALE DE LAUSANNE

POUR L'OBTENTION DU GRADE DE DOCTEUR ÈS SCIENCES

PAR

Isabella GIERZ

acceptée sur proposition du jury:

Prof. V. Savona, président du jury

Prof. K. Kern, directeur de thèse

Prof. R. Fasel, rapporteur

Prof. K. Horn, rapporteur

Prof. D. Pavuna, rapporteur



ÉCOLE POLYTECHNIQUE
FÉDÉRALE DE LAUSANNE

Suisse
2011

Abstract

In this thesis we study the electronic structure of different two-dimensional (2D) electron systems with angular resolved photoemission spectroscopy (ARPES). This technique is based on the photoelectric effect and directly probes the electronic structure of a system. By carefully analyzing the measured band structure with respect to peak position and line width we can determine the complex self-energy Σ that describes the renormalization of the electron's energy and the change in lifetime due to many-body interactions.

The 2D electron systems investigated in this work are surface alloys on Ag(111), bismuth trimers on Si(111) and epitaxial graphene monolayers grown on SiC(0001). Surface alloys on Ag(111) are formed by depositing 1/3 of a monolayer of bismuth, lead or antimony (alloy atoms) on the clean silver surface. Although (Bi,Pb,Sb) and Ag atoms are immiscible in the bulk they form long-range ordered surface alloys, where every third Ag atom is replaced by an alloy atom. These systems as well as the Bi trimers on Si(111) show a spin splitting of the 2D band structure due to the Rashba-Bychkov (RB) effect. The RB model states that in a symmetry broken environment (such as the surface of a semi-infinite crystal) the spin-orbit interaction will lift the spin-degeneracy of the band structure. Such a spin-split band structure bares great potential for applications in the field of spintronics, e.g. in a Datta-Das spin field effect transistor. In the present work we investigate the origin of the observed giant spin splitting in surface alloys, especially the interplay between structural parameters and the atomic spin-orbit interaction. Furthermore, we will show that it is possible to transfer these concepts to a semiconducting substrate, which is better suited for spintronics applications.

The third system under investigation — graphene — is an ideally two-dimensional crystal. It consists of a single layer of carbon atoms arranged in a honeycomb lattice, and its charge carriers are confined within a plane that is just one atom thick. These charge carriers behave like massless Dirac particles and possess extremely high carrier mobilities. This makes graphene a promising material system for high-speed electronic devices. In order to reach this ambitious goal one needs reliable methods for the large-scale production of high quality graphene films. Epitaxial growth on silicon carbide (0001) substrates is the method of choice in this case, as it offers the advantage of a precise thickness control and a semiconducting substrate at the same time. However, the presence of the substrate reduces the carrier mobility of graphene's charge carriers considerably. Therefore, it is necessary to decouple the graphene layer from the substrate after epitaxial growth. A second issue that needs to be addressed, are viable doping methods for graphene. As graphene's peculiar band structure results from a sensible interplay between electrons and crystal lattice it is not an option to replace single atoms of the graphene lattice by dopants as is common practice when doping silicon. In order to preserve its band structure, graphene is usually doped by adsorbing atoms or molecules on its surface. As graphene grown on SiC is n-doped due to charge transfer from the substrate, appropriate means for p-type doping are clearly required. In this thesis, we will present a new growth method for quasi free-standing graphene on SiC(0001) and viable means for p-type doping.

Keywords: ARPES
two-dimensional electron systems
surface alloys
graphene
Rashba-Bychkov effect
spintronics
doping
decoupling

Zusammenfassung

In dieser Arbeit untersuchen wir verschiedene zweidimensionale (2D) Elektronensysteme mit winkelaufgelöster Photoemission. Diese Technik basiert auf dem photoelektrischen Effekt und ermöglicht es direkt die elektronische Struktur eines Materials zu messen. Durch sorgfältige Bestimmung von Peakpositionen und -breiten kann man die komplexe Selbstenergie Σ berechnen, die beschreibt wie sich sowohl die Bindungsenergie als auch die Lebensdauer der Elektronen ändert, sobald diese mit anderen Teilchen wechselwirken.

Hier untersuchen wir die folgenden 2D Elektronensysteme: Oberflächenlegierungen auf Ag(111), Bismuth-Trimere auf Si(111) und epitaktisches Graphen auf SiC(0001). Oberflächenlegierungen auf Ag(111) bilden sich, wenn man 1/3 Monolage Wismuth, Blei oder Antimon (Legierungsatome) auf die saubere Oberfläche aufdampft. Obwohl sich (Bi,Pb,Sb)- und Ag-Atome im Volumen nicht mischen bilden sie eine 2D Oberflächenlegierung mit langreichweitiger Ordnung. Das Besondere an diesen Oberflächenlegierungen und auch den Bi-Trimeren auf Si(111) ist, dass die entsprechende 2D Bandstruktur spinaufgespalten ist. Die Ursache hierfür ist der Rashba-Bychkov Effekt. In einem System, in dem die Rauminversionssymmetrie gebrochen ist (also zum Beispiel an der Oberfläche eines Volumenkristalls), hebt die Spin-Bahn-Wechselwirkung die Spinartung der Zustände auf. Einer solchen spinaufgespaltenen Bandstruktur kommt große Bedeutung zu im Hinblick auf Spintronik-Anwendungen, zum Beispiel in einem Datta-Das Spin-Feldeffekttransistor. In dieser Arbeit untersuchen wir den Ursprung der riesigen Spinaufspaltung in den Oberflächenlegierungen, insbesondere das Zusammenspiel zwischen strukturellen Parametern und der atomaren Spin-Bahn-Wechselwirkung. Außerdem werden wir zeigen, wie sich dieses Konzept auf die Oberfläche eines Halbleiters übertragen lässt, die für elektronische Anwendungen weitaus besser geeignet sind als metallische Substrate.

Das dritte System, das wir im Folgenden untersuchen werden, ist Graphen — ein idealer 2D Kristall. Graphen besteht aus einer einzigen Lage von Kohlenstoffatomen, die ein Honigwabengitter bilden. Die Bewegungsfreiheit der Ladungsträger beschränkt sich hier auf eine Schicht von der Dicke einer einzigen Atomlage. Die Ladungsträger in Graphen verhalten sich als hätten sie keine Masse und haben sehr hohe Beweglichkeiten. Aus diesem Grund ist Graphen ein vielversprechendes Material im Hinblick auf zukünftige sehr schnelle elektronische Anwendungen. Um diese ehrgeizige Ziel zu erreichen müssen allerdings verschiedene Hindernisse überwunden werden. Zuerst einmal benötigt man eine zuverlässige Herstellungsmethode für Graphenfilme mit hoher Qualität. Die Methode der Wahl ist in diesem Fall epitaktisches Wachstum auf einem Siliziumkarbid-Substrat. Das Wachstum auf der Silizium-terminierten Seite des Substrats ermöglicht eine genaue Kontrolle der Filmdicke auf einem halbleitenden Substrat. Allerdings führt der Einfluss des Substrats zu einer erheblichen Verringerung der Beweglichkeit der Ladungsträger. Aus diesem Grund muss das Graphen nach dem Wachstum vom Substrat entkoppelt werden. Ein weiterer wichtiger Aspekt für zukünftige elektronische Anwendungen von Graphen ist eine entsprechende Dotierung. Da die besonderen elektronischen Eigenschaften von Graphen aus einem sensiblen Zusammenspiel zwischen den Elektronen und dem Graphengitter entspringen, kann man nicht einfach einzelne Gitteratome durch Fremdatome ersetzen wie bei der Dotierung von

Silizium. Stattdessen dotiert man Graphen, indem man verschiedene Atome oder Moleküle auf die Oberfläche aufbringt. Da Graphen auf SiC durch Ladungstransfer aus dem Substrat n-dotiert ist, sucht man vor allem nach praktikablen Methoden für die Dotierung mit Löchern. Wir werden im Folgenden unter anderem eine neue Wachstumsmethode für quasi-freistehendes Graphen und eine Methode zur p-Dotierung vorstellen.

Stichwörter: winkelaufgelöste Photoemission
zweidimensionale Elektronensysteme
Oberflächenlegierungen
Graphen
Rashba-Bychkov Effekt
Spintronik
Dotierung
Entkopplung

Contents

1	Introduction	1
2	Scientific background	5
2.1	The two-dimensional electron gas	5
2.1.1	Two-dimensional electron gases in semiconductors	5
2.1.2	Surface states	6
2.1.3	Graphene	7
2.2	The Rashba effect and its applications	12
2.2.1	Spin-orbit interaction	12
2.2.2	The Rashba-Bychkov model	13
2.2.3	Applications of the RB effect	15
2.2.4	Rashba effect on surfaces	17
3	Technical background	21
3.1	Photoemission spectroscopy	21
3.1.1	The photoelectric effect	21
3.1.2	The electron escape depth	21
3.1.3	The photoemission process	22
3.1.4	Quasiparticle picture	25
3.1.5	Angular resolved photoemission spectroscopy	26
3.2	Spin-resolved ARPES	28
3.3	Core level spectroscopy	30
3.4	Low energy electron diffraction	31
3.5	First-principles calculations	35
4	Surface alloys	37
4.1	Atomic contribution to the Rashba splitting	39
4.2	Structural influence on the Rashba splitting	42
4.2.1	Bi/Ag(111)	45
4.2.2	Pb/Ag(111)	46
4.2.3	Sb/Ag(111)	48
4.2.4	Spin Splitting vs. Relaxation	48
4.3	Mixed surface alloys on Ag(111)	50

4.3.1	Binary surface alloy $\text{Bi}_x\text{Sb}_{1-x}/\text{Ag}(111)$	51
4.3.2	Ternary surface alloy $\text{Bi}_x\text{Pb}_y\text{Sb}_{1-x-y}/\text{Ag}(111)$	54
4.4	Conclusion	54
5	Silicon surface with giant spin splitting	57
5.1	Bi on Si(111)	57
5.2	Conclusion	63
6	Discussion: origin of the giant spin splitting	65
6.1	The Au(111) surface state	65
6.2	The atomic spin-orbit coupling	67
6.3	Broken space inversion symmetry	67
6.3.1	Surface potential gradient and electron confinement	68
6.3.2	In-plane inversion asymmetry	69
6.4	Corrugation	70
6.5	Asymmetry of the wave function	71
6.6	Influence of the substrate	72
6.7	Spin splitting in quantum well states	74
6.8	Summary	75
7	Graphene	77
7.1	Atomic hole doping of graphene	78
7.2	Electronic decoupling of epitaxial graphene	85
7.3	Illuminating the dark corridor	93
7.4	Conclusion	103
8	Summary and outlook	105
8.1	Summary	105
8.2	Outlook	106
8.2.1	Rashba effect at surfaces	106
8.2.2	Graphene	106

Chapter 1

Introduction

Towards the end of the 19th century a complete physical description of the universe seemed to be within reach. The two corner stones of classical physics — Newton’s mechanics and Maxwell’s theory of electromagnetism — were able to give satisfactory explanations to most observations. Then, however, many groundbreaking discoveries like e. g. that of the x-rays (Röntgen 1895), of radioactivity (Becquerel 1896) and of the electron (Thomson 1897) revealed the limits of classical physics. With the rise of quantum mechanics and relativity at the beginning of the 20th century it became apparent that classical physics fails (i) whenever the dimensions of an object approach atomic length scales, and (ii) when the speed of an object approaches the speed of light. Among the most important milestones are Planck’s discovery in 1900 that the energy of black body radiation is quantized, which culminated in the introduction of light quanta (later named ‘photons’) by Einstein in 1905, and the prediction of quantized energy levels in the hydrogen atom by Bohr in 1913. The Schrödinger equation (1926) and Heisenberg’s uncertainty principle (1927) form the basis of the new quantum theory of physics.

In combination with today’s ability to fabricate and investigate nanostructured materials we have unprecedented possibilities to develop new low-dimensional systems whose intriguing properties are ruled by the laws of quantum mechanics and to reach a better understanding of physics at the nanoscale. In the present thesis we investigate the electronic structure of different two-dimensional (2D) electron systems localized at the surface of a substrate using angular resolved photoemission spectroscopy (ARPES).

One focus of this thesis lies on the influence of the spin-orbit interaction in the symmetry-broken environment at the surface of a crystal. The Rashba-Bychkov (RB) effect [1,2] states that the spin degeneracy of an asymmetrically confined 2D electron gas is lifted by the spin-orbit interaction. The resulting dispersion in the nearly free electron model consists of two parabolas shifted away from the $\bar{\Gamma}$ point by an amount $\pm k_R$. The spin-polarization of the typical RB dispersion is completely in-plane and tangential to the circular constant energy contours. The RB effect opens up new pathways for the manipulation of the electron spin by electronic means and might eventually lead to new applications in the field of spintronics. Recently, 2D surface alloys were identified as a new class of materials that exhibits a particularly large RB-type spin splitting [3–5]. A surface alloy is formed by

replacing every third atom of a silver or copper (111) surface by a heavy alloy atom such as bismuth, lead or antimony. Although there is a general agreement that a structural inversion asymmetry and the presence of heavy atoms are necessary ingredients to obtain a large spin splitting, the precise mechanism remains unclear. We have investigated the influence of the weight of the alloy atoms and their outward relaxation on the size of the spin splitting. Our results allow us to develop a more complete understanding of the origin of the observed giant spin splitting.

For future device applications it is desirable to control the size of the spin splitting as well as the position of the Fermi level independently using material parameters in order to obtain the Fermi surface with the desired spin texture. As a first step in this direction it has been shown that the spin splitting (and at the same time the Fermi energy) can be controlled via the Bi content in a mixed $\text{Bi}_x\text{Pb}_{1-x}/\text{Ag}(111)$ surface alloy [6, 7]. We have investigated the mixed $\text{Bi}_x\text{Sb}_{1-x}/\text{Ag}(111)$ surface alloy and could show that the spin splitting increases with increasing bismuth content while the position of the Fermi level remains largely unaffected. First results on the ternary $\text{Bi}_x\text{Pb}_y\text{Sb}_{1-x-y}/\text{Ag}(111)$ surface alloy show that an independent tuning of the spin splitting and the Fermi energy should be possible.

Unfortunately, the 2D electron system of a surface alloy contributes only very little to the total density of states at the Fermi level because of the presence of the metallic substrate. In order to realize the envisioned device applications the giant spin splitting of the surface alloys needs to be transferred to a semiconducting substrate. We could show that a monolayer of bismuth trimers on silicon (111) exhibits a spin splitting of the 2D band structure that is of similar magnitude to the one in the $\text{Bi}/\text{Ag}(111)$ surface alloy.

Apart from surface alloys on $\text{Ag}(111)$ and bismuth trimers on $\text{Si}(111)$ we focus on graphene — a single layer of graphite and one of the few ideally 2D crystals available today. Although it has been believed for a long time that such ideally 2D crystals could not exist, Andre Geim and Konstantin Novoselov have shown that high quality graphene flakes can be obtained by mechanical exfoliation from graphite [8] which was awarded with this year's Nobel prize in physics. Since its discovery in 2004 graphene's intriguing electronic properties have not stopped to amaze the scientific community and to raise high hopes for its application in future high speed electronic devices. Graphene owes its fame to the extremely high mobility of its charge carriers (larger than $1 \times 10^5 \text{ cm}^2/\text{Vs}$) and to the fact that the band structure in the vicinity of the Fermi level can be approximated by a linear instead of the conventional parabolic dispersion, which means that graphene's charge carriers behave like relativistic massless Dirac particles. Due to its extremely high carrier mobility and the strict two-dimensionality of its electronic structure graphene is an excellent candidate for the next generation of electronic materials. Apart from mechanical exfoliation from graphite, which is the method of choice to produce proof of principle graphene devices, graphene can be grown epitaxially on different substrates which allows for large-scale production. The substrate of choice for future commercial devices is semiconducting silicon carbide. When annealing the substrate at elevated temperatures silicon atoms leave the substrate whereas carbon atoms remain behind to form graphene layers [9]. On $\text{SiC}(0001)$ — the so-called silicon face — the strong graphene-substrate interaction leads to uniform

layer-by-layer growth [10, 11]. Unfortunately, the strong graphene-substrate interaction though beneficial for homogeneous graphene growth is detrimental for the charge carrier mobility [12].

For future device applications of epitaxial graphene on SiC(0001) three major obstacles have to be overcome. The first one is the absence of a band gap, which leads to low on-off ratios in graphene-based field effect transistors. Such a band gap will open up in graphene nanoribbons due to quantum confinement of the charge carriers. Recently, it has been shown that graphene nanoribbons can be grown on a templated SiC substrate [13]. The second obstacle is to find appropriate chemical doping methods. Epitaxial graphene on SiC(0001) is intrinsically n-doped due to charge transfer from the substrate. Therefore, we need to find easy means of p-type doping. The challenge here is to extract electrons out of the graphene layer without destroying graphene's peculiar band structure. We have shown that this can be achieved by atomic doping using bismuth, antimony or gold atoms. Finally, epitaxial graphene on SiC(0001) needs to be decoupled from the substrate in order to restore its unique electronic properties. The graphene layer on SiC(0001) rests on a carbon buffer layer. We have found that this carbon buffer layer can be decoupled from the SiC substrate by gold intercalation. The resulting quasi free-standing graphene layer is hardly influenced by the underlying substrate which we expect to result in improved electronic properties.

An introduction about the physical and technical background required for the understanding of the experimental results is given in chapter 2 and 3. In chapter 4 we will present our results about the influence of the weight of the alloy atoms and their outward relaxation on the size of the RB-type spin splitting in surface alloys. Furthermore, we will show how to tune the size of the spin splitting as well as the position of the Fermi level in mixed binary and ternary surface alloys. In chapter 5 we will show that the concept of the giant spin splitting in surface alloys can be transferred to a silicon substrate. In chapter 6 we develop a more complete understanding about the origin of the RB-type spin splitting at surfaces including our recent results. Chapter 7 is dedicated to our experimental results concerning epitaxial graphene on SiC(0001). In chapter 8 we will summarize the main results of this thesis and present some ideas for future research projects based on the previous chapters.

Chapter 2

Scientific background

2.1 The two-dimensional electron gas

When the spatial expansion of a material becomes smaller than the wavelength of the conduction electrons, electrons become confined and their energy E as well as their momentum k become quantized. This leads to special electronic properties which are dominated by quantum size effects. The simplest model that describes quantum confinement is the particle in a box of width L [14]. The potential describing the box is given by

$$V(x) = \begin{cases} 0, & \text{for } 0 < x < L \\ \infty, & \text{else} \end{cases}$$

Solving the Schrödinger equation gives the following energy eigenvalues

$$E(k) = \frac{\hbar^2 k^2}{2m}$$

where m is the mass of the particle, $k = n\pi/L$, and $n \in \mathbb{N}$. Electrons can be confined in one spatial direction in a quantum well, in two spatial directions in a quantum wire, and in all three spatial directions in a quantum dot. In the following we will focus on the two-dimensional electron gas (2DEG) where the electrons are confined along one direction but are allowed to move freely in the plane perpendicular to that direction. Such 2DEGs are of particular interest because they show the (fractional) quantum Hall effect. 2DEGs located on the surface of a substrate are of particular importance in the field of surface science because they can be investigated by surface sensitive techniques like low energy electron diffraction (LEED), scanning tunneling microscopy (STM), and angular resolved photoemission spectroscopy (ARPES).

2.1.1 Two-dimensional electron gases in semiconductors

Measuring the quantum Hall effect in a 2DEG requires highest charge carrier mobilities. This can be achieved in the 2DEGs that are formed at the semiconductor-oxide interface

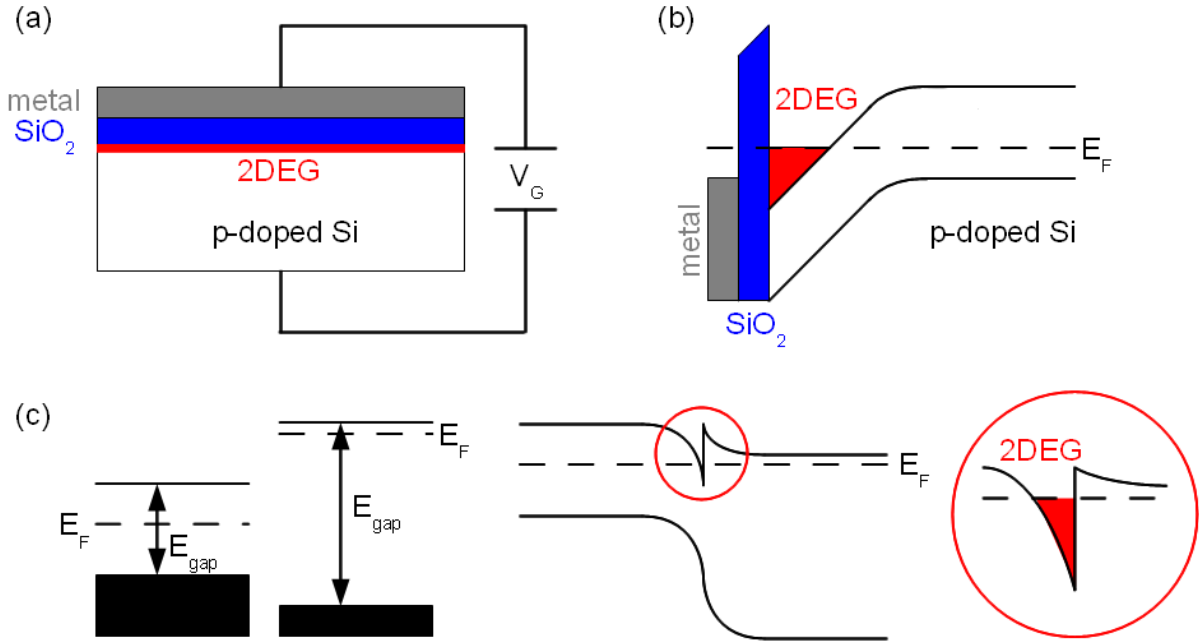


Figure 2.1: Two-dimensional electron gases: (a) **metal oxide semiconductor field effect transistor** (b) band bending due to applied gate voltage creates 2D electron gas (c) a similar band bending takes place in a semiconductor heterojunction like e.g. GaAs/ $\text{Al}_x\text{Ga}_{1-x}\text{As}$

in a metal-oxide-semiconductor field effect transistor (MOS-FET) as displayed in Fig. 2.1 (a) and (b). The applied gate voltage bends the bands at the semiconductor-oxide interface to form a triangular potential well that confines the charge carriers in the direction perpendicular to the interface. The 2D charge carrier concentration in such MOS-FETs is controlled via the applied gate voltage. A similar band bending takes place at the interface between two semiconductors with different band gaps in a semiconductor heterojunction. This is shown in Fig. 2.1 (c). In this case the charge carrier concentration is determined by the doping level. The biggest advantage of these semiconductor based 2DEGs is the extremely high charge carrier mobility in the order of $1 \times 10^6 \text{cm}^2/\text{Vs}$ [14] that makes these systems ideal candidates to investigate the (fractional) quantum Hall effect. On the other hand, these 2DEGs are localized at buried interfaces in the bulk of the crystal and cannot be investigated by surface sensitive techniques such as ARPES, STM and LEED.

2.1.2 Surface states

Solving the Schrödinger equation for an infinite periodic potential leads to the well known Bloch states of the form $\Psi_{\vec{k}}(\vec{r}) = u_{\vec{k}}(\vec{r}) \exp(i\vec{k}\vec{r})$, where $u_{\vec{k}}(\vec{r})$ is a rapidly oscillating function with the periodicity of the lattice potential [14]. In this case, periodic boundary conditions require the wave vector \vec{k} to be real. In a semi-infinite crystal, however, the component of \vec{k} normal to the crystal surface where periodic boundary conditions do not apply can

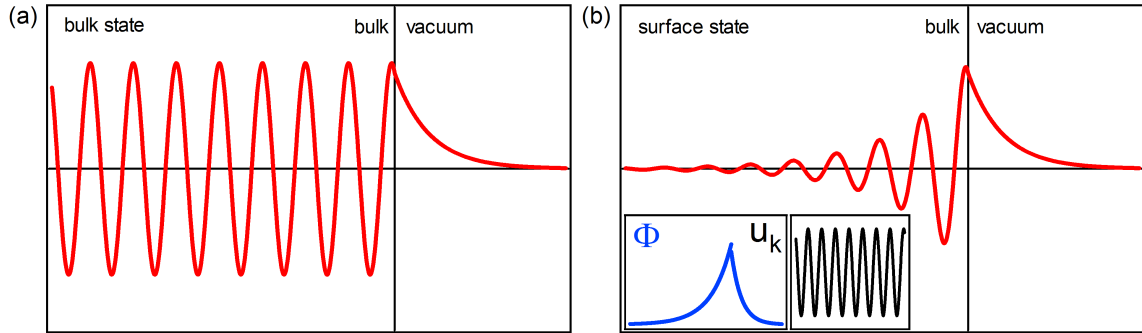


Figure 2.2: In a semi-infinite crystal the bulk states (a) are exponentially damped inside the vacuum region. Furthermore, in a semi-infinite crystal complex wave vectors are allowed. This leads to additional solutions to the Schrödinger equation, where the electron wave function is localized at the crystal surface (b) inside the projected band gap of the bulk band structure. The inset in (b) shows the envelope function (blue) and the quickly oscillating part of the Bloch wave function $u_{\vec{k}}(\vec{r})$ (black).

assume complex values leading to additional solutions of the Schrödinger equation. These additional solutions cannot exist within an infinitely expanded crystal, and their energy eigenvalues are located in the projected bulk band gap. These solutions decay exponentially towards both the vacuum and the crystal bulk (see Fig. 2.2), i.e. the corresponding electronic states are localized at the surface of the crystal. Electrons within these surface states are strongly confined in the direction perpendicular to the surface, whereas they can propagate freely in the surface plane. Therefore, surface states constitute a paradigm 2D electron system.

Such surface states were first introduced by Tamm using a 1D Kronig-Penney model [15]. Shockley extended Tamm’s model to a more general 3D potential [16]. This historical development resulted in the classification of surface states into two categories — Tamm and Shockley surface states. Shockley surface states are described in the framework of the nearly free electron model and exist simply due to the lack of translational symmetry at the surface. Tamm states, on the other hand, are usually derived from a tight binding model. The existence of Tamm surface states requires a considerable perturbation of the surface potential due to surface reconstruction or relaxation [17].

In addition to surface states there are so called ‘surface resonances’. Their decay into the crystal is slow and they may overlap energetically with bulk states.

2.1.3 Graphene

In contrast to the previously mentioned quasi 2DEGs with a small but finite extension into the third spatial direction, graphene — a single layer of carbon atoms arranged in a honeycomb lattice — constitutes an ideal 2D crystal as the electrons are localized within a single

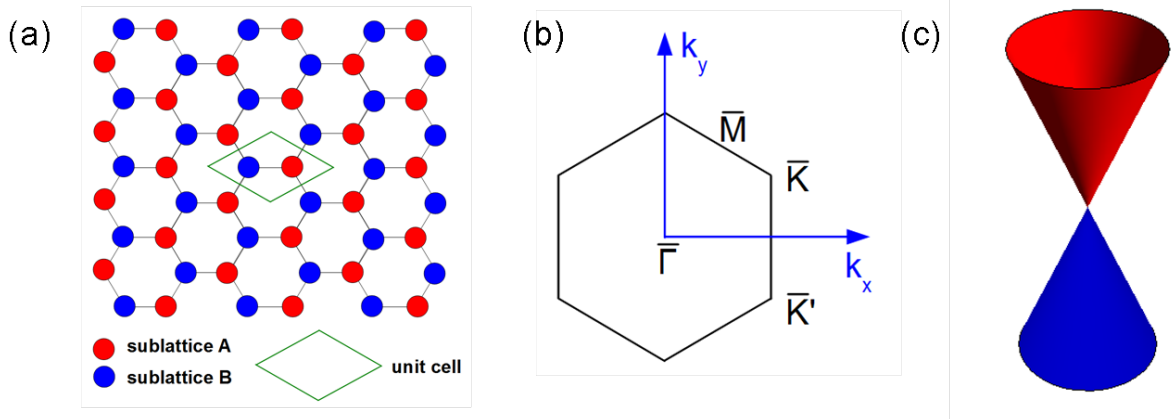


Figure 2.3: Panel (a) displays a sketch of graphene’s honeycomb lattice that consists of two equivalent sublattices shown in red and blue, respectively. The unit cell is indicated in green. The corresponding hexagonal Brillouin zone is shown in panel (b). The cosine shaped valence and conduction bands cross at the \bar{K} -point of the 2D Brillouin zone at the Fermi level, where the band structure can be approximated by a conical dispersion shown in panel (c). In the vicinity of the crossing point graphene’s charge carriers behave like massless Dirac particles.

atomic layer. Graphene was studied theoretically as soon as 1947 [18] as a model structure for 3D graphite. About forty years later Semenoff [19] realized that the band structure of the honeycomb lattice follows a linear rather than a parabolic dispersion in the low energy regime ($|E - E_F| < 1$ eV, where E_F is the Fermi energy). This implies that charge carriers in graphene behave like massless relativistic Dirac particles. Graphene therefore constitutes a condensed matter analog of (2+1)-dimensional quantum electrodynamics. For a long time, however, it was believed that such strictly 2D crystals were unstable and could not exist. Thermal fluctuations in 2D crystal lattices should lead to large displacements of atoms (comparable to interatomic distances) at any finite temperature. As a consequence the 2D crystal will simply decompose [20]. Only recently it was shown that single-layer graphene flakes can be mechanically exfoliated from bulk graphite and that these flakes are not only stable but actually possess a remarkable crystalline quality with extremely high carrier mobilities [8].

Graphene’s honeycomb lattice consists of two equivalent triangular sublattices A and B as sketched in Fig. 2.3 (a). Each sublattice is responsible for the formation of a cosine-shaped band. These bands intersect at the \bar{K} -point of the 2D Brillouin zone [see Fig. 2.3 (b)] exactly at the Fermi level. Around this crossing point the bands can be approximated by a conical dispersion [see Fig. 2.3 (c)] that is accurately described by the Dirac equation for massless particles:

$$\hbar v_F \vec{\sigma} \vec{\nabla} \Psi = E \Psi \quad (2.1)$$

where $v_F \sim 1 \times 10^6$ m/s is the Fermi velocity and $\vec{\sigma}$ are the Pauli matrices. The presence of the two equivalent triangular sublattices leads to the description of graphene’s charge carriers in terms of spinor wavefunctions Ψ , where the ‘spin’ index $\vec{\sigma}$ indicates the sublattice

rather than the real electron spin, hence the term ‘pseudospin’ [20]. This pseudospin can be visualized as the projection of the particle wavefunction onto sublattice A (pseudospin \uparrow) or B (pseudospin \downarrow). It is responsible for graphene’s many intriguing electronic properties. First of all, the crossing of the two π -bands that form the Dirac cone is only possible because they differ in one quantum number — the pseudospin. Due to the pseudospin graphene’s charge carriers accumulate a Berry phase [21] of π on closed loop paths which results in the absence of backscattering in both magnetotransport [22–25] and scanning tunneling spectroscopy experiments [26]. Furthermore, the pseudospin is responsible for the peculiar half-integer quantum Hall effect observed in graphene [27–29], and the conservation of the pseudospin upon passing a potential barrier is expected to result in perfect transparency of the barrier for graphene’s charge carriers (Klein tunneling) [30]. Meanwhile, there even exist proposals for ‘pseudospintronic’ devices, like e.g. a pseudospin valve [31].

Graphene production

Due to its extremely high carrier mobility — larger than $1 \times 10^5 \text{ cm}^2/\text{Vs}$ — and the strict two-dimensionality of its electronic structure graphene is an excellent candidate for the next generation of electronic materials. There are several methods for the production of monolayer graphene.

Mechanical exfoliation from bulk graphite results in graphene flakes with a broad thickness distribution and a lateral size of up to one millimeter [32]. After cleavage the graphene flakes are usually transferred to a SiO_2 substrate, and flakes of monolayer thickness can be identified with an optical microscope. This is a tedious procedure that will never allow to produce graphene on a large scale. However, for the fabrication of proof of principle devices mechanical exfoliation remains the method of choice.

Reduction of graphene oxide: One promising, low-cost, and easily up-scalable alternative is the reduction of graphene oxide [33, 34]. A mild ultrasonic treatment of graphite oxide (a layered material produced by the oxidation of graphite) in water results in its exfoliation to form stable aqueous dispersions that consist almost entirely of fully exfoliated graphene oxide sheets. These graphene oxide monolayers can be easily deposited onto a large variety of substrates. Although chemical reduction of close-to-insulating graphene oxide can increase its conductivity considerably it remains orders of magnitude lower than that of pristine graphene.

Epitaxial growth: The most promising approach for large scale graphene production is epitaxial growth on a substrate. Long before the recent interest in graphene it was shown that ‘monolayers of graphite’ can be grown by either **chemical vapor deposition** (CVD) on catalytic substrates or by thermal graphitization of SiC. It is known for a long time that hydrocarbons can be cracked on catalytic metal substrates like Ni [35–45], Ir [46–48], Pt [49–53], Rh [49], Ru [49] and Cu [54, 55] or on transition metal

carbides [51, 56–59] to form single layers of graphite. However, the underlying substrate affects the electronic properties of the graphene layer. For a weak graphene-substrate interaction like in the case of graphene on Ir(111) a Moiré pattern is formed. The superperiodic potential associated with the Moiré pattern gives rise to Dirac cone replicas and the opening of minigaps in the band structure [48]. For graphene on Ni(111) the graphene-substrate interaction is so strong that the linear dispersion is completely lost. This is remedied by intercalation of noble metals like Cu [39, 40, 43], Ag [41] or Au [42, 44] that saturate the Ni 3*d* bonds and weaken the interaction between graphene and substrate. Nevertheless, the metallic substrate makes these systems unsuitable for device applications. Recently, it has been shown that it is possible to transfer the graphene film to an arbitrary substrate after CVD growth on Ni(111) [45] or thin Cu films [55]. It is even possible to grow graphene directly on a dielectric substrate: single-layer graphene is formed by CVD on thin copper films predeposited on dielectric substrates that evaporate during or immediately after graphene growth, resulting in graphene deposition directly on the bare dielectric substrate [60].

A much easier alternative, however, is the growth of graphene on a semiconducting substrate like **SiC**. On both the silicon- and the carbon-terminated face of a SiC substrate, graphene is commonly grown by **thermal graphitization** in ultra high vacuum (UHV). When annealing the substrate at elevated temperatures Si atoms leave the surface whereas the C atoms remain and form carbon layers [9]. On SiC(000 $\bar{1}$), the so-called **C-face**, the weak graphene-to-substrate interaction results in the growth of rotationally disordered multilayer graphene and a precise thickness control becomes difficult [11, 61, 62]. On the other hand, the rotational disorder decouples the graphene layers so that the transport properties resemble those of isolated graphene sheets with room temperature mobilities in excess of 200,000 cm²/Vs [29, 63, 64].

On the **Si-face** the comparatively strong graphene-to-substrate interaction results in uniform, long-range ordered layer-by-layer growth [10, 11, 62, 65]. However, commercially available SiC wafers show a high density of scratches caused by mechanical polishing. This problem can be solved by hydrogen etching, where several hundred nanometers of material are removed from the surface. The resulting (0001) surface exhibits large uniform terraces with a width of 1500 Å and a height of one unit cell [66–69]. After hydrogen etching the samples are inserted into UHV where residual oxygen impurities are removed by depositing Si at a substrate temperature of 800°C until a sharp (3×3) LEED pattern is observed. Subsequent direct current heating at 1100°C for five minutes is sufficient for the formation of the first carbon monolayer. Within this so-called zero layer (ZL) every third C-atom forms a chemical bond to a Si-atom in the layer below. The partial sp³-hybridization of the ZL prevents the formation of π -bands and therefore the ZL has no graphene properties. Its band structure consists of two non-dispersing bands at about –0.3 eV and –1.2 eV initial state energy [11]. In addition, the ZL forms a (6 $\sqrt{3}$ ×6 $\sqrt{3}$)R30° reconstruction with respect to the SiC substrate [11, 61, 70–73]. Upon further annealing at 1150°C for five minutes a purely sp²-hybridized carbon layer forms on top of the ZL which shows the linear band structure characteristic of massless charge carriers in graphene. The band structure of this “conventionally” grown graphene monolayer (cML) near the \bar{K} -point

is influenced considerably by the underlying SiC substrate. It is n-doped with the crossing point of the two linear bands (Dirac point) at $E_D = -420$ meV due to charge transfer from the substrate [74–77]. Furthermore, the possibility of a band gap opening has been discussed [71, 76, 78–80]. And, worst of all, the strong substrate influence is detrimental for the charge carrier mobility [12].

However, UHV graphitization of SiC is accompanied by a considerable roughening of the surface and yields graphene layers consisting of small grains (30–200 nm). As nucleation of new graphene layers starts at step edges, monolayer graphene areas coexist with graphene bilayer islands as well as with uncovered regions of the buffer layer. Recently, it was shown that graphene films grown under 900 mbar of argon atmosphere have a greatly improved surface morphology. Instead of a surface roughening step bunching occurs, resulting in macro-terraces that are a factor of 5–8 times wider than the original terraces and that are homogeneously covered with a graphene monolayer [81].

2.2 The Rashba effect and its applications

2.2.1 Spin-orbit interaction

Electrons move with a velocity \vec{v} in the electric field created by the nucleus $\vec{E} = \frac{1}{e} \frac{\vec{r}}{r} \frac{\partial V}{\partial r}$. In the rest frame of the electron this electric field transforms into a magnetic field $\vec{B} = -(\vec{v} \times \vec{E})/c^2$, where c is the speed of light, that interacts with the magnetic moment $\vec{\mu}$ of the electron. The energy of the electron in this field is given by $\Delta E = -\vec{\mu} \cdot \vec{B}$ with $\vec{\mu} = -g_e \mu_B \vec{s}/\hbar$, where $g_e = 2.002$ is the g -factor of the electron, $\mu_B = e\hbar/(2m_e)$ is the Bohr magneton, m_e is the electron mass, and \vec{s} is the electron spin. Using $\vec{l} = \vec{r} \times \vec{p}$, where \vec{l} is the orbital angular momentum of the electron, one finds — after backtransformation into the rest frame of the nucleus — the spin-orbit interaction (SOI) term [82]

$$\Delta E = \frac{\mu_B}{\hbar m_e c^2} \frac{1}{r} \frac{dV}{dr} (\vec{l} \cdot \vec{s}) \quad (2.2)$$

The SOI is a consequence of the relativistic behavior of the electron and can be derived from the Dirac equation [83]

$$(c\vec{\alpha}\vec{p} + \beta m_e c^2 + V)\Psi = E\Psi \quad (2.3)$$

where

$$\alpha = \begin{pmatrix} 0 & \vec{\sigma} \\ \vec{\sigma} & 0 \end{pmatrix}$$

and

$$\beta = \begin{pmatrix} \mathbb{1} & 0 \\ 0 & -\mathbb{1} \end{pmatrix}$$

with the Pauli spin matrices $\vec{\sigma} = (\sigma_x, \sigma_y, \sigma_z)$ and the (2×2) unitary matrix $\mathbb{1}$. $\Psi = (\Psi_A, \Psi_B)$ is a four component spinor. This allows us to rewrite Eq. (2.3) as follows

$$\begin{aligned} \vec{\sigma}\vec{p}\Psi_B &= \frac{1}{c}(E - m_e c^2 - V)\Psi_A \\ \vec{\sigma}\vec{p}\Psi_A &= \frac{1}{c}(E + m_e c^2 - V)\Psi_B \end{aligned}$$

We can eliminate $\Psi_B = \frac{c}{E + m_e c^2 - V} \vec{\sigma}\vec{p}\Psi_A$ and obtain

$$\vec{\sigma}\vec{p} \left(\frac{c^2}{E + m_e c^2 - V} \right) \vec{\sigma}\vec{p}\Psi_A = (E + m_e c^2 - V)\Psi_A$$

By expanding the energy denominator in the non-relativistic limit

$$\frac{c^2}{E + m_e c^2 - V} \approx \frac{1}{2m_e} \left(1 - \frac{E + m_e c^2 - V}{2m_e c^2} + \dots \right)$$

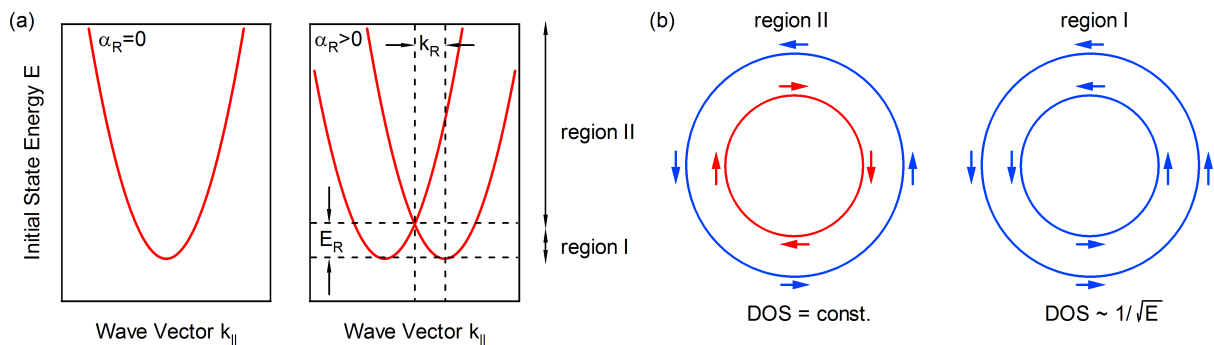


Figure 2.4: (a) dispersion of the 2D free electron gas without (left) and with (right) Rashba SOI. The characteristic parameters of the RB model E_R and k_R are indicated by black arrows. (b) constant energy contours of region II (left) and region I (right) with the corresponding spin-polarization for $\alpha_R > 0$.

we obtain the Pauli equation for a spherically symmetric potential

$$\left(\frac{p^2}{2m_e} + V - \frac{\hbar^2}{4m_e^2 c^2} \frac{dV}{dr} \frac{\partial}{\partial \vec{r}} + \frac{1}{2m_e^2 c^2} \frac{1}{r} \frac{dV}{dr} \vec{l} \vec{s} \right) \Psi_A = E \Psi_A \quad (2.4)$$

where the third term on the left hand side is the Darwin term (which gives rise to the Zitterbewegung of the electron), and the fourth term is the Pauli SOI from Eq. (2.2). In a solid the dominant contribution to the Pauli SOI comes from the electron motion in the bare Coulomb potential of the innermost region of the atomic cores. The potential gradient dV/dr is proportional to the atomic number Z . Therefore, the SOI becomes important in heavy elements with a large Z .

2.2.2 The Rashba-Bychkov model

Spin degeneracy is the consequence of combined time reversal [$E(\uparrow, \vec{k}) = E(\downarrow, -\vec{k})$] and spatial inversion symmetry [$E(\uparrow, \vec{k}) = E(\uparrow, -\vec{k})$] that leads to $E(\uparrow, \vec{k}) = E(\downarrow, \vec{k})$. If the spatial inversion symmetry is broken the spin degeneracy can be lifted by the SOI. The loss of space inversion symmetry can either originate from a bulk inversion asymmetry in non centrosymmetric semiconductors (Dresselhaus effect [84]) or from a structural inversion asymmetry (Rashba-Bychkov (RB) effect [1, 2]). A structural inversion asymmetry is caused e.g. by the asymmetric confinement potential of the 2D electron gas in a semiconductor heterostructure, or simply by the presence of the surface in a semi-infinite crystal. As a consequence, the electronic states that feel this structural inversion asymmetry (2D electron gas in a semiconductor heterostructure or 2D surface states) become spin-polarized. The RB-Hamiltonian for the SOI in a quasi-free 2D electron gas confined in the (x, y) -plane with an inversion asymmetry along the z -direction reads [1, 2]

$$H_{RB} = \alpha_R \vec{\sigma}(\vec{k}_{\parallel} \times \vec{e}_z) \quad (2.5)$$

where α_R is the Rashba constant, $\vec{\sigma} = (\sigma_x, \sigma_y, \sigma_z)$ are the Pauli matrices, \vec{k}_{\parallel} is the in-plane momentum, and \vec{e}_z is a unit vector perpendicular to the plane of the 2D electron gas. Solving the Schrödinger equation leads to the following energy dispersion

$$E(k_{\parallel}) = E_0 + \frac{\hbar^2 k_{\parallel}^2}{2m^*} \pm \alpha_R k_{\parallel} = E_0 + \frac{\hbar^2}{2m^*} (k_{\parallel} \pm k_R)^2 \quad (2.6)$$

Equation (2.6) describes two parabolas with effective mass m^* with an offset $\pm k_R = \alpha_R m^* / \hbar^2$ away from $k_{\parallel} = 0$. The momentum offset k_R translates into a characteristic energy called the Rashba energy $E_R = \hbar^2 k_R^2 / (2m^*) = m^* \alpha_R^2 / (2\hbar^2)$. Time reversal symmetry requires that the two spin-polarized parabolas cross at time-reversal invariant momenta of the 2D Brillouin zone. The dispersion of a 2D free electron gas with and without Rashba SOI is sketched in Fig. 2.4 (a). Constant energy contours of the 2D RB dispersion consist of two concentric circles. The RB dispersion can be divided into two different regions: region I is the energy interval between the band minimum at $E = E_0$ and the crossing point of the two parabolas at $E = E_R$, region II includes the energies $E > E_R$. These two regions differ with respect to the 2D density of states (DOS; constant in region II, $1/\sqrt{E}$ -behavior in region I [4, 83]) and the spin-polarization [see Fig. 2.4 (b)]. From the cross product in Eq. (2.5) we see that the electron spin aligns perpendicular to both \vec{k}_{\parallel} and \vec{e}_z , i.e. the spin-polarization is completely in-plane and parallel to the circular constant energy contours. For $\alpha_R > 0$ the electron spin rotates counterclockwise on the outer contour and clockwise on the inner contour in region II. In region I the spins rotate counterclockwise on both constant energy contours. Integration over momentum space yields zero net spin, i.e. the system is not magnetic.

The spin-polarization of the 2D states caused by the RB effect can be compared to the spin-polarization caused by the Zeeman effect if one considers $\alpha_R (\vec{k}_{\parallel} \times \vec{e}_z)$ as an effective \vec{k} -dependent magnetic field B_{eff} that aligns the electron spin. The direction of B_{eff} , i.e. the spin quantization axis, is then essentially determined by the cross product between \vec{k}_{\parallel} and the structural inversion asymmetry along \vec{e}_z , whereas the size of the spin splitting is determined by the Rashba constant α_R . Within the framework of the quasi-free electron model the Rashba constant α_R is determined by the structural inversion asymmetry which is parametrized as an electric field \vec{E} along \vec{e}_z , i.e. $\vec{E} = (0, 0, E_z)$. In the rest frame of the electron moving with a velocity v_{\parallel} this electric field transforms into a magnetic field $B = (v_{\parallel}/c^2)E_z$. For typical values of E_z and v_{\parallel} this would result in a spin splitting that is several orders of magnitude smaller than observed experimentally [83, 85]. This is not surprising: from Eq. (2.2) we know that the main contribution to the SOI actually comes from the Coulomb field of the atomic core that is neglected in this simplified model. This can be visualized as follows. Electrons in the periodic potential of a solid are described by Bloch wave functions of the form $\Psi_{\vec{k}}(\vec{r}) = u_{\vec{k}}(\vec{r}) \exp(i\vec{k}\vec{r})$, where $u_{\vec{k}}(\vec{r})$ is a quickly oscillating function with the periodicity of the lattice potential. In the Envelope Function Approximation [83] the full wave function of the electron is a product of $u_{\vec{k}}(\vec{r})$ times a slowly varying envelope function $\Phi_{\vec{k}}(\vec{r})$ [see inset of Fig. 2.2 (b)]. The Bloch part $u_{\vec{k}}(\vec{r})$ of the wave function feels the strong atomic fields, whereas the envelope function $\Phi_{\vec{k}}(\vec{r})$ is

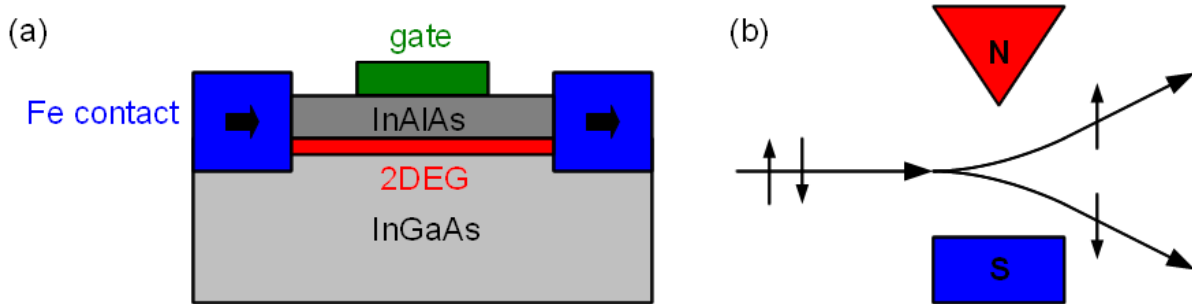


Figure 2.5: (a) sketch of the spin field effect transistor as proposed by Datta and Das [86]. The RB-type SOI induces a phase shift $\Delta\phi = 2m^*\alpha_R L/\hbar^2$ between electrons with spin \uparrow and spin \downarrow , respectively, where α_R is controlled by the gate voltage. (b) In the Stern-Gerlach experiment a spatially varying magnetic field plays the role of a spin-dependent potential that accelerates particles with opposite spin in opposite directions. Such a spatially varying magnetic field can be created in a 2DEG with RB-type SOI, where the strength of the SOI is varied in the direction perpendicular to the charge current by a gate voltage.

sensitive to the structural inversion asymmetry [83]. Using a simple tight binding model Petersen and Hedegård [85] could show that the Rashba constant α_R is proportional to the atomic spin-orbit coupling parameter and an asymmetry parameter γ . This asymmetry parameter describes the mixing of p_z - and p_{xy} -orbitals, thereby including the effect of an external electric field. If inversion symmetry is restored, $\gamma = \alpha_R = 0$. In order to obtain a sizable spin splitting one needs a structural inversion asymmetry combined with strong atomic fields.

2.2.3 Applications of the RB effect

The possibility to tune the spin splitting by an external gate voltage forms the basis for many spintronic device proposals such as the Datta-Das spin field effect transistor [86]. Furthermore, a gradient in the effective magnetic field caused by a spatial variation of the RB-type SOI leads to spin separation in the Stern-Gerlach spin filter [87]. In addition, 2D spin-split states are expected to show the intrinsic spin Hall effect [88, 89], and an enhancement of the superconducting temperature is predicted in the regime where the Rashba splitting is larger than the Fermi energy [90].

Datta-Das spin field effect transistor: In the spin FET proposed by Datta and Das [86] see Fig. 2.5 (a)] the RB-type SOI in the 2DEG at the interface between two semiconductors is controlled by a gate voltage. Spin-polarized electrons are injected and detected with ferromagnetic contacts. The initial polarization of the electrons along the

x -direction $\begin{pmatrix} 1 \\ 1 \end{pmatrix}$ can be decomposed into

$$\begin{pmatrix} 1 \\ 1 \end{pmatrix} = \begin{pmatrix} 1 \\ 0 \end{pmatrix} + \begin{pmatrix} 0 \\ 1 \end{pmatrix}.$$

These two components precess during the propagation of the electrons in the RB field so that the electrons arriving at the second contact have the following polarization

$$\begin{pmatrix} 1 \\ 0 \end{pmatrix} + e^{i\Delta\phi} \begin{pmatrix} 0 \\ 1 \end{pmatrix}$$

where the phase shift $\Delta\phi = 2k_R L$ depends on the momentum offset k_R (i.e. on the gate voltage) and on the length of the 2D channel L . For $\Delta\phi = 2n\pi$ with $n \in \mathbb{N}$, the electron spin matches the spin-polarization in the drain contact and the 2D channel is open. For $\Delta\phi = 2(n+1)\pi$ the electron spin and the spin-polarization in the drain contact are antiparallel to each other and the 2D channel is closed.

Stern-Gerlach spin filter: In the original Stern-Gerlach experiment [see Fig. 2.5 (b)] the derivative of the magnetic field acts as a spin-dependent potential that accelerates charge neutral particles with opposite spin in opposite directions. Such a spatially varying magnetic field is implemented in a 2DEG with RB-type SOI, where the effective magnetic field felt by the propagating electrons is varied in the direction perpendicular to the current by a gate voltage [87]. Nearly 100% spin-filtering can be achieved.

The spin Hall effect causes spin accumulation in the direction perpendicular to the charge current in a 2DEG. The origin of the spin Hall effect is the SOI that couples the spin to the orbital motion of the carriers. The spin accumulation can be caused either by a Rashba or Dresselhaus splitting of the 2D band structure (intrinsic spin Hall effect) or by a spin-dependent impurity scattering (extrinsic spin Hall effect). The intrinsic spin Hall effect can only be observed if the spin splitting of the initial states is larger than their lifetime broadening [88]. However, it remains unclear at present whether the predicted dissipationless spin currents are actual transport currents that lead to an experimentally observable spin accumulation [91]. Furthermore, the SOI in a symmetry broken environment also plays a key role for the observation of the quantum spin Hall effect where dissipationless spin currents flow at the edges of a 2D topological insulator at zero magnetic field [92].

Superconductivity: In region I where the Fermi level lies between the band minimum at E_0 and the crossing point of the two spin-polarized bands at E_R the density of states shows quasi one dimensional behavior and the Fermi surface exhibits a peculiar spin texture, where the spins have the same sense of rotation on both Fermi contours (see Fig. 2.4). The strong 1D-like divergence of the density of states directly influences the binding energy for a Cooper pair Δ in the system. For a 2D Rashba system in region I one finds $\Delta \propto E_R$,

i.e. the relevant energy scale for the onset of superconductivity is now given by the Rashba energy E_R so that a significant increase of the superconducting critical temperature is expected in systems with a large Rashba splitting [90].

2.2.4 Rashba effect on surfaces

Clean surfaces

The RB model was developed to explain the observed spin splitting in asymmetrically confined 2D electron gases in semiconductor heterostructures where experimentally observed splittings are typically on the order of 0.1 to 10 meV [83]. However, these are not the only systems that exhibit a RB-type spin splitting. 2D surface states owe their mere existence to the presence of a structural inversion asymmetry — the crystal surface. Such surface states are confined within the first few atomic layers and are therefore very sensitive to the asymmetric potential at the surface. LaShell *et al.* [93] were the first to discover the RB-type spin splitting of the sp_z -derived surface state in the projected bulk band gap at $\bar{\Gamma}$ on Au(111). They reported a spin splitting of 110 meV at the Fermi level which is at least one order of magnitude larger than for typical semiconductor heterostructures. The related surface states on Cu(111) and Ag(111) do not show a spin splitting which was attributed to their comparatively small atomic numbers [94]. A similar, though substantially larger spin splitting than in the surface state on Au(111) exists on Bi(111), Bi(110), and Bi(100) [95], on Sb(111) [96] and in the d -derived surface states of W(110) [97] and Lu(0001) [98].

Manipulating the spin splitting

Different approaches have been chosen to manipulate the spin splitting of these metal surface states. The spin splitting on W(110) and Mo(110) can be increased by a factor of two to three by Lithium adsorption [97], the spin splitting on Au(111) increases by up to 30% by rare gas adsorption (Ar, Kr, Xe) [99, 100], and oxidizing the surface of Gd(0001) to form $p(1 \times 1)\text{O}/\text{Gd}(0001)$ increases the spin splitting by a factor of three [101]. Furthermore, deposition of thin Ag films on Au(111) decreases the spin splitting of the surface state, and in a chemically disordered $\text{Au}_x\text{Ag}_{1-x}$ alloy the spin splitting of the surface state can be decreased continuously by reducing the Au concentration x in the uppermost atomic layers [102–104].

Giant spin splitting through surface alloying

The biggest increase of the spin splitting so far was achieved by surface alloying [5], where every third atom of a noble metal Ag(111) [3–5, 7, 105–107] or Cu(111) surface [106, 108] is replaced by a heavy alloy atom (Bi, Pb, Sb). The resulting $(\sqrt{3} \times \sqrt{3})\text{R}30^\circ$ structure is displayed in Fig. 2.6. In contrast to the clean (111) substrate the surface of the surface alloy is corrugated due to the outward relaxation Δz of the alloy atoms. The surface alloys Bi/Ag(111) and Pb/Ag(111) show an unprecedented spin splitting of $E_R = 200$ meV [5] and $E_R = 23$ meV [4], respectively. This is huge compared to the Rashba energy

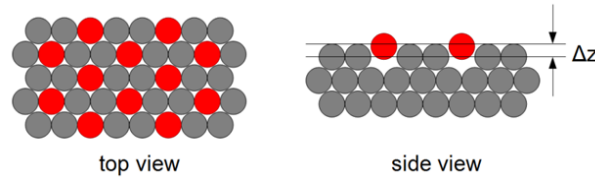


Figure 2.6: Top view (left) and side view (right) of the $(\sqrt{3} \times \sqrt{3})R30^\circ$ structure formed by surface alloys on Ag(111) and Cu(111). Every third atom in the (111) surface is replaced by an alloy atom (red). The alloy atoms relax outward by an amount Δz .

$E_R = 2.1$ meV for the Au(111) surface state. The reason for the considerable enhancement of the spin splitting in surface alloys has to be sought in the structure of the $(\sqrt{3} \times \sqrt{3})R30^\circ$ reconstructed surface. The considerable outward relaxation of the alloy atoms determines the asymmetry parameter γ (i.e. the orbital character of the surface state wave function) which for its part determines the size of the spin splitting [85, 109]. Furthermore, the corrugation of the surface potential leads to an out-of-plane spin component [5, 110]. In the free electron RB model this can be understood as originating from an in-plane component of ∇V resulting from an in-plane inversion asymmetry [111]. It has been shown that the characteristic parameters of the RB-type dispersion can be tuned continuously in a mixed $\text{Bi}_x\text{Pb}_{1-x}/\text{Ag}(111)$ surface alloy [6].

Spin-polarized surface states on semiconducting substrates

Usually, surface states contribute only very little to the density of states at the Fermi level, so that the observed RB splitting of these states will not influence the transport properties of these systems. Therefore, it is desirable to transfer the concept of the giant spin splitting to a semiconducting substrate. One step in this direction is the growth of ultrathin Bi films [112–116] on Si(111). There, however, spin-polarized surface states and spin degenerate quantum well states coexist at the Fermi level. Recently, it was shown with spin- and angular resolved photoemission spectroscopy that the quantum well states in ultrathin Pb films on Si(111) show a small spin splitting on the order of 10 meV [117]. Another attempt was to grow Pb/Ag(111) and Bi/Ag(111) surface alloys on ultrathin Ag films on Si(111) [118–120]. But similar to the ultrathin Bi films on Si(111) spin-polarized surface states and spin degenerate quantum well states of the Ag film coexist at the Fermi level. A more promising direction is to induce a spin-polarization of the surface state on a semiconducting substrate. One monolayer Tl on Si(111) shows a spin split surface state with a Rashba energy of $E_R = 20$ meV at the $\bar{\Gamma}$ -point [121]. This splitting, however, is small compared to the giant spin splitting in the Bi/Ag(111) surface alloy, and the surface state does not cross the Fermi level. Another promising material system are (sub-)monolayer phases of Bi on Si(111) [122]. Previous ARPES results for the trimer phase at one monolayer Bi coverage revealed the presence of at least four surface states, two of which cross at high symmetry points [123]. The origin of these surface state bands was attributed to bonding between Bi and Si and bonding of Bi atoms in a trimer, respectively

[124]. Whether these surface states are actually spin-polarized remains an open question.

Origin of the RB-type spin splitting

Although there is a general agreement about some necessary ingredients for a large RB-type spin splitting — such as a structural inversion asymmetry and the presence of heavy atoms — many open questions remain, especially concerning the influence of the different parameters in different material systems. For Li/W(110) [97] the increase of the RB splitting with Li coverage was attributed to a variation in the surface potential gradient although it is obvious that the surface potential gradient alone cannot account for the size of the spin splitting [83, 85]. The increase of the spin splitting due to rare gas adsorption on Au(111) was attributed to the Pauli repulsion between the filled orbitals of the rare gas atoms and the orbitals of the substrate that shifts the electron density of the surface state to regions where the potential gradient is larger. The change of the work function (i.e. of the potential gradient itself) seemed to play a minor role in this case [99, 100]. In contrast to Au(111), Xe adsorption onto the Bi/Ag(111) surface alloy had no measurable influence on the size of the spin splitting [105] indicating that different mechanisms influencing the spin splitting might be at work. For Ag/Au(111) the authors argued that the spin splitting is solely determined by the number of heavy Au atoms probed by the Shockley state wave function [102–104]. An estimate for the atomic contribution to the size of the spin splitting can be obtained from the spin-orbit coupling in the corresponding single atoms [95, 125]. In the Bi/Ag(111) surface alloy, however, the size of the spin splitting cannot be explained by the presence of heavy Bi atoms alone because the splitting is larger than the splitting of the surface states on clean Bi(111) where the number of Bi atoms in the surface layer is three times higher than in the Bi/Ag(111) surface alloy [5]. For Au and Ag, respectively, on W(110) the size of the spin splitting was found to be entirely independent of the atomic number of the overlayer [126]. Recently, it was argued that the spin splitting is determined by the asymmetry of the wave function — characterized by different l -components of the surface state — near the nucleus [98]. The giant spin splitting in surface alloys was attributed to the outward relaxation of the alloy atoms that directly influences the orbital composition of the surface state wave function [109] and to an additional in-plane inversion asymmetry [5, 111]. Furthermore, there are contradicting opinions about the influence of the substrate on the size of the spin splitting in surface alloys [106, 108].

Regarding this variety of possible explanations a unified theory explaining the origin and the size of the RB-type spin splitting in different material systems is clearly desirable — if it exists. Such a theory would enable a systematic control of the spin splitting via material parameters and, therefore, would allow us to produce a material with the desired spin texture at the Fermi surface.

Chapter 3

Technical background

3.1 Photoemission spectroscopy

3.1.1 The photoelectric effect

Photoemission spectroscopy (PES) is based on the photoelectric effect discovered by Hertz in 1887 [127]. In 1905, Einstein was able to explain this effect by invoking the quantum nature of light [128] which was rewarded with the Nobel prize in 1921. Irradiation of a material with photons of energy $\hbar\omega$ releases electrons with kinetic energy E_{kin} from the surface if the energy of the light is larger than a characteristic value E_{min} — called the work function Φ — which depends on the material. From the kinetic energy of the electron its binding energy E_B within the material can be determined via

$$E_B = \hbar\omega - \Phi - E_{kin} \quad (3.1)$$

Usually the work function Φ_S of the spectrometer is larger than the work function Φ of the sample under investigation, so that it is actually the spectrometer work function Φ_s that enters Eq. (3.1). Photoemission spectra are usually referenced with respect to the Fermi level in the sense that the Fermi level corresponds to zero binding energy. The range of accessible binding energies depends on the photon energy used for the excitation of the photoelectron. Photons in the vacuum ultraviolet (VUV) range are used for the excitation of valence electrons (ultraviolet photoemission spectroscopy UPS), whereas soft x-rays can also excite core levels (x-ray photoemission spectroscopy XPS).

3.1.2 The electron escape depth

The escape depth of electrons is determined mainly by electron-electron interactions. Electron-phonon interactions only contribute at very low energies and are neglected here. The scattering cross section for electron-electron interactions is given by [129]

$$\frac{d^2\sigma}{d\Omega dE} = \frac{\hbar^2}{(\pi\epsilon_0 a_0)^2} \frac{1}{q^2} \text{Im} \left(-\frac{1}{\epsilon(\vec{q}\omega)} \right) \quad (3.2)$$

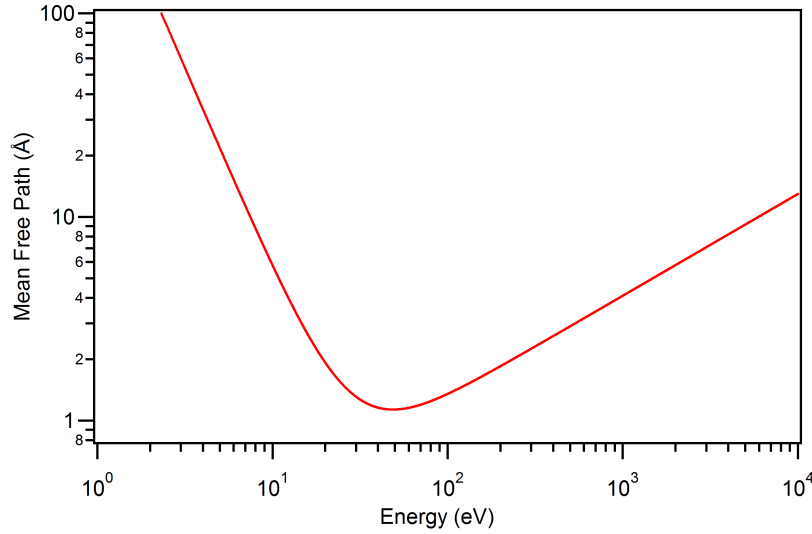


Figure 3.1: Electron mean free path as a function of energy as calculated using Eq. (3.4) from Ref. [130]

with the momentum transfer \vec{q} , the energy transfer E , and the solid angle $d\Omega$. $\epsilon_0 = 8.854 \text{ As}/(\text{Vm})$ is the vacuum permittivity and $a_0 = 0.529 \text{ \AA}$ is Bohr's radius. From the scattering cross section the electron mean free path λ can be calculated via

$$\lambda^{-1} = \int \int \frac{d^2\sigma}{d\Omega dE} d\Omega dE \quad (3.3)$$

Therefore, the average escape depth is essentially determined by the dielectric function $\epsilon(\vec{q}\omega)$. For the relevant energy range of PES the electrons can be approximately described by a free electron gas. In this case the dielectric function $\epsilon(\vec{q}\omega)$ is determined by the plasma frequency which depends only on the electron concentration. As the mean electron-electron distance is roughly equal for all materials, the mean free path λ follows the universal curve depicted in Fig. 3.1. This curve was calculated using the phenomenological function from Ref. [130]

$$\lambda(E) = \frac{538}{E^2} + 0.41\sqrt{aE} \quad (3.4)$$

where a is the thickness of a monolayer in nm. For the range of kinetic energies relevant for PES the electron escape depth is of the order of a few \AA only. This makes PES a very surface sensitive technique.

3.1.3 The photoemission process

In the simplest description of the photoemission process [Eq. (3.1)], a photon impinges on a sample surface and an electron, which is excited via the photoelectric effect, escapes into the vacuum. During this interaction energy and momentum conservation have to be

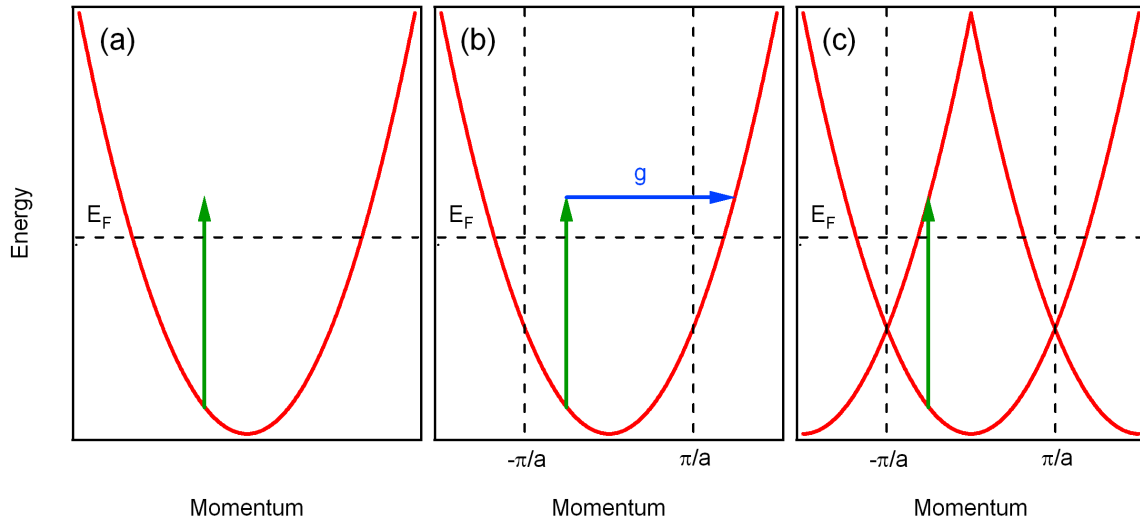


Figure 3.2: For a free electron gas direct transitions are not possible (a). The influence of a periodic crystal potential enables direct transitions. Extended zone scheme (b) and periodic zone scheme (c).

fulfilled. As the photon momentum is small compared to the electron momentum \vec{k} it can be neglected. The resulting direct transitions are forbidden in the free electron model because energy and momentum conservation cannot be fulfilled at the same time due to the lack of appropriate final states. Direct transitions, however, become possible in a crystal lattice, where a lattice vector \vec{g} can compensate for the missing momentum. This is illustrated in Fig. 3.2.

For the interpretation of photoemission experiments the simple picture as described by Eq. (3.1) is hardly sufficient. In the following sections we will look at the photoemission process in more detail and derive a more appropriate description in terms of the three-step and the more realistic one-step model.

The three-step model

The three-step model [129] is the most intuitive approach to the photoemission process. Within the framework of this model the photoemission process is artificially split into three independent parts. The first step is the photoexcitation of the electron, where a photon is absorbed and an electron-hole pair is created inside the crystal. The probability w for this photoexcitation is given by Fermi's Golden Rule. In a second step, the electron propagates towards the crystal-vacuum interface. During this step the photoelectrons scatter with other electrons, plasmons or phonons, lose part of their energy and change their momentum. In the third step the electron is refracted at the crystal-vacuum interface and escapes through the surface. The measured photocurrent I is then proportional to the product of (i) the probability for the photoexcitation, (ii) the probability for the electron to arrive at the crystal-vacuum interface without being scattered, and (iii) the transmission

function for the crystal-vacuum interface.

The one-step model

The separation of the photoemission process into three steps is artificial. The correct treatment of the photoemission process considers the whole process as one single step. The one-step model [129] discusses the excitation from an initial state (Bloch state) into a damped final state near the surface. This damping takes care of the short mean free path of the electrons in a solid. In contrast to the three-step model, where the three processes are considered as being independent from each other, the one-step model takes into account interference between the three artificial steps. A correct one-step treatment of the photoemission process is based on Fermi's Golden Rule with proper functions for the initial and final state and the dipole operator for the interaction between electron and photon. This problem, however, cannot be solved rigorously. Various approximations have to be used to make a one-step calculation feasible. One of these approximations is the so-called sudden approximation [129] which will be presented in the next paragraph.

The sudden approximation The photocurrent in a photoemission experiment results from the excitation of an electron from the initial state Ψ_i to the final state Ψ_f caused by a photon field with vector potential \vec{A} . The photocurrent I is proportional to the transition probability w and can be calculated with Fermi's Golden Rule using the dipole approximation [129]:

$$I \propto \frac{2\pi}{\hbar} |\langle \Psi_f | \vec{A} \vec{p} | \Psi_i \rangle|^2 \delta(E_f - E_i - \hbar\omega) \quad (3.5)$$

In the simplest approximation the wave function for the initial (final) state can be written as a product of the orbital $\Phi_{i,\vec{k}}$ from which the photoelectron is emitted (the wave function $\Phi_{f,E_{kin}}$ of the photoemitted electron) times the wave function of the remaining $N - 1$ electrons. For solids the photocurrent I is usually written in terms of the spectral function $A(\vec{k}, E)$ [129]:

$$I \propto \sum_{f,i,\vec{k}} |\langle \Phi_{f,E_{kin}} | \vec{r} | \Phi_{i,\vec{k}} \rangle|^2 A(\vec{k}, E) \quad (3.6)$$

As can be seen from Eq.(3.6) PES essentially measures the spectral function $A(\vec{k}, E)$. This spectral function is related to the single particle Green's function $G(\vec{k}, E)$ via

$$A(\vec{k}, E) = \frac{1}{\pi} \text{Im} \left(G(\vec{k}, E) \right).$$

For a gas of free electrons $G_0(\vec{k}, E) = 1/(E - E_{\vec{k}}^0 - i\epsilon)$, where ϵ is a small number. In this case the spectral function is a δ -function $A_0(\vec{k}, E) = \delta(E - E_{\vec{k}}^0)$ and the dispersion is given by $E_{\vec{k}}^0 = \hbar^2 k^2 / (2m^*)$. When interactions are taken into account the electron energy is renormalized by the so-called self energy $\Sigma(\vec{k}, E)$ which leads to the following Green's

function

$$G(\vec{k}, E) = \frac{1}{E - E_{\vec{k}}^0 - \Sigma(\vec{k}, E)}$$

and the corresponding spectral function

$$A(\vec{k}, E) = \frac{1}{\pi} \frac{Im(\Sigma(\vec{k}, E))}{\left[E - E_{\vec{k}}^0 - Re(\Sigma(\vec{k}, E)) \right]^2 + \left[Im(\Sigma(\vec{k}, E)) \right]^2} \quad (3.7)$$

In the simplest case $Im(\Sigma)$ is constant, $Re(\Sigma) = 0$, and $A(\vec{k}, E)$ is a Lorentzian with full width at half maximum $\Gamma = 2Im(\Sigma)$ positioned at $E_{\vec{k}}^0$. As can be seen from Eq. (3.7) $Re(\Sigma)$ causes deviations from the bare band dispersion $E_{\vec{k}}^0$, and $Im(\Sigma)$ is responsible for the intrinsic line width of the photoemission spectrum. $E_{\vec{k}}^0$ is solely determined by the symmetries of the lattice potential. The ability to measure the renormalized dispersion together with an accurate determination of the photoemission line width makes PES a powerful tool for the investigation of many-body interactions in solids.

3.1.4 Quasiparticle picture

The full Hamiltonian describing electrons in the periodic potential of a solid contains not only the one-electron potentials describing the interaction between electrons and the ionic cores but also many-body interactions. In the independent electron approximation the problem is reduced to a single electron moving in the effective potential $U_{eff}(\vec{r})$ of the atomic cores and the remaining $(N - 1)$ electrons with the resulting bare band dispersion $E_{\vec{k}}^0$. When many-body interactions are taken into account the independent electron picture breaks down. However, when merging the bare electron with the many-body interactions to form a new ‘quasi-particle’, the main conclusions of the independent electron approximation remain valid. The influence of many-body interactions like electron-electron and electron-phonon scattering is then expressed in terms of the complex self energy Σ .

The quasiparticle lifetime τ can be determined from the full width at half maximum Γ of the photoemission peaks via $\tau = \hbar/\Gamma$. There are three main contributions to the quasiparticle lifetime [125]: (i) electron-electron scattering Γ_{e-e} , (ii) electron-phonon scattering Γ_{e-ph} , and (iii) impurity scattering Γ_{imp}

$$\Gamma = \Gamma_{e-e} + \Gamma_{e-ph} + \Gamma_{imp}. \quad (3.8)$$

Electron-electron interaction: At $T = 0$ the probability for an electron with $E = E_F$ to scatter with a second electron is zero because there are no unoccupied levels at the Fermi energy, and therefore there is no phase space for this process. Consequently, the lifetime of an electron at E_F at $T = 0$ is infinite. If E is slightly different from E_F this leads to a finite scattering rate of order $(E - E_F)^2$. At $T > 0$ there will be partially occupied levels in a shell of width $k_B T$ around the Fermi level and the scattering rate will become

proportional to $(k_B T)^2$ even at $E = E_F$. This leads to the following scattering rate due to electron-electron interactions [131]:

$$\Gamma_{e-e} = 2\beta[(\pi k_B T)^2 + (E - E_F)^2] \quad (3.9)$$

where β is the electron-electron interaction constant.

Electron-phonon interaction: The lifetime-broadening induced by electron-phonon interactions is given by [132]

$$\Gamma_{e-ph} = 2\pi\lambda k_B T \quad (3.10)$$

for temperatures larger than the Debey temperature, with the electron-phonon coupling constant λ . Apart from a reduced lifetime, electron-phonon scattering leads to a change of the energy dispersion due to the real part of the self energy $E(\vec{k}) = E_k^0 + Re(\Sigma)$. This band renormalization can be expressed as a change of the electronic velocity $v(k) = 1/\hbar(\partial E/\partial k)$. With $v_0 = 1/\hbar(\partial E_k^0/\partial k)$ one finds [131]

$$v(k) = \frac{1}{1 + \lambda} v_0(k) \quad (3.11)$$

where $\lambda = -\partial Re(\Sigma)/\partial E$. Electron-phonon interactions lead to a reduced slope of the quasiparticle band (=kink) around the Fermi level.

Impurity scattering: The increase in line width due to electron-impurity scattering is assumed to be independent of energy E and temperature T but proportional to the impurity concentration. Therefore, we write

$$\Gamma_{imp} = const. \quad (3.12)$$

3.1.5 Angular resolved photoemission spectroscopy

A modern photoemission setup (Fig. 3.3) consists of a light source in the VUV range (gas discharge lamp, laser, or synchrotron radiation) that irradiates the sample. Electrons excited via the photoelectric effect are analyzed with respect to their kinetic energy E_{kin} and their emission angle θ in an electrostatic analyzer. From the kinetic energy the binding energy of the electrons inside the crystal can be calculated using Eq. (3.1). As the in-plane momentum $k_{||}$ is conserved at the crystal-vacuum interface it can be determined directly from the emission angle θ of the photoelectrons via

$$k_{||} = \sqrt{\frac{2m_e E_{kin}}{\hbar^2}} \sin(\theta) \quad (3.13)$$

where m_e is the electron mass, i.e. $k_{||}[\text{\AA}^{-1}] = 0.512\sqrt{E_{kin}[\text{eV}]} \sin(\theta)$. The in-plane momentum is varied by turning the sample around θ and ϕ , respectively, as displayed in Fig. 3.3. Therefore, with ARPES one can directly measure the dispersion $E_B(k_{||})$ of a 2D electron system.

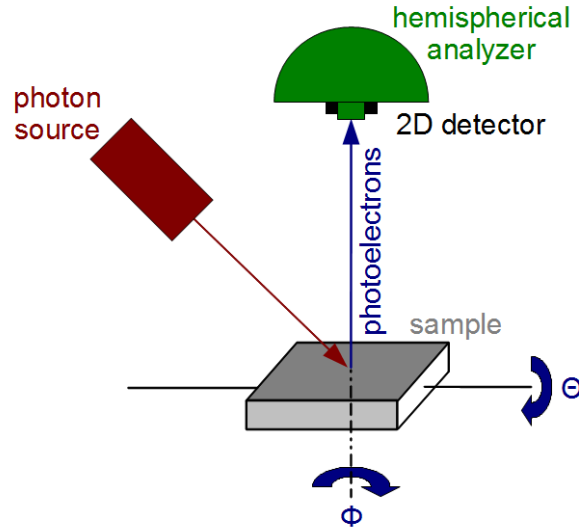


Figure 3.3: Angular resolved photoemission setup: a light source (gas discharge lamp, laser, or synchrotron radiation) emits monochromatic photons of energy $h\nu$ that impinge on the sample surface. Photoelectrons are emitted and focused into a hemispherical analyzer where both kinetic energy and emission angle of the photoelectron are determined. After passing the analyzer the electrons are detected with a 2D CCD camera.

Setup: ARPES experiments have been performed at the Max Planck Institute for Solid State Research in Stuttgart as well as at the Synchrotron Radiation Center (SRC) in Stoughton/WI. The ultra-high vacuum (UHV) chamber in Stuttgart is equipped with a hemispherical SPECS electron analyzer (energy and angular resolution are 10 meV and 0.5° , respectively) and a monochromatized He lamp that offers UV radiation at $h\nu = 21.2\text{ eV}$ (HeI) and $h\nu = 40.8\text{ eV}$ (HeII). The manipulator can be cooled with liquid nitrogen to a base temperature of -180°C .

The measurements at the SRC were done at the variable polarization VLS-PGM beamline. This beamline is equipped with an elliptically polarized Apple II undulator that delivers p- and s-polarization of photons in an energy range from 15 eV to 250 eV. For the ARPES measurements a Scienta analyzer (energy resolution of better than 10 meV, angular resolution of 0.4°) has been used. The manipulator is cooled with liquid helium and reaches temperatures down to $\sim 25\text{ K}$.

The ARPES data in Fig. 7.7 (b), Fig. 7.13 and Fig. 7.14 were measured at the SRC at $T = 100\text{ K}$ [Fig. 7.7 (b)] and $T = 50\text{ K}$ [Fig. 7.13 and Fig. 7.14]. All other ARPES experiments have been performed in Stuttgart. The experiments on the surface alloys and on Bi/Si(111) in chapter 4 and 5 were done at $T = -180^\circ\text{C}$, the graphene measurements in chapter 7 were done at room temperature.

Data analysis: When analyzing photoemission data, either momentum distribution curves (MDCs: photocurrent at constant binding energy as a function of emission an-

gle) or energy distribution curves (EDCs: photocurrent at constant emission angle as a function of binding energy) are considered. Before fitting the photoemission spectra an appropriate background has to be subtracted. In order to do this the measured spectrum has to be separated into the primary spectrum $P(E_{kin})$ and the secondary spectrum that represents inelastic events like electron-electron and electron-ion scattering. Usually it is sufficient to subtract the so-called Shirley background, where the background $B_S(E_{kin})$ at kinetic energy E_{kin} is proportional to the weight of the primary spectrum $P(E_{kin})$ for all kinetic energies $E'_{kin} > E_{kin}$, i.e. [129]

$$B_S(E_{kin}) \propto \int_{E'_{kin} > E_{kin}} P(E'_{kin}) dE'_{kin} \quad (3.14)$$

When fitting EDCs one has to take into account that the photoemission intensity is cut off at the Fermi level E_F by the Fermi function $f(E - E_F, T)$. The Fermi function also includes the experimental broadening of the Fermi edge due to a finite temperature T . The complete fitting function for an EDC is given by

$$I(E) = c + B_S(E) + \left[\sum_i L(E, E_i, \Gamma_i) * G(\Gamma_{res}) \right] f(E - E_F, T) \quad (3.15)$$

The constant offset c accounts for the dark count rate in the detector. $L(E, E_i, \Gamma_i)$ is the Lorentzian from Eq. (3.7) with the peak position at E_i and the full width at half maximum $\Gamma_i = 2Im(\Sigma)$ that describes the single peaks. These have to be convoluted with a Gaussian function $G(\Gamma_{res})$ to account for the experimental resolution Γ_{res} . If $\Gamma_i \gg \Gamma_{res}$ the broadening due to the experimental resolution can be neglected and the spectra can be fitted by

$$I(E) = c + B_S(E) + \sum_i L(E, E_i, \Gamma_i) f(E - E_F, T). \quad (3.16)$$

The fitting function for MDCs reduces to

$$I(k) = c + \sum_i L(k, k_i, \Gamma_{k_i}) \quad (3.17)$$

where the background c includes the dark count rate as well as the Shirley background at the energetic position of the MDC.

3.2 Spin-resolved ARPES

In a spin- and angular resolved photoemission experiment [7, 110, 133] the photoelectrons are first filtered with respect to their kinetic energy and emission angle in a hemispherical analyzer before their spin is determined in a Mott polarimeter. A sketch of the experimental setup is shown in Fig. 3.4. Inside the Mott detector [see Fig. 3.4 (b)] the photoelectrons are scattered by a thin gold foil. Electrons with spin \uparrow (\downarrow) have a higher probability to be

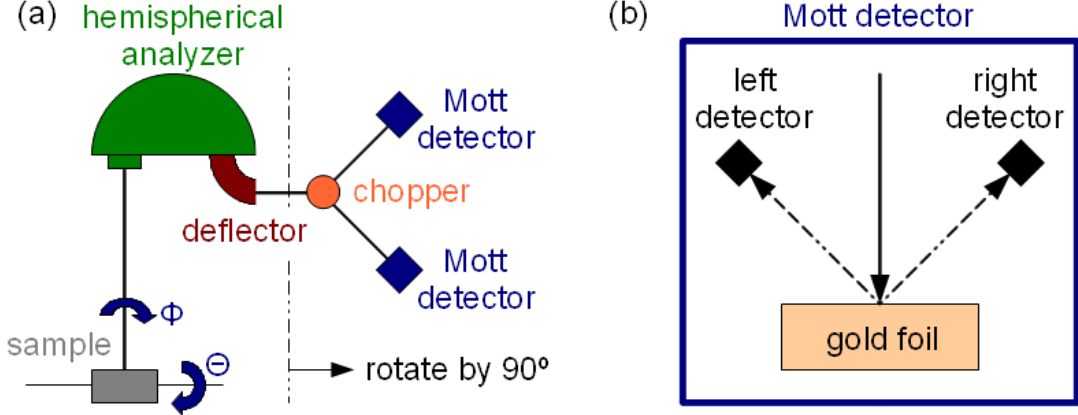


Figure 3.4: (a) SARPES setup: the photoelectrons are filtered with respect to their emission angle and kinetic energy by a hemispherical analyzer. Afterwards the electrons are deflected by 90° and enter the Mott detector, where the electron spin is measured. Within the Mott polarimeter (b) the photoelectrons are scattered into different directions depending on their spin by a thin gold foil. After scattering the electrons are collected by four detectors (left, right, up, and down) and the asymmetries $A_{up,down}$ and $A_{left,right}$ are measured. Therefore, one Mott polarimeter can determine two components of the photoelectron spin. Mounting two Mott detectors under an angle of 90° gives access to all three components of the photoelectron spin. A chopper is used to distribute the photoelectrons evenly between the two Mott polarimeters.

scattered to the left (right). After scattering, the electrons are counted by detectors placed at scattering angles of $\pm 120^\circ$ and the asymmetry $A = (N_{left} - N_{right}) / (N_{left} + N_{right})$ can be calculated, where N_{left} and N_{right} are the number of photoelectrons scattered to the left and right, respectively. The spin-polarization of the photoelectrons is then given by $P = A/S$, where S is the Sherman function. The latter is given by the asymmetry measured for a completely spin-polarized beam of electrons. Present Mott detectors are very inefficient with a Sherman function between 6 and 30% [7]. The spin-resolved intensities I_{up} and I_{down} with respect to the quantization axis determined by the detector arrangement inside the Mott polarimeter can be calculated from the spin-integrated intensity I_{tot} via $I_{up} = I_{tot}(1 + P)/2$ and $I_{down} = I_{tot}(1 - P)/2$. In addition to the left-right asymmetry one can simultaneously measure the up-down asymmetry so that with a single Mott polarimeter one can measure the spin-polarization along two spatial directions. In order to measure all three components of the photoelectron spin two Mott detectors are mounted with an angle of 90° between them [see Fig. 3.4 (a)]. The incoming photoelectrons are evenly distributed between the two Mott detectors with a $\pm 45^\circ$ chopper. The three-dimensional spin vector is measured with respect to the Mott coordinate frame. It needs to be converted into the sample coordinate frame by using a transformation matrix T that depends on the polar angle θ [133].

A spin-resolved ARPES (SARPES) experiment provides four data sets: the integrated intensity I_{tot} and the spin-polarization along the three spatial direction P_x , P_y , and P_z .

The measured spin-polarization, however, depends sensitively on the amount of overlap between adjacent peaks, i.e. on experimental resolution and intrinsic line width, as well as the presence of a nonpolarized background. Therefore, it is difficult to draw any conclusion apart from the existence of spin-polarized bands from the measured data. This problem can be overcome by a sophisticated data analysis [110]. In a first step the spin-integrated data is fitted by an appropriate number of spin-polarized peaks that can be determined from the measured spin-polarization and a background. In a second step, an arbitrary spin-polarization defined by the two polar angles θ and ϕ and the magnitude c is assigned to each peak. From these values the spin-polarization along x , y , and z can be calculated and fitted to the experimental data by optimizing θ , ϕ , and c .

Setup: The SARPES experiments for this work have been performed using the COPHEE setup at the Swiss Light Source in Villigen Switzerland. Spin-resolved measurements were taken with a photon energy of 30 eV with energy and momentum resolutions of 80 meV and 3% of the surface Brillouin zone, respectively. During SARPES measurements the sample was kept at room temperature.

3.3 Core level spectroscopy

Core level spectroscopy is a versatile tool to investigate the chemical composition of a surface and to assign a chemical state to the detected elements [134]. The sample is irradiated by soft x-rays and the photoelectrons are analyzed with respect to their kinetic energies. The binding energy of the electrons can be calculated from Eq. (3.1). As each element has a characteristic set of binding energies the peak positions can be used to identify the elements present at the surface under investigation. From the integrated intensity of the peaks one can determine the concentration of a particular material. Small shifts of the binding energies of a particular peak contain information about the chemical state of the atom. The main peaks in the photoemission spectrum correspond to electrons which leave the surface without energy loss. Electrons that undergo inelastic scattering events contribute to the Shirley background [see Eq. (3.14)].

Apart from photoelectrons, Auger electrons will be excited during the photoemission process. Photoexcitation with soft x-rays creates a hole within a particular core level. During the Auger process this vacancy is filled by an electron from a higher shell. At the same time a second electron is emitted from the sample with a kinetic energy equal to the difference between the energy of the initial core hole and the doubly charged remaining atom. On top of photoelectron and Auger lines additional features appear in the measured spectrum. There are satellite peaks that originate from the emission spectrum of a non-monochromatic x-ray source. Furthermore, shake-up lines are created when the remaining ion is left in an excited state after the photoemission process. The kinetic energy of the emitted photoelectron in this case is reduced by the energy difference between ground state and excited state of the ion. Additional energy loss lines appear if the photoelectron interacts with plasmons of the conduction electrons on its way towards the crystal-vacuum

interface. In this case, the energy difference between the primary peak and the loss peak corresponds to the plasmon energy.

Chemical composition: When interpreting XPS data the first step is the identification of the chemical species present at the surface by comparing the measured peak positions to reference spectra (e.g. from Ref. [134]). If in doubt one can check the conclusion by looking at the spin doublets for p , d , and f lines. They should have the correct separation and intensity ratios.

Identification of chemical states: As the chemical environment of a particular atom affects the binding energy of its core levels one can determine the chemical state of an atom from an accurate determination of the peak position.

Quantitative analysis: The integrated intensity of a given peak I depends on the concentration of atoms of a given element n and the so-called atomic sensitivity factor. However, the sensitivity factor is determined not only by element specific properties like the photoelectric cross section but also by instrumental parameters like the x-ray flux and the detection efficiency. Therefore, the use of atomic sensitivity factors in the determination of n leads to semiquantitative results with an accuracy between 10 and 20% only. However, relative concentrations can be determined with a very high accuracy by comparing the integrated intensities of the respective core levels.

Setup: Core level spectra were measured both at the Max Planck Institute for Solid State Research in Stuttgart as well as at the SRC in Stoughton/WI. The XPS measurements in Stuttgart have been used mainly to check the cleanliness of the substrate and to determine adsorbate coverages. These measurements have been performed at room temperature using non-monochromatized Mg $K\alpha$ radiation at $h\nu = 1253$ eV. The core level data in Fig. 7.9 (b) were measured at the SCR using $h\nu = 150$ eV.

3.4 Low energy electron diffraction

Low energy electron diffraction (LEED) is the ideal tool to investigate the atomic structure at a crystal surface. In the energy range between 0 – 500 eV the mean free path of electrons inside the crystal is limited to a few Å (see Fig. 3.1) and the de Broglie wavelength of the electrons $\lambda = h/p$ matches the crystal lattice constant. Fig. 3.5 (b) shows a sketch of the experimental setup. The electron gun shown in blue creates a beam of monochromatic electrons that impinges on the sample at normal incidence. The elastically scattered electrons can pass the LEED optics and are imaged on a fluorescent screen. The LEED optics consist of several different grids. The first grid is grounded to shield the sample from the high electric fields on the luminescent screen. The second grid is set to a voltage just below the acceleration voltage of the incident electrons to remove inelastically

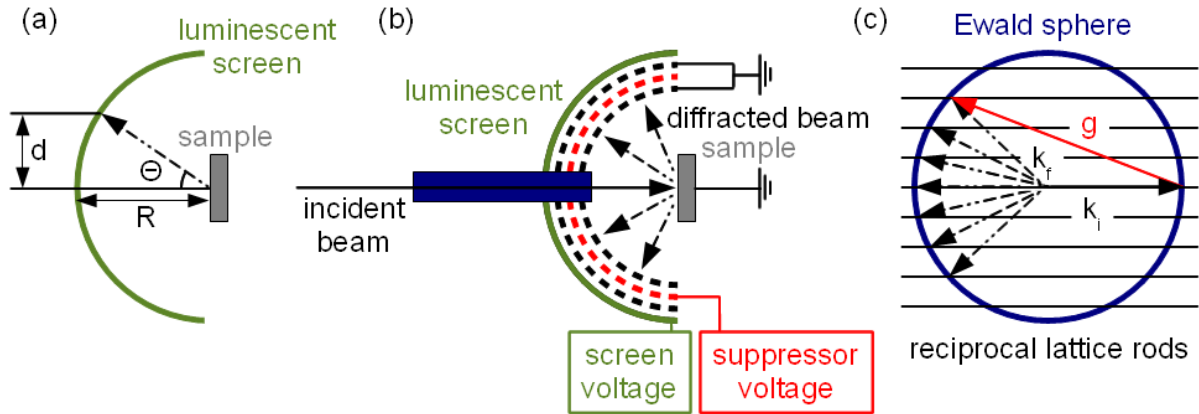


Figure 3.5: (a) The diffraction pattern is an image of the reciprocal lattice. From the position of the intensity maxima on the LEED screen the unit vectors in reciprocal space can be calculated. (b) Experimental setup for LEED: an electron gun (blue) creates the incident beam of monochromatic electrons that are diffracted by the sample (gray) and detected on a luminescent screen (green) (c) Laue condition for the existence of a diffracted beam $\vec{k}_i - \vec{k}_f = \vec{g}$ illustrated graphically.

scattered electrons from the diffracted beam. This grid is called the ‘suppressor’. The last grid is grounded again to shield the suppressor from the high voltage on the luminescent screen. After passing this last grid the elastically scattered electrons are accelerated towards the luminescent screen by the screen voltage.

Kinematic theory: For an ideal 2D crystal the reciprocal lattice consists of lattice rods instead of lattice points like in the case of a 3D crystal. The Laue condition for the existence of a diffracted beam is given by [14]

$$\vec{k}_i - \vec{k}_f = \vec{g} \quad (3.18)$$

where \vec{k}_i and \vec{k}_f are the wave vector of the incident and scattered electron, respectively, and \vec{g} is a reciprocal lattice vector. This is illustrated in Fig. 3.5 (c) by means of the Ewald sphere. The reciprocal lattice rods are shown in black. The radius $|\vec{k}_i|$ of the Ewald sphere (blue) depends on the energy of the incident electrons. The direction of the incident electrons is indicated by \vec{k}_i . Every time when the Ewald sphere crosses the reciprocal lattice rods the Laue condition (3.18) is fulfilled and the electrons are diffracted. The position of the diffracted beam on the LEED screen can be calculated via $d = R \sin(\theta)$ [see Fig. 3.5 (a)] with $\sin(\theta) = \pi \hbar / (g \sqrt{2mE})$, where $g = |\vec{g}|$ is the corresponding distance in reciprocal space, and E is the kinetic energy of the electrons. Upon increasing the energy of the incident electrons the diffraction spots move towards the center of the LEED screen. Whithin the framework of this so-called ‘kinematic’ theory the intensity of the diffracted

beam is simply given by the absolute square of the structure factor F [14]

$$I \propto |F|^2 = \left| \sum_i f_i e^{-i\vec{g}\vec{r}_i} \right|^2 \quad (3.19)$$

where \vec{r}_i is the position of atom i . The atomic scattering factor f_i is assumed to be constant, and the intensity of a given diffracted beam is independent of the energy. The diffraction pattern observed on the luminescent screen is simply a cut through the reciprocal lattice that reflects the size, the shape, and the symmetry of the unit cell in real space.

Dynamical theory: As the incident electrons in a LEED experiment probe the first few atomic layers of the sample they do not see a strictly 2D system but a mixture between continuous rods and discrete lattice points. Therefore, the intensity of the diffracted spots becomes energy-dependent, and the assumption of a constant atomic scattering factor is not adequate any longer. A more appropriate description of the atomic scattering factor can be obtained by expanding the atomic scattering factor as a function of partial waves with orbital momentum l . For a spherically symmetric scattering potential the atomic scattering factor is given by [135]

$$f_l(k) = \frac{1}{k} \sum_{l=0}^{\infty} (2l+1) e^{i\delta_l(k)} \sin(\delta_l(k)) P_l(\cos(\theta)) \quad (3.20)$$

where δ_l is the scattering phase shift between incoming and outgoing wave, and P_l are the Legendre polynomials. Another drawback of the kinematic theory of diffraction is the neglect of multiple scattering and refraction at the crystal-vacuum interface. This is remedied by the dynamical theory of diffraction where a realistic model for the atomic scattering factor [Eq. (3.20)] as well as multiple scattering and refraction of the electrons are included. Using the dynamical theory of diffraction one can calculate the intensity I of a particular diffraction spot as a function of electron energy that is determined by the acceleration voltage V . By comparing experimentally measured $I(V)$ -spectra to dynamical calculations a precise determination of the atomic positions in the first few layers of the crystal can be achieved.

Dynamical $I(V)$ -LEED calculations consist of three major steps: first the scattering of a single atom is calculated using Eq. (3.20). The number of phase shifts δ_l that has to be included depends on the scattering atom. For a scattering potential of sufficiently short range the number of phase shifts δ_l that have to be included in Eq. (3.20) can be estimated as follows [135]. In a classical picture, there will be no scattering event if the scattering parameter b is larger than the range of the potential R_0 (see Fig. 3.6). If the particles are scattered by a spherically symmetric potential the classical angular momentum is conserved $|\vec{L}| = |\vec{r} \times \vec{p}| = \text{const.} = b\sqrt{2mE}$. For $b < R_0$ the maximum angular momentum is limited to $|L| \leq R_0\sqrt{2mE}$. Making use of the correspondence principle we find that the quantized angular momentum l is limited to $l \leq \sqrt{l(l+1)} \leq 1/\hbar R_0\sqrt{2mE} = kR_0$. This means that the sum in Eq. (3.20) can be truncated at $l = kR_0$. In a second step the atoms

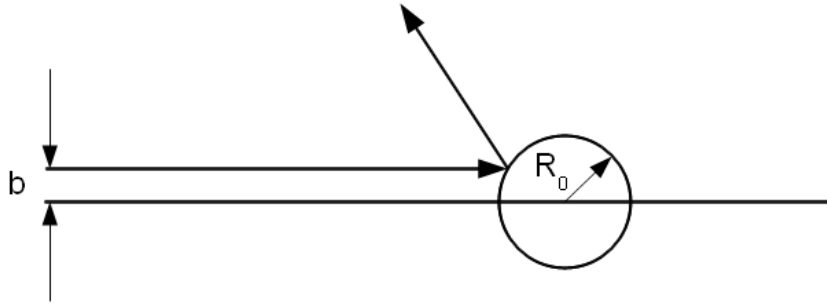


Figure 3.6: A classical particle is scattered by the potential V if the scattering parameter b is smaller than the range of the potential R_0 .

are assembled in a 2D layer and the diffraction pattern is calculated including multiple scattering within this layer. The 2D layer is described by a muffin-tin potential that consists of spherical potentials with range R_0 centered at the ion cores and has a constant value V_0 (real part of the inner potential) everywhere else. This real part of the inner potential is responsible for the refraction of electrons at the crystal-vacuum interface. Finally, the 2D layers are stacked to form a 3D crystal. Again, the diffraction pattern is calculated including multiple scattering between adjacent layers and the limited penetration depth of the electrons is taken into account via the imaginary part V_{0i} of the inner potential. Apart from structural parameters and the inner potential, the effects of a finite temperature T have to be included via the Debye-Waller factor $e^{-2M} = e^{-\Delta q^2 T / \Theta_D^2}$, where Δq is the momentum transfer and Θ_D is the Debye-temperature.

The most intense peaks of the dynamical $I(V)$ spectrum are — after an appropriate shift in energy caused by refraction at the crystal-vacuum interface — located at the energies where the 3D Laue equation is fulfilled. Due to multiple scattering events, however, a dynamical $I(V)$ -spectrum contains much more peaks than a kinematic spectrum.

Structure determination using $I(V)$ -LEED: Every $I(V)$ -LEED calculation starts with guessing a model structure. Then, the $I(V)$ -spectra for this model structure are calculated using the method described in the previous paragraph. Finally, the calculated $I(V)$ -curves are compared with the measured curves with the help of a reliability factor (R -factor). If the agreement is bad one starts again from the beginning with a modified structural model. If the agreement is satisfying the chances are high that one has found the correct structure.

The most commonly used reliability factor is the one introduced by Pendry [136]. The advantage of the Pendry R_P -factor is its sensitivity to the peak positions, whereas the absolute values of the peak intensities are not considered. Instead, the R_P -factor is sensitive to relative intensities. The Pendry R_P -factor is defined as

$$R_P = \frac{\sum_{\vec{g}} \int (Y_{\vec{g},exp.} - Y_{\vec{g},calc.})^2 dE}{\sum_{\vec{g}} \int (Y_{\vec{g},exp.} + Y_{\vec{g},calc.})^2 dE} \quad (3.21)$$

where the Y -functions are given by $Y(E) = L^{-1}(E)/(L^{-2}(E) + V_{0i}^2)$ with the logarithmic derivative of the intensities $L(E) = I'(E)/I(E)$. $R_P = 0$ for perfect agreement, and $R_P = 1$ if the measured and calculated $I(V)$ -curves are completely uncorrelated. An overall R_P -factor below 0.2 generally implies good agreement.

Apart from the surface structure $I(V)$ -LEED also determines a number of non-structural parameters like the real and imaginary part of the inner potential and the surface Debye temperature. The variance σ of the R_P -factor allows an estimation of the confidence interval of the model parameters used in the $I(V)$ -LEED calculations.

Setup and details about the calculations: LEED measurements were done using an ErLEED 1000-A at $T = 77$ K. During LEED measurements magnetic stray fields were compensated using Helmholtz coils to assure perpendicular incidence of the electrons on the sample for all kinetic energies.

The LEED calculations in the present work were performed using the Barbieri/Van Hove SATLEED package [137]. The necessary fourteen phase shifts were determined with the Barbieri/Van Hove phase shift package [138]. Temperature effects were calculated within the SATLEED code by multiplying each atoms scattering amplitude by a Debye-Waller factor. Pendry reliability R_P -factors [136] were used to measure the level of agreement between measured and calculated $I(V)$ -LEED spectra and statistical errors in analysis were estimated with Pendry RR -factors [136].

3.5 First-principles calculations

In a first step the surface geometry is determined from first-principles using the VIENNA AB-INITIO SIMULATION PACKAGE (VASP) which provides precise total energies and forces [139]. Electronic structure calculations have been performed within the framework of relativistic multiple-scattering theory (layer Korringa-Kohn-Rostoker method (KKR) [140, 141]) using the Perdew-Wang exchange-correlation potential [142]. The self-consistent potentials serve as input for the photoemission calculations, which rely on the relativistic one-step model [140, 143]. Thus, all essential ingredients of the excitation process are captured, in particular transition matrix elements and boundary conditions.

Chapter 4

Surface alloys

Structure The deposition of $1/3$ of a monolayer of (Bi,Pb,Sb) on Ag(111) results in the formation of a long range ordered surface alloy where every third atom in the Ag(111) surface is replaced by an alloy atom. The resulting $(\sqrt{3} \times \sqrt{3})R30^\circ$ structure is shown in Fig. 2.6. The surface alloy exhibits a large corrugation due to the outward relaxation Δz of the alloy atoms. In contrast to the Bi/Ag(111) and Pb/Ag(111) surface alloys that always form with face-centered cubic (fcc) toplayer stacking, the Sb/Ag(111) surface alloy can be formed with either fcc or hexagonal close-packed (hcp) toplayer stacking [144,145].

Band structure The surface state of clean Ag(111) has a parabolic shape with an effective mass of $0.42 m_e$ [99] and a Fermi energy of 63 meV at 30 K [94]. Upon adsorption of $1/3$ of a monolayer of Bi, Pb or Sb the surface state dispersion changes dramatically. Instead of a single doubly degenerate parabola one finds a RB-type dispersion consisting of two spin-polarized bands with a characteristic momentum offset k_R (see Fig. 4.1). The band structure of the (Bi,Pb,Sb)/Ag(111) surface alloys consist of three pairs of spin-split states. The pair with the largest binding energy [completely occupied in Bi/Ag(111)] and

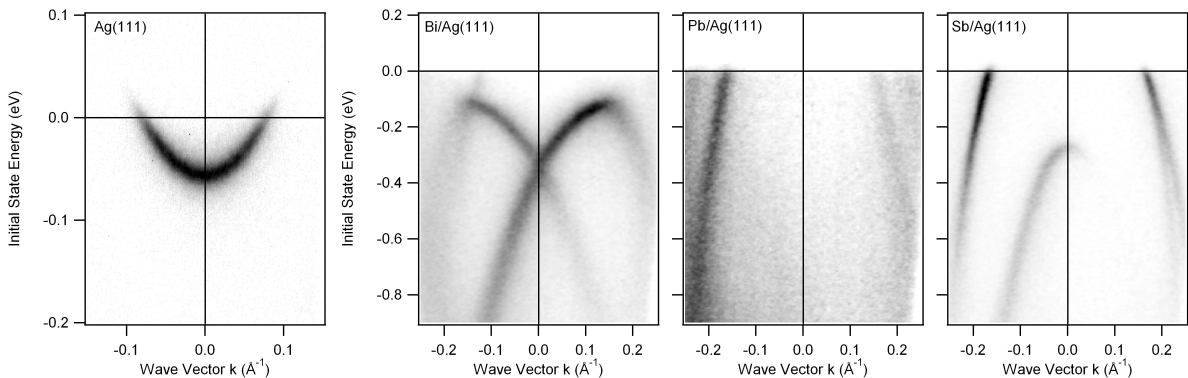


Figure 4.1: Surface state dispersion at the $\bar{\Gamma}$ -point of the surface Brillouin zone for Ag(111) and the three surface alloys Bi/Ag(111), Pb/Ag(111), and Sb/Ag(111).

	k_R (\AA^{-1})	E_R (meV)	α_R (eV \AA)	m^* (m_e)	E_0 (eV)	Ref.
Bi/Ag(111)	0.13	200	3.2	-0.31	-0.135	[5]
Pb/Ag(111)	0.03	23	1.52	-0.15	+0.654	[3, 4, 6]
Sb/Ag(111)	0.005	1	0.38	-0.10	-0.28	[107, 146]

Table 4.1: Characteristic parameters for the sp_z surface state of the different surface alloys on Ag(111).

Sb/Ag(111), partially occupied in Pb/Ag(111)] has mainly sp_z orbital character. At higher binding energy we find two p_{xy} -states with $m_j = 1/2$ (partially occupied) and $m_j = 3/2$ (unoccupied), respectively. Table 4.1 summarizes the characteristic parameters for the sp_z -band in the (Bi,Pb,Sb)/Ag(111) surface alloys.

Sample preparation The Ag(111) substrate was cleaned using several sputtering/annealing cycles (sputtering with 1 keV Ar ions at an Ar pressure of 1×10^{-6} mbar followed by annealing at 530°C). Cleanliness of the substrate was controlled with XPS. In addition, the surface state of clean Ag(111) was monitored with ARPES. One third of a monolayer of Bi, Pb, or Sb was deposited using a commercial electron beam evaporator. The substrate temperature during deposition was 420°C, 350°C, and 250°C for Bi, Pb and Sb, respectively. After deposition the LEED pattern showed a sharp $(\sqrt{3} \times \sqrt{3})R30^\circ$ structure. For the preparation of the mixed $\text{Bi}_x\text{Sb}_{1-x}/\text{Ag}(111)$ surface alloy, Sb and Bi were successively deposited at 250°C and 150°C, respectively.

Origin of giant RB-type spin splitting in surface alloys The strong enhancement of the RB-type spin splitting was attributed to the integration of heavy atoms into the Ag(111) surface and the considerable corrugation caused by the outward relaxation of the Bi/Pb atoms [5, 109]. Furthermore, the corrugation of the surface potential results in a spin-polarization component normal to the surface [147] which was recently observed by spin-resolved ARPES [110]. In the free electron RB model this can be understood as originating from an in-plane component of ∇V resulting from an in-plane inversion asymmetry. The combination of both in-plane and out-of-plane inversion asymmetry leads to a strong enhancement of the spin splitting in a nearly free electron model [111].

Despite the similar atomic SOI ($\zeta_{6p} = 1.25$ eV for Bi and $\zeta_{6p} = 0.91$ eV for Pb [148]), the momentum offset for Bi/Ag(111) [5] is a factor of four larger than in Pb/Ag(111) [3]. This has to be attributed to a different outward relaxation of the Bi and Pb atoms [109, 146] and will be discussed in more detail in the next section. In this section we will address the atomic contribution to the RB-type spin splitting by comparing the surface alloys Bi/Ag(111) and Sb/Ag(111).

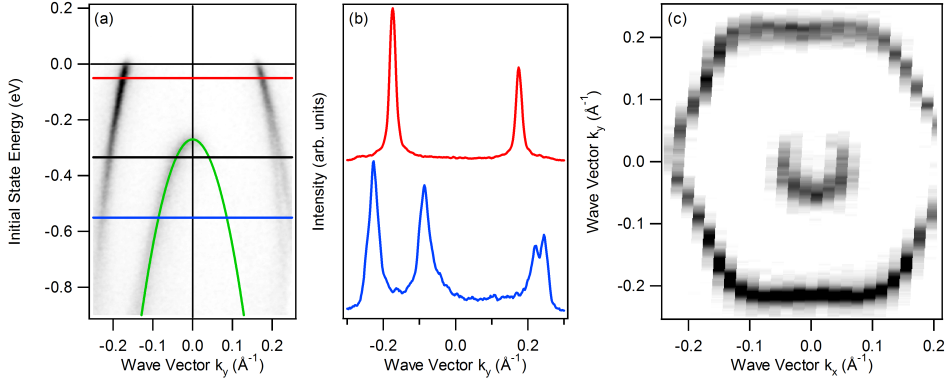


Figure 4.2: (a) Measured band structure around $\bar{\Gamma}$ for the Sb/Ag(111) surface alloy. The green line represents a parabolic fit with $m^* = -0.1m_e$ and $E_0 = -0.27$ eV. (b) Momentum distribution curves at -0.05 eV (red) and -0.55 eV (blue) initial state energy, respectively. These energies are marked by red/blue lines in the measured band structure shown in panel (a). Panel (c) shows a constant energy contour at $E = -0.33$ eV. This energy is marked with a black line in panel (a).

4.1 Atomic contribution to the Rashba splitting

One important difference between (Bi,Pb,Sb)/Ag(111) is the mass of the alloy atom. Bi and Pb have a similar atomic weight ($Z_{\text{Bi}} = 83$ and $Z_{\text{Pb}} = 82$), whereas Sb is considerably lighter ($Z_{\text{Sb}} = 51$). The lighter mass of the Sb atom directly results in a smaller atomic SOI ($\zeta_{5p} = 0.4$ eV [148]). Therefore, Sb/Ag(111) provides an almost ideal opportunity to assess the role of the atomic contribution to the RB-type spin splitting in surface alloys.

The energy dispersion for the Sb/Ag(111) surface alloy is shown in the right panel of Fig. 4.1 as well as in Fig. 4.2 (a). The maximum of the lower sp_z -band is located at an initial state energy of -0.27 eV and the dispersion is well approximated by a parabolic fit with effective mass $m^* = -0.1m_e$ [see green parabola in Fig. 4.2 (a)]. The upper p_{xy} -band forms a hole pocket at $\bar{\Gamma}$. It crosses the Fermi level at $k_F = \pm 0.17 \text{ \AA}^{-1}$. In contrast to the Bi/Ag(111) and Pb/Ag(111) surface alloy the spin splitting of the lower sp_z -band cannot be resolved for Sb/Ag(111). (Recent SARPES experiments revealed a small splitting of $k_R = 0.005 \text{ \AA}^{-1}$ [107]). The upper p_{xy} -band, however, shows a small spin splitting for $E < -0.3$ eV. The different slopes for the two spin-polarized p_{xy} -bands suggest that these bands cross in the vicinity of the Fermi level. Such a crossing has not been observed in the Bi/Ag(111) and Pb/Ag(111) surface alloy, where the spin-polarized bands only cross at high symmetry points $\bar{\Gamma}$ and \bar{M} . These qualitative conclusions are confirmed by MDCs extracted from the intensity map in Fig. 4.2 (a) at the position of the horizontal lines at $E = -0.05$ eV (red) and $E = -0.55$ eV (blue). At -0.05 eV the line cuts only the upper band, and the corresponding MDC exhibits two sharp peaks on opposite sides of $\bar{\Gamma}$ with nearly Lorentzian line shapes. The MDC at -0.55 eV cuts both bands and reveals the splitting of the upper p_{xy} -band.

While the Sb/Ag(111) bands are approximately free-electron like near the center of

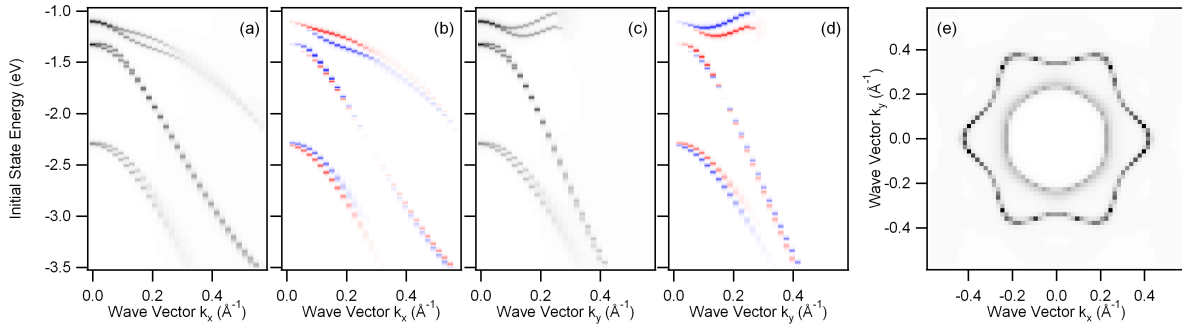


Figure 4.3: Calculated band structure for the Sb/Ag(111) surface alloy along k_x (a) and k_y (c), respectively, together with the corresponding spin-polarization in panel (b) and (d). Blue (red) corresponds to spin up (down). Panel (e) shows a constant energy contour at $E = -3$ eV.

the Brillouin zone, the dispersion is strongly affected by the lattice potential at larger $k_{||}$ values. The departure from an isotropic dispersion can be seen on the constant energy contour displayed in Fig. 4.2 (c). The smaller contour with a circular shape belongs to the lower sp_z -bands. The larger hexagonally-shaped contour belongs to the upper p_{xy} -bands.

Figure 4.3 displays the result of first principle electronic structure calculations. It is well known that the size of the spin splitting depends sensitively on the outward relaxation Δz of the alloy atoms. The atomic positions as computed using the VASP yielded an outward relaxation of the Sb atoms of $\Delta z = 0.24$ Å. This value is significantly larger than the values found previously (0.03 Å SXR [149], 0.07 Å $I(V)$ -LEED [150], 0.03 Å MEIS [144]) indicating that the VASP might overestimate the outward relaxation. Figure 4.3 (a) and (c) show the calculated dispersion for the Sb/Ag(111) surface alloy along k_x and k_y , respectively, together with the corresponding spin-polarization in panel (b) and (d), where blue (red) represents spin up (down). The spin polarization of the surface states is mainly in plane and normal to the wave vector in agreement with the RB model. Apart from a constant shift in energy the dispersion of the calculated bands follows nicely the experimental data. The spin splitting, evident in panel (b) and (d), is barely visible in the total density maps in panel (a) and (c). The calculation also reproduces the anomalous crossing in the upper p_{xy} -band (it occurs in the vicinity of the Fermi level, in the region showing vanishing spin polarization) as well as the anisotropy of the constant energy contour [see Fig. 4.3 (e)]. Furthermore, the calculation reveals a third set of bands at higher energies which is ascribed to p_{xy} ($m_j = 3/2$) states.

The orbital hybridization deduced from the first-principles electronic structure calculations indicates a similar (25%) admixture of p_{xy} -character to the sp_z -bands for both the Sb/Ag(111) and the Bi/Ag(111) systems. However, the ($p_{xy} : sp_z$)-ratio in the lower sp_z -band depends sensitively on the outward relaxation of the alloy atoms Δz , which might be overestimated by the VASP. Nevertheless, the difference in the size of the spin splitting in Sb/Ag(111) and Bi/Ag(111) has to be attributed — at least partly — to the difference in the atomic SOI.

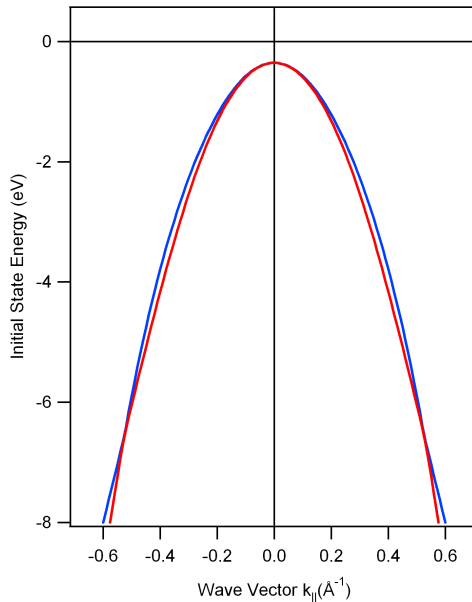


Figure 4.4: 2D nearly free electron gas subjected to an in-plane inversion asymmetry. The band dispersion becomes non-parabolic, and the two spin-polarized bands shown in red and blue, respectively, cross away from the $\bar{\Gamma}$ point.

Although the first-principles calculations nearly perfectly reproduce the experimental results, the origin of the observed spin splitting is difficult to grasp. It becomes more obvious in a recently developed nearly free electron (NFE) model [111]. There, the contributions to the spin splitting from a structural inversion asymmetry in the plane as well as perpendicular to the plane of the 2DEG can be switched on and off separately so that their mutual interplay can be analyzed. If we calculate the band dispersion for an in-plane inversion asymmetry only, we can reproduce the band crossing away from the $\bar{\Gamma}$ point. The result is displayed in Fig. 4.4. As the perpendicular gradient is set to zero in this case, there is no momentum offset of the band maximum away from $\bar{\Gamma}$. The anomalous band crossing at $k \neq 0$ can be attributed to the fact that the in-plane inversion asymmetry results in a non-parabolic dispersion. Similar to the Bi/Ag(111) surface alloy, the in-plane inversion asymmetry in Sb/Ag(111) is a consequence of the threefold rotational symmetry of Ag(111) substrate and the outward relaxation of the Sb atoms. The presence of an in-plane inversion asymmetry becomes also apparent from the hexagonal shape of the constant energy contour in Fig. 4.2 (c). From the NFE model we qualitatively conclude that in Sb/Ag(111) there is a strong in-plane inversion asymmetry which is comparable to Bi/Ag(111), but since the atomic SOI in Sb is much weaker than in Bi, a strong enhancement of the spin splitting cannot be expected.

Using $k_R = 0.005 \text{ \AA}^{-1}$ as recently determined by spin-resolved ARPES [107] results in a Rashba constant $\alpha_R = 0.38 \text{ eV \AA}$. The ratio between the atomic SOI for Bi and for Sb $\zeta_{Bi} : \zeta_{Sb} \approx 3$ cannot completely explain the large difference in α_R as $\alpha_R(Bi/Ag) : \alpha_R(Sb/Ag) \approx 8$. Therefore, there has to be an additional parameter apart from the atomic

SOI that influences the size of the spin splitting. This additional parameter is the outward relaxation of the alloy atoms as will be discussed in more detail in the next section.

4.2 Structural influence on the Rashba splitting

The RB-type spin splitting relies on different contributions, such as a strong atomic spin-orbit interaction, a structural inversion asymmetry as well as other structural parameters (e. g., corrugation, relaxation, orbital character) [85,109,125,133,151,152]. The importance of detailed structural considerations, which are completely neglected in the framework of the NFE RB model, becomes obvious when comparing silver and antimony. The surface states on the (111) surfaces of these elements exhibit substantially different spin splittings (the one in Ag(111) being much smaller than in Sb(111) [96,125,153]) although the atomic spin-orbit parameters differ only by a factor of four ($\zeta_{Ag} = 0.11$ eV [154] and $\zeta_{Sb} = 0.40$ eV [148]). Since surface potential gradient and atomic spin-orbit coupling can be considered to be of the same order of magnitude, the reason for this difference in spin splitting must be sought in the structure. The fcc structure of Ag features a smooth hexagonal lattice at the (111) surface, whereas the rhombohedral structure of Sb(111) with two atoms in the basis grows in a bilayer configuration stacked along the [111] direction resulting in a corrugated surface [155]. Hence, structural considerations have to be taken into account for a better understanding of the RB-type spin splitting in surface states. For systems with a similar crystal structure like Bi and Sb the different size of the spin splitting can be attributed to the difference in atomic mass [95,96,156]. Further, even though the atomic spin-orbit coupling is vanishingly small in graphene or carbon nanotubes, it has been shown that the spin-orbit interaction can be structurally enhanced by the local curvature in their structure [152,157,176].

Surface alloys like (Bi,Pb,Sb)/Ag(111) show an extremely large RB-type spin splitting [3,5,6,108,158]. Interestingly, only a fraction of the atoms at the surface feature a sizable atomic SOI so that here as well the source of the large spin splitting must be sought in the structure. Motivated by this and by theoretical considerations about the relaxation dependence of the spin splitting [109] we present a systematic study of the alloy atom relaxation in different Ag(111) surface alloys using $I(V)$ -LEED measurements and simulations. We relate the dopant atom relaxation to the size of the spin splitting and address a number of other unresolved issues in the literature. These include the band assignment of the bands crossing the Fermi level in the Pb/Ag(111) surface alloy, hcp and fcc toplayer stacking in the Sb/Ag(111) surface alloy as well as the Bi atom relaxation in the Ag(111) and Cu(111) surface alloys.

We measured $I(V)$ -LEED spectra for the surface alloys Bi/Ag(111), Pb/Ag(111) and Sb/Ag(111). The corresponding simulations were done for two different surface alloy structures: the unfaulted (fcc) substitutional surface alloy and the faulted (hcp) substitutional surface alloy. The decision between fcc and hcp toplayer stacking was made by comparing the reliability R_P -factors for both structures. For the rejected structures the R_P -factors were in all cases more than double to those of the finally chosen structures.

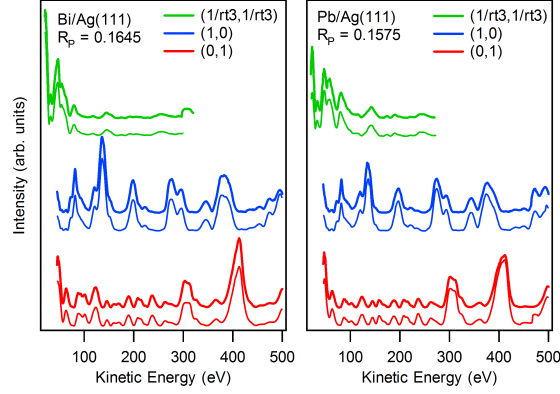


Figure 4.5: $I(V)$ -LEED data (thick lines) for the $(\sqrt{3} \times \sqrt{3})R30^\circ$ phase of Bi (left) and Pb (right) on Ag(111) are displayed together with the corresponding calculated $I(V)$ -LEED spectra (thin lines).

During the simulations surface geometry, Debye temperatures and real part of the inner potential were optimized by fitting the theoretical $I(V)$ -LEED curves to the measured ones. In every step the geometry of the four highest layers was calculated as a $(\sqrt{3} \times \sqrt{3})$ unit cell. The symmetry restricts the degrees of freedom to the component normal to the surface and also forbids buckling for most layers. Three Debye temperatures T_D were fitted for each measurement: one for the top layer Ag atoms, one for the top layer Pb/Bi/Sb atoms and one for all the other Ag atoms. The real part of the inner potential was found to be approximately 6 eV for all calculations. The imaginary part of the potential was kept at a fixed value of 4.5 eV.

Fig. 4.5 shows the integrated intensity of the three equivalent (0,1) and (1,0) spots and the six equivalent $(1/\sqrt{3}, 1/\sqrt{3})$ spots as a function of electron energy for the Bi/Ag(111) and Pb/Ag(111) surface alloys. The data were averaged over three (six) equivalent spots and smoothed. During data smoothing each data point was replaced by the average with its two neighbors. This smoothing procedure was repeated 20 times. The $I(V)$ -LEED spectra for both Bi/Ag(111) and Pb/Ag(111) surface alloys differ only in detail indicating that they form the same $(\sqrt{3} \times \sqrt{3})R30^\circ$ structure. For the Sb/Ag(111) surface alloy two different phases are known from the literature, which differ in the toplayer stacking [144, 150, 159]. One phase grows in regular fcc stacking while the other phase grows in hcp stacking. The $I(V)$ -LEED spectra for the two Sb/Ag(111) surface alloys, which have been treated in analogy to the spectra in Fig. 4.5 (b), are shown in Fig. 4.6 (a). The thick and thin lines in the graphs correspond to the experimental and calculated spectra, respectively. It can be seen that for all surface alloys the calculated spectra fit very well to the experimental data resulting in low R_P -factors. Only the R_P -factor for the hcp-phase of the Sb/Ag(111) is somewhat higher, which we attribute to some fcc-domains being present at the surface.

The structural parameters resulting from the calculated $I(V)$ -LEED spectra are summarized in Table 4.2 along with some values from the literature for comparison. The outward relaxation Δz , which is the distance between the alloy atom and the plane of

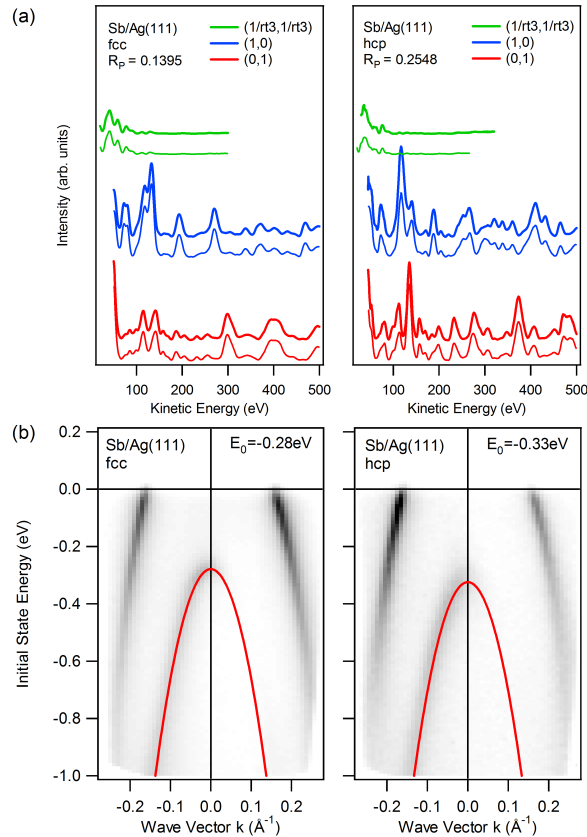


Figure 4.6: Comparison of $I(V)$ -LEED (a) and ARPES (b) data for fcc (left panels) and hcp (right panels) toplayer stacking for the Sb/Ag(111) surface alloys. The red lines in (b) are fits to the experimental data.

the first layer of substrate atoms (see Fig. 2.6), is given for each of the different alloy atoms. In addition, the interlayer distances for the first four layers are summarized. After the fourth layer no significant deviation from the bulk value of 2.36 \AA is expected. The in-plane lattice constants were held fixed. While for the Pb/Ag(111) and Bi/Ag(111) surface alloys the interlayer distances hardly differ from the bulk, it should be noted that in the Sb/Ag(111) surface alloy the distance between the first and the second silver layer is increased by about 0.1 \AA . Furthermore, non-structural parameters that accompany the $I(V)$ -LEED calculations such as the Debye temperatures as well as the real part of the inner potential are given in Table 4.3. As the $I(V)$ -LEED measurements were done at 77 K , which is comparable to the low Debye temperatures, no complications from a too high Debye-Waller factor were anticipated in the calculations.

In the following, we relate the structural findings to the size of the Rashba-type spin splitting. An overview of the typical parameters k_R , α_R , and E_R in the surface alloys on Ag(111) and Cu(111) is given in Table 4.4.

	Δz (Å)	d_{12} (Å)	d_{23} (Å)	d_{34} (Å)	R_P	Ref.
Bi/Ag(111) fcc	0.65 ± 0.10	2.32 ± 0.02	2.33 ± 0.03	2.34 ± 0.04	0.1645	this work
	0.35 (theory)					[5]
	0.85 (theory)					[109]
Pb/Ag(111) fcc	0.46 ± 0.06	2.35 ± 0.02	2.33 ± 0.03	2.34 ± 0.04	0.1575	this work
	0.24 (XRD)					[160]
	0.8 (STM)					[160]
	0.68 (theory)					[160]
	0.42 (theory)					[6]
	0.97 (theory)					[109]
Sb/Ag(111) hcp	0.11 ± 0.05	2.43 ± 0.05	2.34 ± 0.05	2.35 ± 0.06	0.2548	this work
	0.03 (XRD)	2.50				[149]
	0.02 (theory)					[159]
	0.07 (LEED)					[150]
Sb/Ag(111) fcc	0.10 ± 0.02	2.44 ± 0.02	2.33 ± 0.02	2.33 ± 0.03	0.1395	this work
	0.24 (theory)					[158]
Bi/Cu(111) fcc	1.02 (XRD)	2.12	2.10			[161]
	1.06 (theory)					[106]
Sb/Cu(111) hcp	0.47 (MEIS)	2.05				[162]
	0.6 (XRD)	1.98				[149]

Table 4.2: Geometrical parameters of the different surface alloys on Ag(111) and Cu(111) substrates. The outward relaxation Δz is the distance between the alloy atom and the plane of the surface layer. The distances d_{12} , d_{23} , and d_{34} are the distances between the first (=surface) and second layer, the second and third layer, as well as the third and fourth layer, respectively. The bulk interlayer distances are 2.36 Å for Ag(111) and 2.09 Å for Cu(111).

4.2.1 Bi/Ag(111)

With $\Delta z = (0.65 \pm 0.10)$ Å, the Bi/Ag(111) surface alloy shows the largest outward relaxation in the surface alloys considered here on a Ag(111) substrate. So far only two theoretical values have been reported for the relaxation, one of which is smaller while the other is larger than the experimental value (see Table 4.2). The difference between the theoretical values is most likely related to different methods for relaxing the structure. Nevertheless, the corresponding band structure calculations both show good agreement with the experimental data [5, 109].

Calculations have shown that an increased p_{xy} -character in the fully occupied band is responsible for the enhanced spin splitting characterized by a momentum offset of $k_R = 0.13 \text{ \AA}^{-1}$ in Bi/Ag(111) [109]. It was shown that starting from a hypothetical flat Bi/Ag(111) surface alloy the $s : p_z$ -ratio changes in favor of the p_z -character with an admixture of p_{xy} -character upon outward relaxation of the Bi atoms resulting in a stronger spin splitting. Comparing the Bi/Ag(111) surface alloy to the Bi/Cu(111) surface alloy, we find that the structure is qualitatively the same for both surface alloys. However,

	$T_D(\text{Pb/Bi/Sb})(\text{K})$	$T_D(\text{Ag}_1)(\text{K})$	$T_D(\text{Ag}_{2\rightarrow})(\text{K})$	V_R (eV)
Pb/Ag(111) fcc	90	150	180	6.3
Bi/Ag(111) fcc	65	160	210	5.9
Sb/Ag(111) hcp	150	110	230	5.7
Sb/Ag(111) fcc	115	130	200	6.2

Table 4.3: Non structural parameters that have been used in the $I(V)$ -LEED calculation. The Debye temperatures T_D for the different alloy atoms (Pb/Bi/Sb), the surface layer silver atoms (Ag_1), and the silver atoms in the subsequent layers ($\text{Ag}_{2\rightarrow}$) are given along with the real part of the inner potential V_R .

for the Bi/Cu(111) surface alloy outward relaxations of more than one Ångström have been reported (see Table 4.2). The difference in outward relaxation can be attributed to the smaller lattice constant of the Cu substrate. A comparison of the electronic structures shows that the spin splitting $k_R = 0.03 \text{ \AA}^{-1}$ for Bi/Cu(111) is much smaller than for Bi/Ag(111). Furthermore, the surface alloy bands in Bi/Cu(111) are shifted into the unoccupied states, which can be related to a different charge transfer to the surface state from the Cu bulk as compared to the Ag bulk.

4.2.2 Pb/Ag(111)

For the Pb/Ag(111) surface alloy an outward relaxation of $\Delta z = (0.46 \pm 0.06) \text{ \AA}$ has been found. This value lies in between previously reported values excluding the value obtained by STM. STM is generally not very suitable for obtaining structural parameters perpendicular to the surface [160]. Also, in contrast to what has been observed before [160], our $I(V)$ -LEED calculations show that the two lattice sites of the Ag atoms in the $(\sqrt{3} \times \sqrt{3})R30^\circ$ unit cell are equivalent.

The size of the spin splitting for the Pb/Ag(111) surface alloy is still under debate due to different interpretations of the measured ARPES spectra [4, 6, 109, 110, 118]. Depending on the dispersion of the sp_z -band and the p_{xy} -band in the unoccupied states, the occupied states may be assigned to different bands [4, 6, 109]. It has been shown that the position of the sp_z -band is particularly sensitive to the outward relaxation of the Pb atoms [109]. With a calculated outward relaxation of 0.97 \AA , the sp_z -band with $k_R=0.11 \text{ \AA}^{-1}$ and the p_{xy} -band cross without hybridizing (Scenario I). By reducing the relaxation of the Pb atoms to 0.67 \AA , however, the two sets of bands avoid each other resulting in a lower apparent spin splitting (Scenario II) [109]. Other calculations found a relaxation of 0.42 \AA leading to a spin splitting of $k_R=0.04 \text{ \AA}^{-1}$ in good agreement with experiment [6, 7]. Here, no band crossing between the sp_z -band and the p_{xy} -band has been observed. As the experimental outward relaxation found for Pb/Ag(111) is 0.46 \AA , we are inclined to favor the second scenario. This interpretation is further supported by recent spin-resolved ARPES measurements [110].

4.2. Structural influence on the Rashba splitting

	k_R (\AA^{-1})	E_R (meV)	α_R (eV \AA)	Ref.
Sb/Ag(111)	0.005	1	0.38	[107, 158]
Pb/Ag(111)	0.03	23	1.52	[6] (exp)
	0.04	22	1.05	[6] (theor)
	0.11			[109]
Bi/Ag(111)	0.13	200	3.05	[5]
	0.13			[109]
Sb/Cu(111)	0.005	3	0.19	^a
Bi/Cu(111)	0.03	15	1.0	[108]
	0.096			[163]
	0.032	13	0.82	[106] (exp)
	0.028	9	0.62	[106] (theor)
Au(111)	0.012	2.1	0.33	[104]
Ag(111)	0.0007	0.005	0.013	[125]
Cu(111)	0	0	0	^b

Table 4.4: Characteristic parameters for the spin-split states in the different surface alloys on the Ag(111) and Cu(111) surfaces. The different parameters, momentum offset k_R , Rashba energy E_R , and Rashba constant α_R are defined in the text.

^aThese values are estimated as an upper limit from the line width in the momentum distribution of the experimental band structure in Sb/Cu(111)

^bAs we expect the spin splitting in the Cu(111) surface state to be smaller than for the Ag(111) surface state, we have set the values to zero for the purpose of this work.

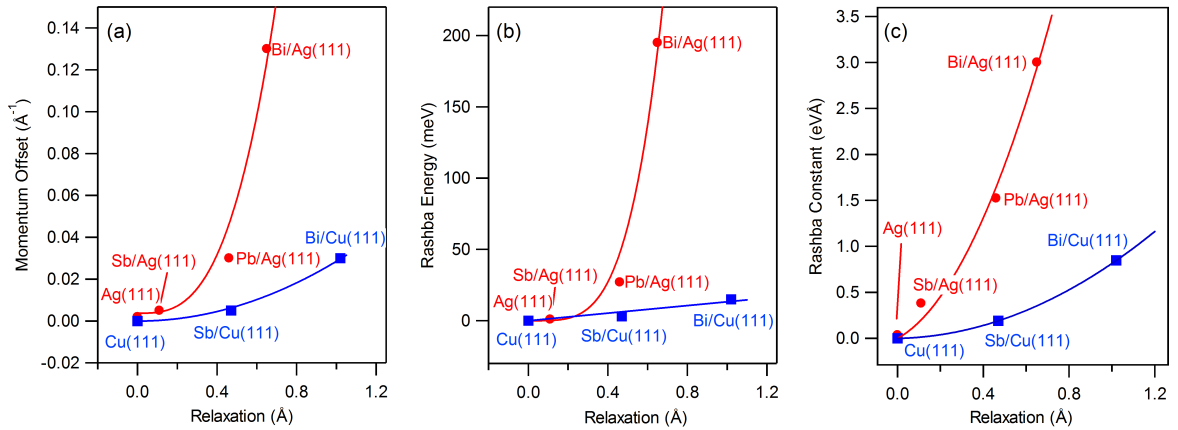


Figure 4.7: Characteristic experimental parameters for a Rashba system, such as momentum offset (a), Rashba Energy (b), and Rashba constant (c) are shown as a function of the outward relaxation Δz . The lines are drawn as a guide to the eye.

4.2.3 Sb/Ag(111)

The Sb/Ag(111) surface alloy can be formed with either fcc or hcp toplayer stacking [144, 159]. However, no reproducible way of creating these two phases has been reported so far. The formation of the hcp toplayer stacking has been attributed to the presence of subsurface stacking faults from previous preparations caused by Sb atom diffusion into the bulk [159]. We have found that it is possible to reproducibly create the two phases separately regardless of the sample preparation history. In the electron beam evaporator used for depositing the Sb atoms, the atom beam is partially ionized by electrons from a filament. A positive voltage at the crucible accelerates the Sb ions towards the grounded sample. The higher the voltage at the crucible, the higher the kinetic energy of the Sb ions and therefore the stronger their impact at the Ag(111) surface. For voltages below +370 V at the Sb crucible as well as for thermal Sb atoms evaporated from a Knudsen cell, we found that the phase with fcc-stacking is formed. For higher voltages the phase with hcp-stacking is formed. It is conceivable that the higher ion energy results in ion implantation into the Ag substrate inducing the subsurface stacking faults that favor the phase with hcp-stacking.

The Sb outward relaxation for the fcc- and hcp-phase is $(0.10 \pm 0.02) \text{ \AA}$ and $(0.11 \pm 0.05) \text{ \AA}$, respectively. These values are similar to what has been previously found for the hcp-phase using $I(V)$ -LEED. In addition, a slight outward relaxation between 0.07 \AA and 0.08 \AA of the surface Ag layer has been observed for both phases. The Ag layer relaxation has also been found by x-ray diffraction (XRD). There the Ag layer relaxation is larger (0.14 \AA), whereas the outward relaxation of the Sb atom is smaller (0.03 \AA) [149]. A similar effect has been observed for the Sb/Cu(111) surface alloy. There, however, the Cu layer relaxation reduces the distance between the surface layer and the substrate [149, 162].

The toplayer stacking also slightly affects the band structure. This can be seen in Fig. 4.6 (b), where the experimental band structure of the two phases for the Sb/Ag(111) surface alloy in the vicinity of the $\bar{\Gamma}$ -point is shown. We observe a small shift of 50 meV between the sp_z -band of the two phases. However, due to the comparatively large error bars we cannot relate this to the outward relaxation. Therefore, we rather attribute this shift to disorder at the surface. This interpretation is also supported by the larger R_P -factor for the hcp-phase.

The spin splitting of the sp_z -band is too small to be detected by conventional ARPES. However, spin-resolved photoemission experiments, which are much more sensitive to a small spin splitting due to the ‘spin-label’ of the bands [110], show that the sp_z -band of the hcp-phase in the Sb/Ag(111) surface alloy is spin-split by $k_R = 0.005 \text{ \AA}^{-1}$ [107]. Unfortunately, no spin splitting has been reported so far for the fcc-phase.

4.2.4 Spin Splitting vs. Relaxation

The large spin splitting in the different surface alloys cannot be accounted for by the spin-orbit interaction in the heavy elements alone. This becomes obvious when comparing them to other materials with a sizable spin splitting, such as Au(111) or Bi(111). The spin

splitting of the surface state on the pristine Ag(111) substrate is undetectable with current experimental techniques. The spin splitting in the Bi/Ag(111) surface alloy is much larger than what has been observed for the Bi(111) surface state, even though only a fraction of the atoms in the surface alloy are Bi atoms. Thus, the simple statement that a strong spin-orbit coupling leads to a large spin splitting does not hold.

In order to resolve this issue the structural details of the different materials have to be considered. As the structure dictates the potential landscape, the orbital overlap as well as the orbital hybridization, it has direct influence on the asymmetry of the wave functions and the corresponding spin splitting in the electronic structure. In Fig. 4.7 (a)–(c) the characteristic parameters for the RB-type spin splitting in the different surface alloys — momentum offset k_R , Rashba energy E_R , and Rashba constant α_R — are plotted as a function of the outward relaxation. The data points for the surface alloys on the Cu(111) and the Ag(111) substrates are drawn in blue squares and red circles, respectively. The solid lines are drawn to guide the eye.

Unfortunately, with experimentally available systems it is difficult to change only one parameter, while leaving everything else constant. Nevertheless, the available data allows us to define the general trend that an increased spin-orbit coupling and an increased outward relaxation leads to an increased spin splitting when considering the Ag(111) and the Cu(111) substrates separately. If we consider that the atomic spin-orbit coupling constant for p -electrons in a hydrogen-like atom is proportional to Z^4/n^3 (Z : atomic number, n : principal quantum number), the increase in the atomic spin-orbit coupling constants of Sb, Pb, and Bi alone cannot account for the increase in the respective Rashba constants. Therefore, we conclude that the structure of the surface alloy, i. e. the outward relaxation, plays a key role in the strength of the spin splitting.

Comparing the surface alloys for the Ag(111) and Cu(111) substrates, the situation is not so straightforward anymore. The Bi/Cu(111) surface alloy shows a much larger outward relaxation, but a much smaller spin splitting than the Bi/Ag(111) surface alloy. It is conceivable that the substrate itself has an influence on the size of the spin splitting. Calculations for the sp_z -states have shown that the substrate atoms within the surface alloy layer carry a significant spectral weight, which has led to the conclusion that the atomic spin-orbit parameter of the substrate contributes to the spin splitting in the corresponding surface alloys [108]. However, in another comparison of the Bi/Ag(111) and the Bi/Cu(111) surface alloy, the spin-orbit coupling of the substrate has been found to play a negligible role in the spin splitting of the surface alloy. The conclusion here was that structural effects (i. e. the outward relaxation of the alloy atom) that change the orbital composition play a dominant role [106]. The difference between Bi/Ag(111) and Bi/Cu(111) could simply originate from the different lattice constants of the substrate. In this regard, a simple tight-binding calculation shows that the Rashba constant is proportional to the lattice constant¹. Another possible explanation is that the spin splitting reaches a maximum with further outward relaxation and then decreases again. In addition, the distance d_{12} between the

¹This results from explicitly considering the lattice constant in the tight-binding calculation presented in Ref. [85].

surface layer and the substrate is compressed for Bi/Ag(111) and expanded for Bi/Cu(111) with respect to the bulk interlayer spacing. Whether this plays a role in the spin splitting for the surface alloys so far is unknown.

The results discussed here show that the outward relaxation plays a key role determining the size of the spin splitting in the surface alloys with the general trend that a larger outward relaxation leads to a larger spin splitting. However, many open questions remain, such as a better understanding of the role of the substrate, the influence of avoided crossings of the bands and the resulting apparent spin splittings as well as the question whether there is a maximum in outward relaxation after which the spin splitting decreases again.

4.3 Mixed surface alloys on Ag(111)

The giant spin splitting in surface alloys results from a strong structural modification at the surface as well as the large atomic spin-orbit interaction (SOI) of the alloy atoms. These surface alloys are an ideal playground to manipulate both the size of the spin splitting as well as the position of the Fermi level as it is possible to change the atomic SOI as well as the relaxation by varying alloy atoms and substrates. For future device applications, it is necessary to tune the size of the spin splitting as well as the position of the Fermi level in such Rashba systems so that the Fermi surface possesses the desired spin texture. A first step in this direction was the experimental proof that the spin splitting (and at the same time the Fermi energy) can be controlled via the Bi content in a mixed $\text{Bi}_x\text{Pb}_{1-x}/\text{Ag}(111)$ surface alloy [6, 7].

In the following we will show by (S)ARPES and $I(V)$ -LEED, that it is possible to form a well-ordered mixed binary $\text{Bi}_x\text{Sb}_{1-x}/\text{Ag}(111)$ surface alloy where the spin splitting can be tuned while leaving the position of the Fermi level largely unaffected. This is an important step towards the realization of a mixed ternary $\text{Bi}_x\text{Pb}_y\text{Sb}_{1-x-y}/\text{Ag}(111)$ surface alloy, where spin splitting and Fermi energy can be tuned independently by varying the material parameters x and y . As a proof of principle we have grown the ternary $\text{Bi}_{0.3}\text{Pb}_{0.35}\text{Sb}_{0.35}/\text{Ag}(111)$ surface alloy and investigated its band structure by (S)ARPES.

The spin splitting k_R in the (Bi,Pb,Sb)/Ag(111) surface alloys increases from Sb via Pb to Bi with increasing mass and increasing outward relaxation Δz of the alloy atom. As Bi and Sb have the same number of valence electrons, i. e. they are isoelectronic, the band maximum E_0 is located at a similar energetic position in the occupied states for the Bi/Ag(111) and the Sb/Ag(111) surface alloys. Pb, however, has one valence electron less than both Bi and Sb. Therefore, the band maximum of the sp_z -state is in the unoccupied states. All the sp_z -states have negative effective masses ranging from $-0.10m_e$ for Sb/Ag(111) to $-0.35m_e$ for Bi/Ag(111).

Mixing Bi and Pb in a binary $\text{Bi}_x\text{Pb}_{1-x}/\text{Ag}(111)$ surface alloy leads to a continuous evolution of the characteristic parameters of the sp_z surface state dispersion with Bi content x [6, 7]. The spin splitting k_R increases with increasing Bi content accompanied by a downward shift of the band maximum into the occupied states. Bi and Sb on the other hand are isoelectronic, i.e. mixing Bi and Sb in a binary $\text{Bi}_x\text{Sb}_{1-x}/\text{Ag}(111)$ surface alloy

would offer the possibility to tune the size of the spin splitting without changing the Fermi level. However, the Sb/Ag(111) surface alloy forms with either fcc or hcp toplayer stacking depending on the growth conditions (see Refs. [144, 146, 159] and section 4.2), whereas Bi/Ag(111) as well as Pb/Ag(111) always form with fcc toplayer stacking. Therefore, it is not *a priori* clear whether a well ordered $\text{Bi}_x\text{Sb}_{1-x}/\text{Ag}(111)$ surface alloy can be formed.

The spin splitting of the sp_z surface state in Sb/Ag(111) is smaller than the line width of the bands which prevents its investigation by conventional spin-integrated ARPES [158]. The discrimination of the two bands, however, can be achieved by SARPES, where the spin polarization P of the photoelectrons is measured in addition to their kinetic energy and the emission angle [133]. Due to the low efficiency of present Mott detectors SARPES measurements are very time-consuming and are therefore usually restricted to single spin-resolved momentum distribution curves (MDCs). The intensities for spin-up (spin-down) electrons I^\uparrow (I^\downarrow) are obtained from the measured spin-integrated intensity I_{tot} according to $I^\uparrow = (1 + P)I_{tot}/2$ and $I^\downarrow = (1 - P)I_{tot}/2$. Assuming a parabolic dispersion, the Rashba splitting k_R is then given by $k_R = \Delta k/2$, where Δk is the \vec{k}_\parallel -distance of the maxima in I^\uparrow and I^\downarrow . Note that $k_R \neq \Delta k/2$ if the dispersion of the bands is not completely parabolic.

4.3.1 Binary surface alloy $\text{Bi}_x\text{Sb}_{1-x}/\text{Ag}(111)$

Figure 4.8 (a) shows the evolution of the surface state band structure for the mixed binary alloys $\text{Bi}_x\text{Sb}_{1-x}/\text{Ag}(111)$ as a function of Bi content x measured with ARPES. The dispersion of the sp_z surface state evolves continuously between $x = 0$ and $x = 1$. Around $x = 0.5$ the line width of the bands increases considerably which we attribute mainly to structural disorder, i.e. to imperfections in the $(\sqrt{3} \times \sqrt{3})R30^\circ$ reconstruction. The position of the lower sp_z -band was determined by fitting MDCs with a Lorentzian and a constant background. The resulting $E(k)$ data were then fitted by parabolas to determine the characteristic Rashba parameters. The continuous evolution of momentum offset k_R , Rashba constant α_R , band maximum E_0 , and effective mass m^* with increasing Bi content x is shown in Fig. 4.8 (b). The Rashba parameter α_R has been calculated from the experimentally determined momentum offset and effective mass.

While k_R , m^* , and α_R continuously increase with x , the band maximum E_0 reaches a maximum at about $x \approx 0.63$ and then decreases again. It is known that E_0 is correlated with the outward relaxation of the Bi and Sb atoms [109]. Because it is unlikely that the outward relaxation of the alloy atoms in the mixed $\text{Bi}_x\text{Sb}_{1-x}/\text{Ag}(111)$ surface alloy is larger than in the pure Bi/Ag(111) surface alloy we attribute the maximum at $x \approx 0.63$ to structural disorder, which is corroborated by the considerable increase in line width.

Recent first-principles calculations are in good agreement with our experimental values for k_R [164]. However, in contrast to experiment the calculations show a continuous increase of E_0 with Bi concentration x and do not capture the maximum at $x \approx 0.63$. This is to be expected because structural disorder is not included in the calculations.

For small Bi contents x the spin splitting of the sp_z surface state of $\text{Bi}_x\text{Sb}_{1-x}/\text{Ag}(111)$ is comparable to the line width of the bands. This limits the accuracy of the values for the spin splitting obtained by conventional spin-integrated ARPES. To overcome this problem

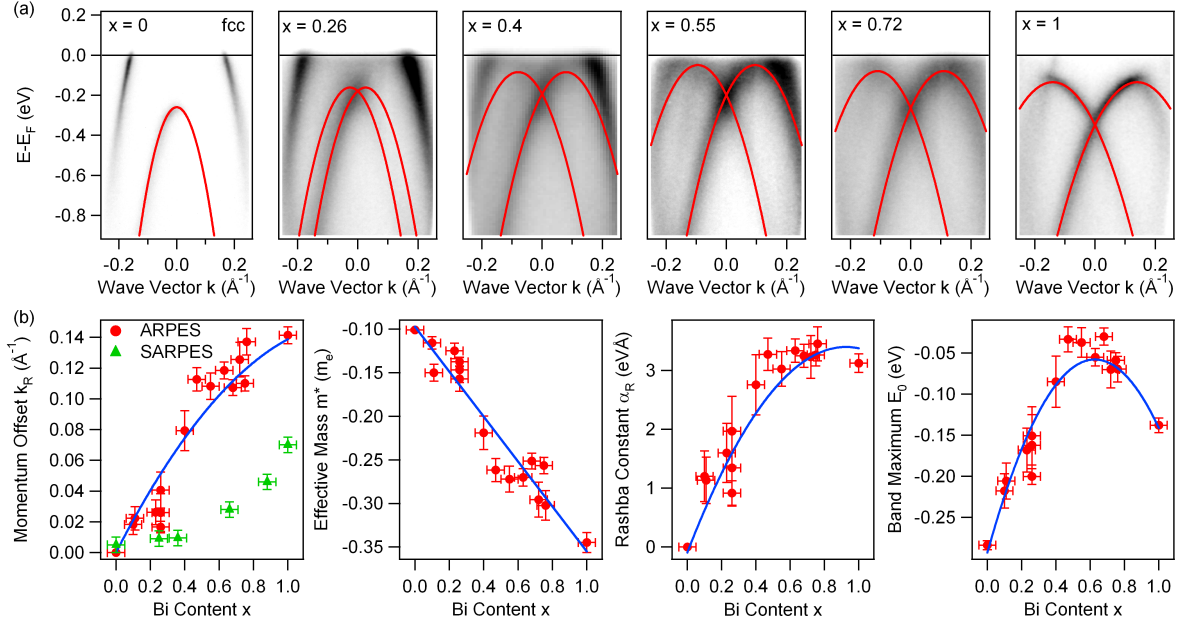


Figure 4.8: Experimental photoemission from $\text{Bi}_x\text{Sb}_{1-x}/\text{Ag}(111)$. The evolution of the sp_z surface state dispersion is shown as a function of Bi content x on a linear gray scale with black (white) corresponding to high (low) photocurrents (a). From parabolic fits to the data (red lines), the characteristic parameters of the Rashba model (momentum offset k_R , effective mass m^* , Rashba constant α_R , and band maximum E_0) have been determined (b). Red dots and green triangles were obtained by spin-integrated and spin-resolved ARPES, respectively. Blue lines are guides to the eye.

spin-resolved MDCs were recorded at an initial state energy of -0.6 eV as a function of Bi content x for the mixed $\text{Bi}_x\text{Sb}_{1-x}/\text{Ag}(111)$ surface alloy. The SARPES-derived momentum offset $\Delta k/2$ is included in Fig. 4.8 (b) (green triangles).

For a Bi content $x \gtrsim 0.3$ the sp_z -band is not parabolic any longer because it hybridizes with the upper p_{xy} -band. In this case, the values for k_R as determined by ARPES and $\Delta k/2$ as determined by SARPES deviate systematically. Nevertheless, the discrepancy for low values of x , where the dispersion is expected to be parabolic, is unexpectedly large. Although we cannot fully explain this discrepancy we want to point out that for small x a determination of k_R with conventional spin-integrated ARPES is difficult for several reasons. First, the size of the spin splitting is comparable to the line width of the bands, so that the two spin-polarized parabolas cannot be properly resolved. Second, the photoemission intensity of the sp_z -state for small x is suppressed for $k > 0$ at $h\nu = 21.2$ eV [see Fig. 4.8 (a)] due to photoemission matrix element effects, so that only part of the bands are available for the fitting procedure described above which limits the accuracy of the fits. However, the main trend — a continuous increase of the spin splitting with Bi content x — is clearly reproduced by the SARPES data.

The $(\sqrt{3} \times \sqrt{3})\text{R}30^\circ$ phase of $\text{Sb}/\text{Ag}(111)$ can be formed with either fcc or hcp toplayer

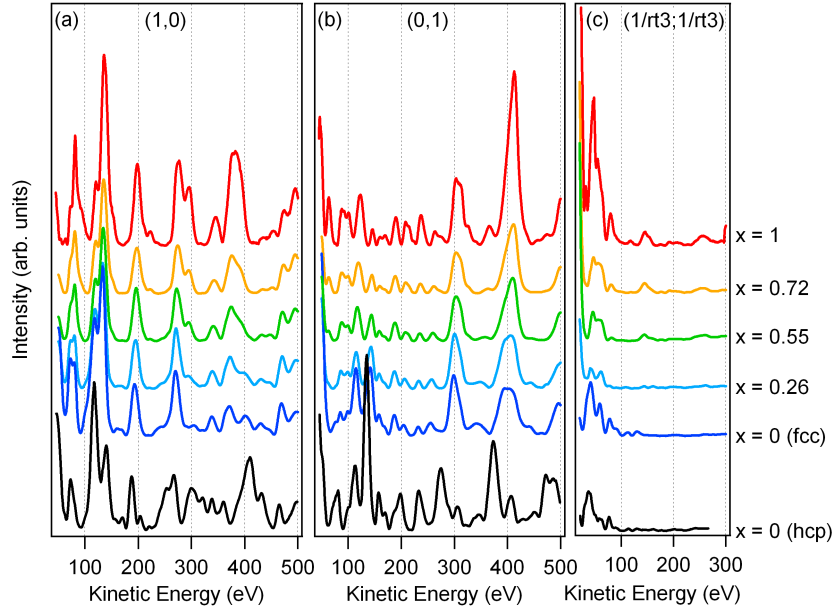


Figure 4.9: Low-energy electron diffraction from mixed $\text{Bi}_x\text{Sb}_{1-x}/\text{Ag}(111)$ surface alloys. The $I(V)$ spectra represent the integrated intensities of the (1,0) (a), (0,1) (b) and $(1/\sqrt{3}, 1/\sqrt{3})$ (c) spots versus electron energy. The spectra evolve continuously between $x = 0$ and $x = 1$. To exclude a possible hcp toplayer stacking, spectra for hcp stacked $\text{Sb}/\text{Ag}(111)$ are displayed for comparison (bottom).

stacking [144, 146, 159]. In experiment, the toplayer stacking can be controlled by tuning the energy of the deposited Sb ions during Sb deposition with an electron beam evaporator. The $\text{Sb}/\text{Ag}(111)$ surface alloys with fcc and hcp toplayer stacking, respectively, can easily be identified with the help of $I(V)$ -LEED measurements as we have shown in Ref. [146] and section 4.2.

In order to determine the toplayer stacking for the mixed $\text{Bi}_x\text{Sb}_{1-x}/\text{Ag}(111)$ surface alloy, we investigated the surface structure with $I(V)$ -LEED (Fig. 4.9). The $I(V)$ -LEED spectra were averaged over equivalent spots and smoothed (further details are given in [146]). They evolve continuously between the pure $\text{Bi}/\text{Ag}(111)$ surface alloy (red in Fig. 4.9) and the pure $\text{Sb}/\text{Ag}(111)$ surface alloy with fcc top layer stacking (blue). For comparison, the $I(V)$ spectra for the $\text{Sb}/\text{Ag}(111)$ surface alloy with hcp top layer stacking are shown in black. As these spectra clearly differ from those for the mixed $\text{Bi}_x\text{Sb}_{1-x}/\text{Ag}(111)$ surface alloy, we conclude that it forms with fcc top layer stacking even if Sb ions are deposited at sufficiently high energies to form an hcp stacked surface alloy.

4.3.2 Ternary surface alloy $\text{Bi}_x\text{Pb}_y\text{Sb}_{1-x-y}/\text{Ag}(111)$

As was shown before, both $\text{Bi}_x\text{Pb}_{1-x}/\text{Ag}(111)$ and $\text{Bi}_x\text{Sb}_{1-x}/\text{Ag}(111)$ can be formed and exhibit a well-defined band structure. While in the $\text{Bi}_x\text{Pb}_{1-x}/\text{Ag}(111)$ surface alloy both the spin splitting and the Fermi level change as a function of x , it is possible to change the spin splitting while leaving the Fermi level largely unaffected in the corresponding $\text{Bi}_x\text{Sb}_{1-x}/\text{Ag}(111)$ surface alloy. As transport properties are determined by the spin texture of the Fermi surface it is important to tune both the position of the Fermi level as well as the size of the spin splitting independently. This can be achieved in a ternary $\text{Bi}_x\text{Pb}_y\text{Sb}_{1-x-y}/\text{Ag}(111)$ surface alloy as follows. In order to increase k_R one has to add heavy elements with large outward relaxation (i.e. Bi, Pb). For a modification of E_F $\text{Bi}_x\text{Sb}_{1-x}$ should be mixed with Pb.

Figure 5 (a) in [165] shows the surface state band structure for a mixed ternary surface alloy with $(x, y, z = 1 - x - y) = (0.3, 0.35, 0.35)$. The line width is significantly increased as compared to those for the mixed binary surface alloys. The ARPES measurements in Fig. 5 (a) in [165] were done using the COPHEE spectrometer with a reduced angular resolution as compared to the setup used for the ARPES data in Fig. 4.8. An additional increase in line width is caused by the intermixing of three elements (instead of two) and by a — probably — not optimized sample preparation. Despite the large line width, the spin splitting ($\Delta k/2 = 0.019 \text{ \AA}^{-1}$) can still be clearly resolved with SARPES, as shown in Fig. 5 (b) in [165].

These results show that ternary alloys can be formed and exhibit a reasonably well defined band structure. They indicate the possibility to form ternary surface alloys with arbitrary compositions that allow us to tune the spin splitting as well as the Fermi energy independently and continuously over a broad range of values.

4.4 Conclusion

In this chapter we have discussed the origin and the manipulation of the spin splitting in surface alloys on $\text{Ag}(111)$.

First, we have studied the electronic structure of the $\text{Sb}/\text{Ag}(111)$ surface alloy and found obvious similarities with the bands of the iso-structural $\text{Bi}/\text{Ag}(111)$ and $\text{Pb}/\text{Ag}(111)$ surface alloys. The characteristic RB-type spin splitting found in $\text{Bi}/\text{Ag}(111)$ and $\text{Pb}/\text{Ag}(111)$, however, is considerably smaller in $\text{Sb}/\text{Ag}(111)$. The experimental data are well reproduced by relativistic first-principles calculations. A simple NFE model indicates that the additional in-plane inversion asymmetry, which plays a crucial role in the $\text{Bi}/\text{Ag}(111)$ surface alloy, is also present in $\text{Sb}/\text{Ag}(111)$. There, however, it is not efficient in producing a large RB-type spin splitting because of the weak atomic SOI in Sb. On the other hand, the difference in the observed spin splitting between $\text{Bi}/\text{Ag}(111)$ and $\text{Sb}/\text{Ag}(111)$ cannot be explained by the difference in atomic SOI alone, indicating that there are additional structural parameters that influence the size of the spin splitting.

In a second step, we have experimentally determined the outward relaxation of the

alloy atoms for the three different surface alloys Bi/Ag(111), Pb/Ag(111) and Sb/Ag(111) employing quantitative LEED measurements and calculations. The outward relaxation for Pb/Ag(111) is 0.46 \AA , which leads us to favor the scenario with the smaller spin splitting of $k_R = 0.04 \text{ \AA}^{-1}$ where the lower sp_z - and the upper p_{xy} -band avoid each other. The other scenario where a larger outward relaxation of 0.97 \AA leads to a band crossing between sp_z - and p_{xy} -band and a larger spin splitting of $k_R = 0.11 \text{ \AA}^{-1}$ has to be rejected on the basis of the experimentally determined outward relaxation. In addition, we found that the Sb/Ag(111) surface alloy can be grown reproducibly in fcc and hcp toplayer stacking. Furthermore, we have related the outward relaxation to the strongly enhanced spin splitting in the Ag(111) surface alloys comparing them also to surface alloys found on Cu(111). We find that the outward relaxation plays an extremely important role in the size of the spin splitting, because the ratio of the spin-orbit coupling strengths alone does not account for the ratio of the Rashba constants in two different surface alloys. Looking at each substrate individually a clear trend that a large outward relaxation leads to a large spin splitting is evident. Deviations from this trend can be observed when comparing the surface alloys on two different substrates, e. g. Bi/Ag(111) and Bi/Cu(111). This could be explained by the different orbital composition in the surface alloy band structure. The role of the substrate has not been completely solved yet. We conclude that the structure plays an important role for the spin splitting as it defines the potential landscape and has a profound influence on the orbital overlap and the band dispersion. Nevertheless, a straightforward, intuitive model for a better understanding of the RB-type spin splitting at surfaces would be desirable — if it exists.

Finally, we have shown that it is possible to form the mixed binary $\text{Bi}_x\text{Sb}_{1-x}/\text{Ag}(111)$ surface alloy despite the fcc/hcp top layer stacking of Sb/Ag(111). Furthermore, $I(V)$ -LEED experiments revealed that the mixed $\text{Bi}_x\text{Sb}_{1-x}/\text{Ag}(111)$ surface alloy always forms with fcc top layer stacking. ARPES and SARPES measurements show a continuous evolution of the band structure with Bi content x . The results on the mixed ternary surface alloy $\text{Bi}_{0.3}\text{Pb}_{0.35}\text{Sb}_{0.35}/\text{Ag}(111)$ show that ternary alloys can be formed and exhibit a reasonably well defined band structure. Our findings indicate the possibility to form ternary surface alloys with arbitrary compositions that allow us to tune the spin splitting as well as the Fermi energy independently and continuously over a broad range of values. Following this idea, the situation where the Fermi level lies in between the band maximum and the crossing point of the two parabolas is particularly interesting: in this regime the spins on the two circular Fermi surfaces rotate in the same direction and the density of states shows quasi one-dimensional behavior [4, 83]. In this case, the Rashba energy becomes the dominating energy scale and an increase of the transition temperature into a superconducting state is expected [90]. Furthermore, mixed surface alloys with a spatial variation of their chemical composition x create a gradient of the effective Rashba field that is a prerequisite for building a Stern-Gerlach spin filter [87].

Chapter 5

Silicon surface with giant spin splitting

Exploiting the electron spin for information processing is one of the leading goals in the rapidly growing field of spintronics. At its heart lies the RB type spin splitting, where the spin-orbit interaction lifts the spin degeneracy in a symmetry broken environment [1, 2]. The materials of choice are semiconductor heterostructures, albeit the size of the spin splitting is typically very small. A large spin splitting is desirable as it would, for example, decrease the precession time of the spin in a spin transistor [86] so that it is smaller than the spin relaxation time. Furthermore, a separation of the spin-split states beyond their lifetime broadening is an important criterion for distinguishing between the intrinsic and extrinsic spin Hall effect [88, 89, 166].

Recently, a giant spin splitting has been demonstrated for noble metal based surface alloys [3–5], where heavy elements with a strong atomic spin-orbit coupling are incorporated into the surface. These systems, however, are not suitable for the field of spintronics because of the presence of spin-degenerate bands at the Fermi level originating from the metallic substrate. One possible alternative is to grow thin films with spin-split bands onto a semiconducting substrate [112, 119, 120]. However, due to confinement effects a multitude of quantum well states arise, which potentially influence the transport properties of the system. It is, therefore, desirable to transfer the concept of the giant spin splitting directly onto a semiconductor surface.

5.1 Bi on Si(111)

In the following we will show that a monolayer of Bi trimers on a Si(111) surface forms a 2D electronic structure with a giant spin splitting much larger than what has been observed so far at the interfaces of semiconductor heterostructures. The effect can be traced to an inherent structural inversion asymmetry (RB model). While the structure of this system has been studied both theoretically as well as experimentally [122, 167, 168], the electronic structure, in particular a possible spin splitting of the electronic states, has remained a controversial issue [123, 124]. We demonstrate unequivocally that Bi induces a giant spin splitting at the silicon surface. Furthermore, the spin splitting is observed to be larger than

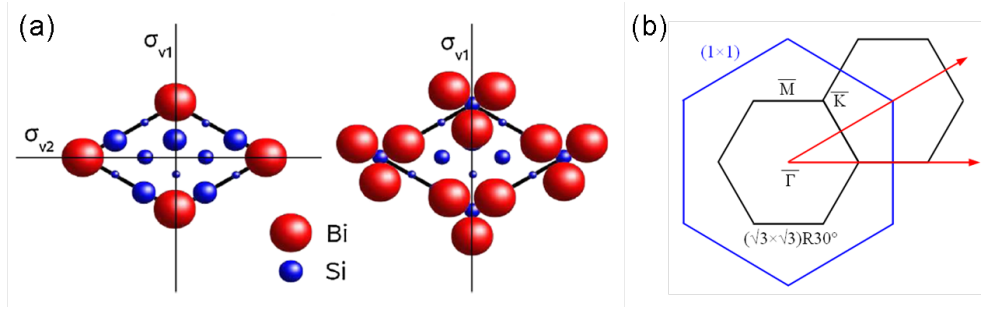


Figure 5.1: (a) Structural model of the two $(\sqrt{3} \times \sqrt{3})R30^\circ$ phases of Bi/Si(111): (left) monomer phase (right) trimer phase. The thin black lines indicate mirror planes of the Bi adlayer. The thicker black lines indicate the $(\sqrt{3} \times \sqrt{3})R30^\circ$ unit cell. The smaller the spheres, the further away they are from the surface. The corresponding 2D Brillouin zone is shown in (b).

the lifetime broadening, so that the Bi/Si(111) system is a prime candidate for spintronics applications or studying the intrinsic spin Hall effect. In addition, the silicon substrate allows for excellent compatibility with existing silicon-based semiconductor electronics. These results have been published in Ref. [169].

A single layer of Bi on Si(111) grows in a monomer as well as a trimer configuration, both of which show a $(\sqrt{3} \times \sqrt{3})R30^\circ$ reconstruction [122, 167, 168]. A structural model is shown in Fig. 5.1 (a) for the monomer phase (left) and the trimer phase (right). Both the monomers and the trimers are centered on top of second layer Si atoms (T_4 lattice sites). The Si substrate breaks the in-plane inversion symmetry for both the monomer and the trimer phase (similar to the Ag(111) substrate in the Ag(111) surface alloys). Considering only the isolated Bi adlayer, the trimer formation introduces a reduction of the symmetry: the mirror plane σ_{v2} is missing. The mirror plane σ_{v1} on the other hand holds for both the monomer and the trimer phase as well as for the combination of adlayer and Si substrate. From these simple symmetry considerations we conclude that the Bi trimer phase is the one with the lower symmetry, and, hence, should lead to the bigger spin splitting. Therefore, we only consider the trimer phase in the following.

As both the monomer phase at $1/3$ ML Bi coverage and the trimer phase at 1 ML Bi coverage show the same $(\sqrt{3} \times \sqrt{3})R30^\circ$ reconstruction we used $I(V)$ -LEED measurements to distinguish between the two phases. We measured the integrated intensity of the (10) and (01) spots as a function of electron energy and compared them to calculations done by Wan *et al.* [122]. The measured data was averaged over three equivalent spots and smoothed. The result is shown in Fig. 5.2. The agreement between measured and calculated spectra is quite convincing, allowing an unambiguous identification and preparation of the trimer phase.

The experimental band structure measured with ARPES along the two high symmetry directions of the surface Brillouin zone (SBZ) $\bar{\Gamma}\bar{M}$ and $\bar{\Gamma}\bar{K}\bar{M}$ is displayed in Fig. 5.3 (a) and (b), respectively. The intense feature near $\bar{\Gamma}$ at an energy of about -2.3 eV can be attributed to the silicon bulk. The other features (S1, S2, S3) in Fig. 5.3 (a) originate from

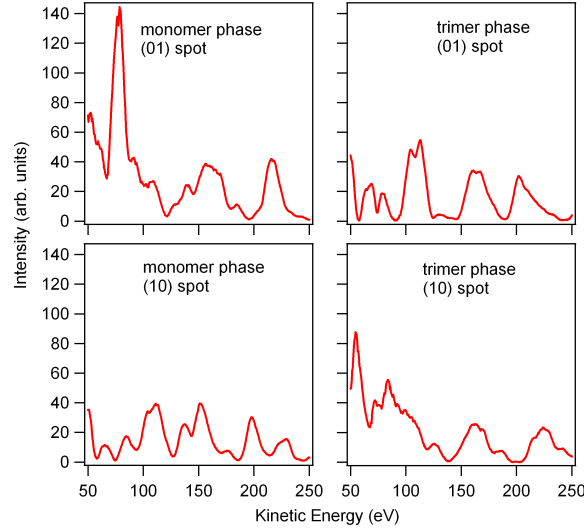


Figure 5.2: The bismuth coverage was determined via $I(V)$ -LEED measurements. The figures show the integrated intensity as a function of electron energy for the (10) and (01) spots of the monomer and trimer phase, respectively.

the 2D electronic structure of the surface. S1 is most intense at the \bar{M} -point at an initial state energy of about -1.3 eV. This band splits in two components when moving away from the high symmetry point \bar{M} , which is a strong indication of a RB-type spin splitting. S2 is located at about -2.3 eV at the second $\bar{\Gamma}$ -point and disperses upwards towards the \bar{M} -points. The third state S3 shows the highest intensity at the second \bar{M} -point at an energy of about -2.5 eV. This band moves downwards in energy towards the second $\bar{\Gamma}$ -point. The bandwidth of S3 is smaller than the one for S2. These three 2D states are also visible along the $\bar{\Gamma}\bar{K}\bar{M}$ -direction as shown in Fig. 5.3 (b). S1 appears as a parabolic band with negative effective mass with a band maximum located at about -1.3 eV at the \bar{M} -point. Along the $\bar{\Gamma}\bar{K}\bar{M}$ direction no splitting of this band has been observed. S2 is located around -1.8 eV at \bar{M} , but only with a very weak intensity. The most intense feature along the $\bar{\Gamma}\bar{K}\bar{M}$ -direction is the S3 2D state with a band minimum at about -2.5 eV at the \bar{M} -point and an upwards dispersion towards the neighboring \bar{K} -points.

A possible spin splitting in the Bi/Si(111) system is an unresolved issue in the literature. While Kinoshita *et al.* [123] consider a splitting in the three 2D states related to a strong spin-orbit interaction of the Bi atoms, it has been dismissed by Kim *et al.* [124]. In the following, we will show from the experimental data as well as spin-resolved band structure calculations that the band structure shows a giant spin splitting of the electronic states due to the RB effect.

A close up of the band structure near the \bar{M} -point is shown in Fig. 5.4. The bands along $\bar{\Gamma}\bar{M}$ [Fig. 5.4 (a)] near -1.2 eV clearly show the characteristic dispersion of a RB type spin splitting with the band crossing at the \bar{M} -point and the shift of the maxima away from it. From the data we extract the momentum offset $k_R = 0.126 \text{ \AA}^{-1}$, an effective

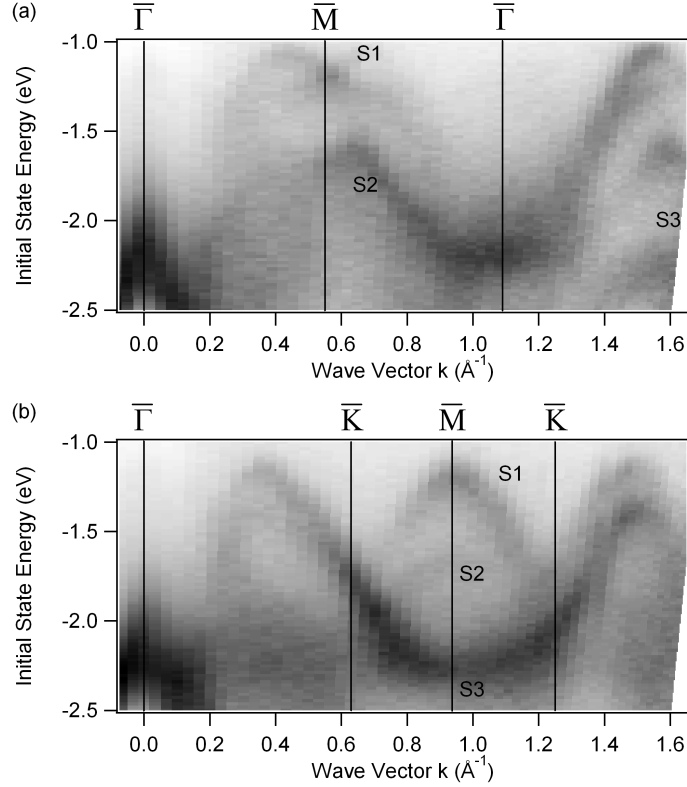


Figure 5.3: The two panels show angle-resolved ultra violet photoemission spectroscopy data of the trimer phase of bismuth on Si(111) along the two high symmetry directions $\bar{\Gamma}\bar{M}$ (a) and $\bar{\Gamma}\bar{K}\bar{M}$ (b). The photoemission intensity is on a linear scale with black and white corresponding to highest and lowest intensity, respectively. The energy scale is set to zero at the Fermi level. A splitting of the two-dimensional state into two bands around the \bar{M} point along the $\bar{\Gamma}\bar{M}$ -direction at an initial state energy of about -1.3 eV is clearly visible in panel (a). We attribute this splitting to the Rashba-Bychkov effect with a momentum offset $k_R = 0.126 \text{ \AA}^{-1}$ and a Rashba energy $E_R = 140$ meV.

mass of $m^* = 0.7 m_e$ as well as the Rashba energy $E_R = 140$ meV. From these values we can calculate the Rashba parameter $\alpha_R = 1.37 \text{ eV\AA}$. The spin splitting is well resolved in the data. The average line width for the spin-split states at the band maximum ($k_x = -0.126 \text{ \AA}^{-1}$) is 195 meV, which accounts for intrinsic lifetime as well as interactions and scattering. The separation of the states is about 220 meV.

The spin splitting at the \bar{M} -point in Fig. 5.4 (a) is strongest along the $\bar{\Gamma}\bar{M}$ -direction. Along the $\bar{K}\bar{M}\bar{K}$ -direction in Fig. 5.4 (b) the spin splitting at the \bar{M} -point is much weaker and cannot be resolved in the experiment. This peculiar band topology can be related to the symmetry properties of the surface structure [see Fig. 5.1 (a)]. Despite the symmetry breaking of the Bi trimers, the mirror symmetry σ_{v1} holds so that for the dispersion along the $\bar{K}\bar{M}\bar{K}$ -direction the spin splitting is greatly reduced, i. e. it cannot be observed in the data. Furthermore, the \bar{M} -point is located on the border of the first SBZ and has a

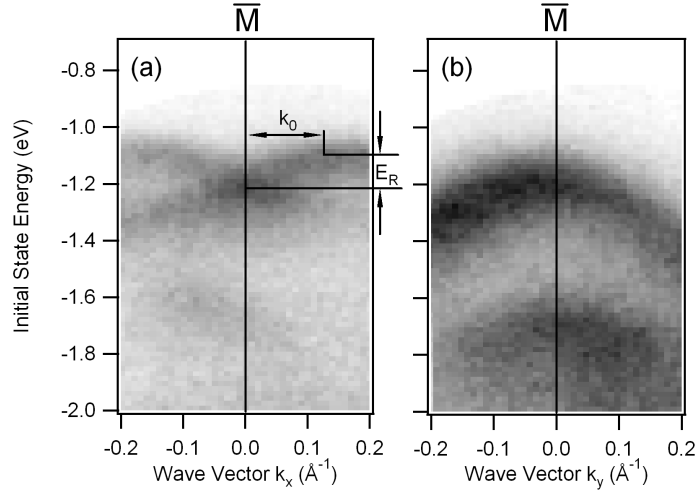


Figure 5.4: Experimental band structure of Bi/Si(111) near the \bar{M} -point. The measurements along $\bar{\Gamma}\bar{M}\bar{\Gamma}$ (a) and $\bar{K}\bar{M}\bar{K}$ (b) show the anisotropic topology of the spin-split bands.

reduced symmetry as compared to the $\bar{\Gamma}$ -point so that an isotropic dispersion around the \bar{M} -point cannot be expected.

To support our interpretation of the observed spin splitting, we conducted spin-resolved first principles band structure calculations. Using the VASP we find that the Bi trimers (milkstool structure) are relaxed outward by 13% from the ideal positions (100% corresponds to the Si bulk interlayer distances, lattice constant (5.403 Å)). The subsurface relaxations are small (<0.5%) and neglected in the Korringa-Kohn-Rostoker (KKR) calculations. The in-plane displacement of the Bi trimer atoms δ is 0.3 with $\delta = 0$ indicating Bi atoms on top of the first layer Si atoms and $\delta = 1$ coinciding Bi-trimer atoms on T_4 sites. The spectral density $n_{\pm}(E, \vec{k}_{\parallel})$ is obtained from the imaginary part of the site-dependent Green function. Resolved with respect to spin orientation (index \pm) and angular momentum, it allows a detailed analysis of the electronic structure. The results of the band structure calculations $n_{+}(E, \vec{k}_{\parallel}) - n_{-}(E, \vec{k}_{\parallel})$ are shown in Fig. 5.5 for the $\bar{\Gamma}\bar{M}$ -direction in (a) and for the $\bar{\Gamma}\bar{K}\bar{M}$ -direction in (b). Blue and red colors correspond to opposite spin-polarizations. The calculations reproduce all the main features of the measured band structure. In particular, the splitting of the S1 band around the \bar{M} -point along the $\bar{\Gamma}\bar{M}$ -direction is well documented. As can be seen in Fig. 5.5 the two branches of the split S1 band clearly show opposite spin-polarization, i. e. a giant spin splitting in the electronic structure of Bi/Si(111).

The spin splitting is strongly anisotropic around \bar{M} . The peculiar band topology, which was observed in the experiment is clearly reproduced in the calculations. This can again be attributed to the lower symmetry of wave vectors \vec{k}_{\parallel} within ($\bar{\Gamma}\bar{K}\bar{M}$) or perpendicular ($\bar{\Gamma}\bar{M}\bar{\Gamma}$) to a mirror plane of the system. It is conceived that this feature results from the ‘trimerization’ of the three Bi sites in the 2D unit cell; calculations with a reduced δ (i. e. larger distance between Bi trimer atoms) indicate an even smaller splitting along $\bar{\Gamma}\bar{K}\bar{M}$.

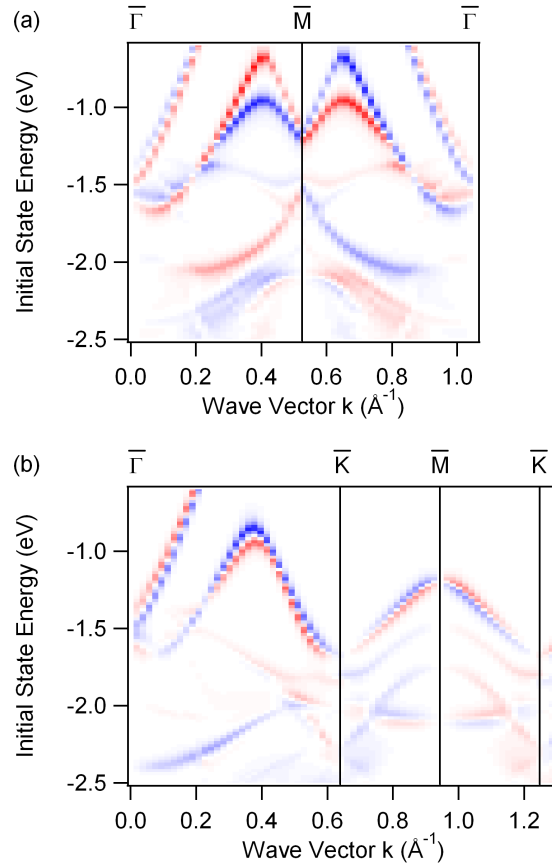


Figure 5.5: Theoretical band structure calculations for the trimer phase of bismuth on silicon(111). Panel (a) and (b) show the calculated dispersion along $\bar{\Gamma}\bar{M}$ and $\bar{\Gamma}\bar{K}\bar{M}$, respectively. Blue and red correspond two opposite spin-polarizations. The calculated spectra reproduce the main features of the measured band structure, especially the spin splitting of the bands around the \bar{M} -point along $\bar{\Gamma}\bar{M}$.

Furthermore, the calculations show that about 83% of the spin-split states at the \bar{M} -point are localized in the Bi adlayer and about 16% in the first Si layer. One can thus speculate that the spin splitting has to be attributed to the presence of the heavy Bi atoms and that the spin splitting is further enhanced by the loss of in-plane inversion symmetry (σ_{v2} in Fig. 5.1 (a) is missing).

The giant spin splitting in the Bi/Si(111) trimer system has a similar origin as in the Bi/Ag(111) surface alloy: An additional inversion symmetry breaking in the plane of the surface leads to a strong enhancement of the spin splitting. In both systems the threefold symmetry of the underlying substrate breaks the in-plane inversion symmetry. However, considering only the topmost layer, the trimer formation in Bi/Si(111) also leads to a breaking of the in-plane inversion symmetry (see Fig. 5.1), which is not the case for the Bi/Ag(111) surface alloy. This inversion asymmetry of the in-plane potential for Bi trimers on Si(111) is illustrated in Fig. 5.6.

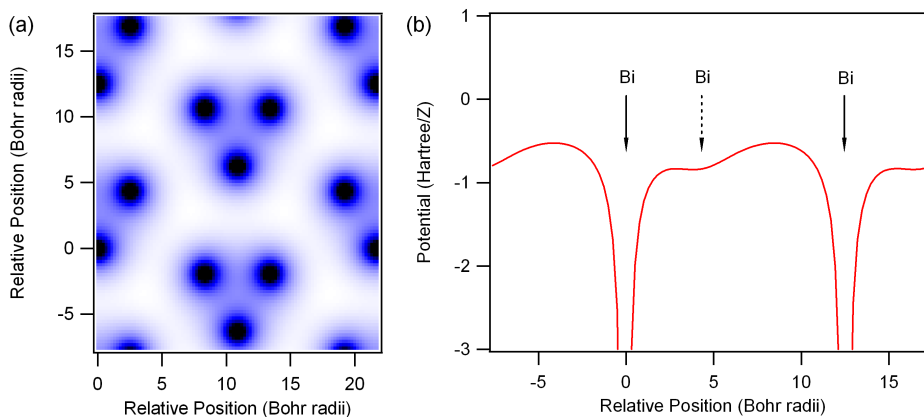


Figure 5.6: Coulomb potential landscape of the Bi trimer atoms (schematic). (a) Two-dimensional plot of the potential produced by point charges at the positions of the Bi atoms. (b) Potential profile along the vertical symmetry line. The breaking of the inversion symmetry is clearly visible. The positions of the Bi atoms are marked by arrows, with the dashed arrows indicating Bi atoms displaced away from the symmetry line.

Comparing the spin splitting of the Bi/Si(111) electronic structure to semiconductor heterostructures, we find that in the latter the spin splitting is substantially smaller. For example, for an inverted InGaAs/InAlAs heterostructure a Rashba constant of $\alpha_R = 0.07 \text{ eV\AA}$ has been measured [170]. With an effective mass of $m^* = 0.05 m_e$, a Rashba energy of $E_R = 16 \mu\text{eV}$ can be calculated. For HgTe quantum wells a Rashba constant $\alpha_R = 0.45 \text{ eV\AA}$ has been found [171]. However, here the spin splitting has been identified to be proportional to k_{\parallel}^3 instead of a linear dependence [172]. For the Bi/Si(111) system, the Rashba energy $E_R = 140 \text{ meV}$ as well as the Rashba parameter $\alpha_R = 1.37 \text{ eV\AA}$ are much bigger. From the momentum offset $k_R = 0.126 \text{ \AA}^{-1}$ we can calculate that a phase shift of the spin precession angle $\Delta\theta = \pi$ can be obtained after a length $L = \Delta\theta/2k_R$ of only 1.3 nm. In the InGaAs/InAlAs heterostructure a length of 400 nm has been estimated. While these figures show the excellent potential of the Bi/Si(111) system, additional measurements giving insight into the transport properties, such as Shubnikov-de Haas oscillations, are necessary to further elaborate the suitability of this system for spintronics applications.

5.2 Conclusion

We have shown that the trimer phase of Bi on Si(111) shows a giant spin splitting. The experimental results reveal the characteristic band dispersion of a RB-type spin splitting with a peculiar band topology at the \bar{M} point. They are confirmed by first principles band structure calculations. The splitting is caused by the spin-orbit interaction induced RB effect in combination with a strong contribution from the reduced in-plane symmetry of the trimer structure and the substrate. Furthermore, this spin splitting is of the same order of magnitude as the one reported for Bi/Ag(111) and orders of magnitude larger than

a typical spin splitting reported for semiconductor heterostructures. In this way, we have transferred the concept of giant spin splitting onto a semiconducting substrate. This gives excellent perspectives for the use of this concept in the field of spintronics. In particular, the silicon substrate makes this system compatible with existing semiconductor technology. On the fundamental side such systems are interesting for, e. g., the spin Hall effect. Since the energy separation of the spin-split states (220 meV) is larger than the lifetime broadening (195 meV), it may be easier to distinguish the extrinsic and intrinsic spin Hall effects.

Recently, our findings were confirmed and complemented. The authors of Ref. [173] observe a similar spin splitting ($E_R = 120$ meV and $k_R = 0.105 \text{ \AA}^{-1}$) of the S_1 surface state along the $\overline{\Gamma\text{M}}$ -direction. In addition, they were able to resolve a spin splitting also for the other two surface states S2 ($E_R = 60$ meV and $k_R = 0.07 \text{ \AA}^{-1}$) and S3 ($E_R = 60$ meV and $k_R = 0.08 \text{ \AA}^{-1}$). Reconsidering our data in Fig. 5.3 (a) the peculiar shape of the S2 band between $\overline{\Gamma}$ and $\overline{\text{M}}$ is a strong indication for the RB-type spin splitting reported in Ref. [173]. Furthermore, Ref. [173] reports a spin splitting for both S1 and S3 along the $\overline{\Gamma\text{KM}}$ -direction. The splitting of the S1 band between $\overline{\text{K}}$ and $\overline{\Gamma}$ can also be seen in our data in Fig. 5.3 (b) around $k = 1.5 \text{ \AA}^{-1}$.

Constant energy contours in Ref. [173] reveal an isotropic spin splitting with standard RB-type spin structure of S3 around the $\overline{\Gamma}$ point. S1 shows a similar vortical spin structure around the $\overline{\text{K}}$ point. There, however, the constant energy contour has no spherical shape which is attributed to the strong crystal field at the boundary of the surface Brillouin zone. The spin structure of the S1 band around the $\overline{\text{M}}$ point was found to be non-vortical. These findings were explained using symmetry arguments: The threefold symmetry of the trimer phase and the presence of mirror planes σ_{v1} along the $\{11\overline{2}\}$ direction (which corresponds to $\overline{\Gamma\text{K}}$) lead to a C_{3v} symmetry for the $\overline{\Gamma}$ and $\overline{\text{K}}$ points, and a C_{1h} symmetry for the $\overline{\text{M}}$ point.

To conclude, Ref. [173] confirms our finding of a large RB-type spin splitting of the surface state band structure for a monolayer of Bi trimers on Si(111). In agreement with our interpretation the origin of the spin splitting was traced back to the loss of the σ_{v2} mirror plane due to the threefold rotational symmetry of the structure. Along the symmetry line $\overline{\Gamma\text{K}}$ the spin splitting is much smaller than perpendicular to that direction ($\overline{\Gamma\text{M}}$).

Chapter 6

Discussion: origin of the giant spin splitting

In section 2.2.4 we briefly discussed the different parameters that were used to explain the origin of the observed RB-type spin splitting in different systems. Although there is general agreement that the two key ingredients for a sizable spin splitting are a structural inversion asymmetry combined with the presence of heavy atoms many details still remain controversial. Before we turn to a detailed discussion about the origin of the RB-type spin splitting at surfaces we will discuss the fundamental principles by a more detailed look at the Au(111) surface state which can be regarded as a prototype for these systems. Afterwards, we will summarize previous findings on different 2D electron systems localized at a crystal surface and try to develop a more complete picture that is able to explain the spin splitting in an arbitrary system.

6.1 The Au(111) surface state

The largest contribution to the spin-orbit coupling comes from regions where the crystal potential changes rapidly, i.e. close to the nucleus of heavy atoms such as Au. The surface potential barrier can be regarded as a structural asymmetry which additionally results in a SOI-mediated spin splitting. However, the strength of the surface potential gradient is orders of magnitude too small to account for the size of experimentally observed spin splittings [83, 85, 174].

The RB-type spin splitting of the Au(111) sp_z surface state was first resolved by La Shell *et al.* in 1996 using ARPES [93]. Recent high resolution ARPES measurements [94] confirmed that the two parabolas of the Au(111) surface state are shifted by $k_R = \pm 0.013 \text{ \AA}^{-1}$ away from the $\bar{\Gamma}$ point. The electron spin polarization of the L-gap surface states on Au(111) can be nicely explained using the original RB model [151]. The spin polarization lies mainly in the plane of the 2D electron gas and is perpendicular to k_{\parallel} , with spin \uparrow (spin \downarrow) rotating clockwise (anticlockwise) around the z axis. As the inversion asymmetry is mainly along the z -direction the out-of-plane polarization P_z is small. At

$k_{\parallel} = 0$, the states are degenerate and the electron spin polarization becomes zero.

Although there are striking similarities between the electronic states in a 2DEG with RB-type spin-orbit interaction and the L-gap surface state on Au(111), the threefold rotational symmetry of the fcc lattice (ABC stacking sequence) allows in principle for a non-zero P_z component as well as for a deviation from the circular constant energy contours that is missing in a 2DEG [147,151]. In the framework of the RB model the presence of a non-zero P_z requires non-vanishing in-plane components of the potential gradient [see equation 2.5]. Thus, P_z is brought about by the in-plane asymmetry of the surface potential, i.e. the surface corrugation.

The effect of surface corrugation on the spin polarization of the L-gap surface states was investigated in Ref. [147]. For a corrugated muffin-tin barrier a small P_z of 1.5% has been found. For a smooth uncorrugated barrier shape P_z is slightly reduced to 1%. This humble change has been attributed to the considerable extension of the surface state wave function within the ten outermost surface layers that smears out the effect of the surface corrugation. In Ref. [175] the influence of the surface corrugation in the form of step lattices was studied using spin-resolved ARPES on vicinal Au(111) surfaces. For a terrace width $> 20\text{\AA}$ the electrons are confined within each (111) terrace. For step separations $< 20\text{\AA}$ the wave functions are delocalized over several steps and become sensitive to the corrugated lattice potential of the steps. In this case, the spin splitting of the surface state increases considerably to $k_R = 0.021\text{\AA}^{-1}$.

Bihlmayer *et al.* [98] have taken a more detailed look at the microscopic origin of the spin splitting of the Au(111) surface state. They found that the Au(111) surface state extends considerably into the bulk, and that more than 40% of the total spin splitting actually comes from the subsurface layers. Furthermore, more than 90% of the contribution to the splitting comes from a region defined by a sphere with a radius of 0.25 atomic units around the nucleus. Therefore, the size of the spin splitting is not determined by the potential gradient at the surface but rather by the resulting asymmetric charge distribution around the atomic cores. Close to the nucleus the wave functions are well expanded in spherical harmonics. This expansion reveals that the surface state wave function of the Au(111) surface state contains contributions from s -, p - and d -orbitals. The authors concluded that the ratio of l - to $(l \pm 1)$ -character of the surface state wave function is a measure of the effective potential gradient at the surface and hence also for the spin splitting. The authors concluded that there is no spin splitting for a surface state of pure l -character.

The discussion of the Au(111) surface state has revealed several important contributions to the RB-type spin splitting at surfaces: (a) a structural inversion asymmetry, (b) the atomic SOI, (c) the corrugation of the surface and (d) the mixing of l - and $(l \pm 1)$ -orbitals in the surface state wave function. In the following we will discuss these contributions in more detail.

6.2 The atomic spin-orbit coupling

From Refs. [83, 85] we know that the magnitude of the symmetry-breaking electric field alone is orders of magnitude too small to account for experimentally observed spin splittings. This problem can be solved by considering a more elaborate model that includes the atomic contribution to the SOI [85]. Petersen and Hedegård [85] considered a simple tight binding model that allowed them to derive an analytic expression for the Rashba coefficient $\alpha_R \propto \alpha\gamma$, where α is the atomic spin-orbit parameter and γ accounts for the effect of the surface potential gradient. The importance of the atomic spin-orbit parameter was confirmed by Ref. [174], where the RB-type spin splitting of the Au(111) surface state is separated into a contribution from the potential gradient of the nucleus and a contribution from the surface potential gradient. The authors concluded that the latter is negligible, and that the RB-type spin splitting mainly comes from a small sphere of radius $R = a_B/Z$ around the nucleus, where a_B is Bohr's radius and Z is the atomic number. Ref. [98] confirmed that more than 90% of the contribution to the splitting of the Au(111) surface state comes from a region defined by a sphere of 0.25 atomic units around the nucleus.

In order to get a first clue about the order of magnitude of the spin splitting that can be expected for the surface state on a certain clean metal surface the spin-orbit splitting of the corresponding atom is usually considered. Table 6.1 summarizes the values for some typical metals. The difference in the atomic spin-orbit parameter can explain qualitatively why the spin splitting of the surface state on clean W(110) is much larger than on clean Mo(110) [97]. For the same reason the spin splitting for the surface states on clean noble metal surfaces is expected to decrease from Au(111) via Ag(111) to Cu(111) [94, 125]. The spin splitting obtained for different Bi surfaces [Bi(111), Bi(110) and Bi(100)] is a few times bigger than for Au(111) [95], and the spin splitting of the surface states on Sb(111) is smaller than on Bi(111) [96] in agreement with the corresponding atomic spin-orbit parameters. A similar reasoning was also applied to explain the size of the spin splitting in thin Ag films on Au(111) or in mixed $\text{Ag}_x\text{Au}_{1-x}$ alloys. In both cases the Rashba constant is proportional to the amount of heavy gold atoms probed by the Shockley state wave function [102, 104].

However, the Rashba constant α_R is influenced by many different parameters and values for the size of the spin splitting that are deduced from the atomic spin-orbit parameter alone can only serve as rough estimates. The limitations of such estimates become obvious when comparing, e.g., the spin splitting of clean Bi surfaces and the (Bi,Pb,Sb)/Ag(111) surface alloys where the difference in atomic SOI alone cannot account for the difference in Rashba constant (see sections 4.1 and 4.2).

6.3 Broken space inversion symmetry

As mentioned in section 2.2.2 spin degeneracy is the consequence of combined time-reversal and space inversion symmetry. The only possibility to lift the spin degeneracy in a non-magnetic system without applying external magnetic fields is to break space inversion

	atomic number Z	atomic orbital	spin-orbit splitting (eV)	Ref.
C	6	$2p$	0.008	[176]
Cu	29	$3p$	0.03	[154]
Mo	42	$4d$	0.12	[177]
Ag	47	$5p$	0.11	[154]
Sb	51	$5p$	0.40	[148]
W	74	$5d$	0.45	[177]
Au	79	$6p$	0.47	[154]
Pb	82	$6p$	0.91	[148]
Bi	83	$6p$	1.25	[148]

Table 6.1: atomic spin-orbit splitting for some metals

symmetry. In the original RB model this is achieved by an external electric field along the direction perpendicular to the confinement plane of the 2DEG [1, 2]. In real systems inversion symmetry breaking is caused by the asymmetric confinement potential for the 2D electron gas in a semiconductor quantum well or heterostructure, or by the presence of the surface like in the case of the Au(111) surface state. Despite the considerable differences between these systems they have one thing in common: there is no spin splitting as long as space inversion symmetry holds.

6.3.1 Surface potential gradient and electron confinement

Although the contribution of the surface potential gradient to the size of the spin splitting is negligibly small [85, 174] its presence is a necessary condition to lift the spin degeneracy of the 2D band structure. In the following we will discuss a few examples that illustrate the influence of the potential gradient at the crystal surface on the size of the spin splitting.

In Ref. [97] it was shown that the spin splitting of the W(110) as well as the Mo(110) surface states can be increased by a factor of two to three upon Lithium adsorption. The authors argued that the adsorption of Li atoms changes both the magnitude of the potential gradient (which is similar to the work function change) as well as the localization of the surface state wave function. Upon Li adsorption the surface state wave function becomes more confined to the crystal surface and thereby more exposed to the potential gradient at the surface.

A similar experiment was done in Refs. [99, 100], where the spin splitting of the Au(111) surface state was increased by the adsorption of rare gases (Ar, Kr, Xe). Due to the repulsive interaction between the sp_z surface state and the nearly unperturbed atomic wave functions of the rare gas atoms, the charge from the evanescent tail of the surface state that penetrates into the vacuum region is driven back into the substrate. The sp_z surface state is pushed towards the atomic cores of the substrate atoms and therefore experiences a stronger potential gradient that — on its part — increases the spin splitting. The work function change (i.e. the change of the surface potential) on the order of 0.5 eV

was assumed to play a minor role in this case.

Another instructive example is the RB-type spin splitting of the Gd(0001) and the $p(1 \times 1)\text{O}/\text{Gd}(0001)$ surface states [101]. The Rashba energy is enhanced by a factor of three upon oxide formation and the Rashba constant changes its sign. The Gd(0001) surface state is almost completely localized within the metal surface layer. Upon oxide formation the weight of the surface state shifts to the region of the O/Gd interface. Due to charge transfer to the electronegative O atom steep charge gradients arise, and the RB-type spin splitting increases considerably. The charge gradient for the clean Gd(0001) surface is small and positive, the charge gradient for the O/Gd interface is much stronger and negative which explains both the size as well as the sign change of the Rashba constant.

The surface states in Lu(0001) show a spin splitting around the $\bar{\Gamma}$ point that is of similar size like for the Au(111) surface state. An external electric field of $-0.46 \text{ V}/\text{\AA}$ pushes the charge density towards the vacuum region which results in a decrease of the spin splitting by about 10% [98].

For a Bi monolayer on Cu(111) three spin-polarized bands have been observed [178]. For this system the magnitude of the spin splitting was found to increase with decreasing binding energy of the states. The largest RB-type spin splitting with $\alpha_R = 2.48 \text{ eV}\text{\AA}$ has been measured for an unoccupied 2D state at an initial state energy of 2.76 eV. With increasing energy the weight of the 2D states shifts towards the vacuum region. The state with the lowest binding energy is completely localized within the Bi layer and therefore insensitive to both the Bi/vacuum as well as the Cu/Bi interface. Hence, the observed spin splitting is small. The two higher lying unoccupied states, however, are delocalized towards the vacuum region and thus are exposed to the potential gradient at the Bi/vacuum interface which increases the spin splitting. The authors concluded that the origin of the large Rashba constant in this system lies in the out-of-plane gradient of the potential $\partial V(\vec{r})/\partial z$.

The above mentioned examples show that upon adatom adsorption or oxidation of the surface the localization of the surface state shifts to regions where the potential gradient is larger (smaller) which results in an increase (decrease) of the spin splitting. The change in localization of the electronic states can be attributed to the change of the surface potential gradient. The size of the spin splitting then depends on the magnitude of the nuclear potential gradient at the position where the electronic states are localized. If the 2D electronic states are confined to the region where the potential gradient is large (i.e. close to the atomic nucleus of heavy atoms) a large spin splitting is expected. The contribution of the surface potential gradient is simply that it creates an appropriate asymmetric confinement potential that allows for the lifting of the spin degeneracy of the corresponding 2D states. The magnitude of the spin splitting is then determined by the nuclear potential gradients.

6.3.2 In-plane inversion asymmetry

The original RB model, where an electric field perpendicular to the confinement plane of the 2D free electron gas breaks the inversion symmetry, predicts parabolic dispersions, circular

constant energy contours and complete in-plane spin polarization. An additional inversion asymmetry in the plane of the 2DEG tilts the spin quantization axis given by the cross product between \vec{k}_{\parallel} and the structural inversion asymmetry along \vec{e} (see equation 2.5) and allows for a non-zero out-of-plane spin component. Furthermore, the spin splitting becomes anisotropic and the constant energy contours deviate from a circular shape. Such an in-plane inversion asymmetry shows up, e.g., at fcc(111) surfaces due to their ABC stacking sequence, for the ordered surface alloys (Bi,Pb,Sb)/Ag(111) and also for Bi trimers on Si(111).

The giant spin splitting of the 2D states in the Bi/Ag(111) surface alloy cannot be explained by a strong atomic SOI alone [5]. The unexpectedly large spin splitting is accompanied by a deviation from a parabolic dispersion, a constant energy contour with sixfold rotational symmetry, and a considerable out-of-plane spin polarization [5, 110, 111]. These observations are a strong indication for the presence of an additional in-plane inversion asymmetry. This in-plane inversion asymmetry is caused by the threefold rotational symmetry of the Ag(111) substrate and is further enhanced by the considerable outward relaxation of the Bi atoms [5, 111].

Ref. [111] investigated the effects of an additional in-plane inversion asymmetry on the dispersion and the spin polarization of a nearly free electron gas. The in-plane inversion asymmetry was mimicked by an asymmetric potential $V(\rho) \neq V(-\rho)$, where $\rho = (x, y)$. Due to the in-plane inversion asymmetry, the band structure for \vec{k}_{\parallel} within a mirror plane of the system differs significantly from that for \vec{k}_{\parallel} perpendicular to a mirror plane. As a result, the constant energy contours deviate from a circular shape. Furthermore, the additional in-plane inversion asymmetry also affects the size of the spin splitting. For an in-plane inversion asymmetry only and \vec{k}_{\parallel} perpendicular to a mirror plane, the spin splitting increases with increasing $|\vec{k}_{\parallel}|$. The size of the spin splitting, however, is much smaller than that induced by the perpendicular inversion asymmetry alone. If \vec{k}_{\parallel} lies within a mirror plane of the system, there is no splitting at all because space inversion symmetry holds in this case. It is the combination of both in-plane and out-of-plane inversion asymmetry that leads to a strong enhancement of the spin splitting.

The effect that the spin splitting is reduced when \vec{k}_{\parallel} lies within a mirror plane of the system is also observed for a monolayer of Bi trimers on Si(111) (see section 5.1 and Refs. [169, 173]). There, the spin splitting of the 2D states is much larger along $\overline{\Gamma\text{M}\Gamma}$ than along $\overline{\Gamma\text{K}\text{M}}$ which lies within a mirror plane of the system.

6.4 Corrugation

As previously mentioned, the contribution from an in-plane inversion asymmetry is intimately linked to the surface corrugation or outward relaxation of the alloy atoms in the (Bi,Pb,Sb)/Ag(111) surface alloys. The microscopic origin of the enhanced splitting in different surface alloys was investigated in Ref. [109]. Depending on the outward relaxation Δz of the alloy atoms the sp_z -state and the lower p_{xy} $m_j = 1/2$ state hybridize and a

band gap opens at the band crossing. Upon decreasing the outward relaxation this hybridization becomes stronger and the Rashba splitting of the sp_z surface state decreases. This points towards an important influence of the outward relaxation on the 2D band structure in surface alloys. The authors of Ref. [109] have demonstrated that the spin splitting for a hypothetical flat Bi/Ag(111) surface alloy reduces to $k_R = 0.05\text{\AA}^{-1}$. In this case the occupied surface state is of sp_z -type with an $s : p_z$ ratio of 4:1. A small outward relaxation of the Bi atoms of 0.1\AA changes the $s : p_z$ ratio to 2:1 and increases the splitting to about 0.07\AA^{-1} . Further relaxation of 0.87\AA adds also some p_{xy} -character at the expense of s -character and increases the splitting to 0.13\AA^{-1} which is in good agreement with experiment [5].

The increase of the spin splitting upon increasing p_{xy} -character of the surface state can be attributed again to an additional in-plane inversion asymmetry. p_z orbitals point along the normal of the confinement plane, whereas p_{xy} -orbitals lie in the plane of the 2D electron system and are therefore much more sensitive to the in-plane inversion asymmetry [111]. This is in agreement with the tight binding model from [85], where the Rashba constant was found to be proportional to the asymmetry parameter $\gamma = \langle p_z(\vec{R}) | V | p_{xy}(\vec{R} + \vec{r}) \rangle$. This asymmetry parameter is given by the overlap between p_z and p_{xy} -orbitals on adjacent atoms induced by the potential V . For $\gamma = 0$ the overlap is zero, inversion symmetry is restored and there is no spin splitting.

Ref. [105] gives another indication that the giant spin splitting in the Bi/Ag(111) surface alloy is enhanced by the outward relaxation of the Bi atoms. Upon Xe adsorption onto the Bi/Ag(111) surface alloy small energy gaps appeared at the crossing of bands with sp_z - and p_{xy} -character, but the Xe adsorption did not modify the spin splitting significantly. From Ref. [109] we know that the hybridization strength between the sp_z - and p_{xy} -states depends on the outward relaxation of the Bi atoms. The observation of a band gap opening is consistent with a reduced outward relaxation of the Bi atoms after Xe adsorption. According to [109] a smaller outward relaxation is expected to result in a smaller spin splitting. The absence of a measurable effect of Xe adsorption on the size of the spin splitting for the Bi/Ag(111) surface alloy, however, indicates that the spin splitting is caused by a different mechanism than in Au(111) where Xe adsorption leads to a 30% increase of the spin splitting [99, 100].

The trend that an increased outward relaxation leads to an increase of the spin splitting in (Bi,Pb,Sb)/Ag(111) surface alloys is nicely confirmed by our $I(V)$ -LEED results in section 4.2 and Ref. [146].

6.5 Asymmetry of the wave function

In the previous sections we have seen that the mixing of different orbital contributions in the 2D wave function plays an important role for the RB-type spin splitting.

Ab initio calculations for the Ag(111) surface state predict that the RB-type spin splitting is a factor of 20 smaller than for the surface state on Au(111) [98]. This difference cannot be explained by the different atomic SOI in Ag and Au which differ by a factor

of four. The expansion of the surface state wave function in spherical harmonics reveals that the $p : d$ ratio is 9.5 in Ag(111) and 3.3 in Au(111). Furthermore, the $p : s$ ratio is larger in Ag(111) than in Au(111). In Ref. [98] the formation of hybrid states between orbitals with l - and $(l \pm 1)$ -character was identified as a crucial parameter for the size of the spin splitting. The comparatively pure p -character of the Ag(111) surface state shows a much smaller splitting than the Au(111) surface state where the admixture of both s - and d -orbitals is much larger than for Ag(111). The surface state of Lu(0001) at the $\bar{\Gamma}$ point with a $d : p$ ratio of 2.7 shows a spin splitting which is very similar in size to the Au(111) surface state. Around the \bar{M} point the RB-type spin splitting is much larger ($k_R = 0.085 \text{\AA}^{-1}$) which can be attributed to an almost equal weight of d_{xz} - and p_x -orbitals with a ratio of $d : p = 1.7$.

The considerable increase of the RB-type spin splitting upon oxide formation on a Gd(0001) surface is also accompanied by a changing orbital composition of the 2D electronic states [101]. The Gd(0001) surface state is almost symmetric with respect to the surface plane, reflecting the rather pure d_{z^2} -character with a $d : p$ ratio of approximately 8 : 1. The 2D state of the oxidized Gd surface is localized at the interface between the O/Gd surface monoxide layer and the next Gd layer where strong electric fields act on the wave function resulting in a high admixture of p_z -character to the d_{z^2} -state ($d : p \approx 5 : 1$).

For the (Bi,Pb)/Ag(111) surface alloys the spin splitting was found to increase with increasing outward relaxation of the (Bi,Pb) atoms [109]. This is related to the fact that the outward relaxation determines the orbital composition of the surface state. For an uncorrugated surface the surface state has sp_z -character with a comparatively large $s : p_z$ ratio [4:1 for Bi/Ag(111)]. Upon increasing the outward relaxation the weight of the s -orbital decreases. Further relaxation also adds some p_{xy} -character. In this case, it is not only the mixing of l - and $(l \pm 1)$ -orbitals but also the mixing of p_z - and p_{xy} -orbitals with the same angular momentum $l = 1$ due to the outward relaxation of the alloy atoms that leads to the giant spin splitting in surface alloys.

6.6 Influence of the substrate

The spin splitting for both one monolayer of Au and Ag on W(110) has a similar value despite the different atomic numbers of the adlayer, whereas no spin splitting has been observed when replacing the substrate by Mo(110) [126]. The Au/Ag-derived states hybridize with a spin split band of the clean substrate, and the resulting bands simply inherit the spin splitting of the substrate. If the spin splitting of the substrate is small like for Mo(110) the same holds for the new Au/Ag-Mo hybrid states.

When comparing the Bi/Ag(111) and the Bi/Cu(111) surface alloys one finds a large difference in the size of the spin splitting of the 2D band structure: the splitting is roughly four times smaller for Bi/Cu(111) ($k_R = 0.03 \text{\AA}^{-1}$) than for Bi/Ag(111) ($k_R = 0.13 \text{\AA}^{-1}$) [106, 108]. The 2D wave functions are strongly localized in the topmost layer. As the substrate atoms in the surface layer carry a considerable charge, Ref. [108] attributed the difference in spin splitting between Bi/Ag(111) and Bi/Cu(111) to the reduction in

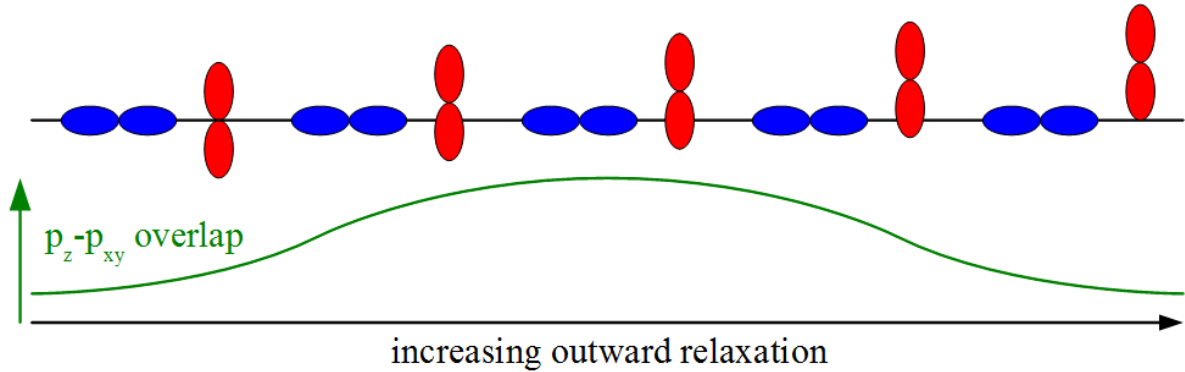


Figure 6.1: Schematic: influence of the outward relaxation on the overlap between Bi p_z - and (Ag,Cu) p_{xy} -orbitals in Bi/Ag(111) and Bi/Cu(111) surface alloys. When increasing the relaxation the overlap increases, reaches a maximum and decreases again.

the atomic spin-orbit parameter of the substrate atoms. This is in good agreement to [126], where the Au/Ag-W hybrid states simply inherit the spin splitting from the W(110) substrate.

However, when comparing the Bi/Ag(111) and Bi/Cu(111) surface alloys there is a second important parameter that differs between these two systems. The outward relaxation of the Bi atoms is much larger on the Cu(111) substrate than on the Ag(111) substrate. Ref. [106] investigated the influence of both the atomic SOI and the outward relaxation for Bi/Cu(111) and Bi/Ag(111) with the help of first-principles calculations. The authors found that artificially increasing the values of the SOI constants in the Cu alloy to match those found in the Ag alloy does not influence the size of the spin splitting. Hence, they concluded that the influence of the SOI strength of the substrate is negligible. Therefore, structural differences between the two alloys have to be responsible for the large difference of the observed spin splitting. The theoretically determined outward relaxations of the Bi atoms in the Bi/Ag(111) and Bi/Cu(111) surface alloys are $z_{\text{Ag}} = 0.85\text{\AA}$ and $z_{\text{Cu}} = 1.06\text{\AA}$, respectively. Artificially reducing the outward relaxation of the Bi atoms in Bi/Cu(111) to the value found for Bi/Ag(111) leads to a strong increase of the Rashba energy which becomes comparable to the value for Bi/Ag(111). In contrast to Ref. [108] the authors of Ref. [106] come to the conclusion that the atomic SOI of the substrate atoms plays no role for the Bi/Ag(111) and Bi/Cu(111) surface alloys and that the difference in spin splitting has to be attributed to the difference in outward relaxation alone.

For Bi/Cu(111) a reduction in outward relaxation leads to an increase in the size of the spin splitting. This is an obvious contradiction to the Bi/Ag(111) surface alloy where the opposite trend was observed [109, 146]. How can we resolve this issue? The outward relaxation of the Bi atom determines the overlap between Bi p_z - and (Ag,Cu) p_{xy} -orbitals and leads to an admixture of p_{xy} -orbitals to the sp_z surface state [109]. Consider the following Gedankenexperiment: If we assume that the Bi and the (Ag,Cu) substrate atoms are on the same plane, the overlap between Bi p_z - and (Ag,Cu) p_{xy} -orbitals is small and so

is the spin splitting. Upon increasing the Bi outward relaxation this overlap first increases, reaches a maximum and then decreases again. This is illustrated in Fig. 6.1. If one assumes that the Bi/Ag(111) surface alloy is located on the small relaxation side of this maximum, it is obvious that the p_z - p_{xy} overlap (and the spin splitting) first increases upon further outward relaxation of the Bi atom. For the Bi/Cu(111) surface alloy we observe the opposite effect: the spin splitting decreases upon increasing the outward relaxation. This can be explained if one assumes that the Bi/Cu(111) surface alloy is located on the large relaxation side of the maximum p_z - p_{xy} overlap. This assumption seems justified by the larger outward relaxation of the Bi atoms in the Bi/Cu(111) surface alloy as compared to the Bi/Ag(111) surface alloy.

6.7 Spin splitting in quantum well states

Recently, thin Bi or Pb films grown on Si(111) have attracted a lot of attention in the Rashba community, introducing again a different aspect concerning the origin of the RB-type spin splitting. In Ref. [112] it was shown that in ultrathin Bi films spin polarized surface states around $\bar{\Gamma}$ coexist with spin-degenerate quantum well states around the \bar{M} point. In contrast to the surface states that are mainly localized within the first bilayer close to the surface, the quantum well states are distributed over the whole Bi film. This makes the quantum well states insensitive to both the Si/Bi and the Bi/vacuum interface and the states remain spin degenerate. The surface state on the other hand is exposed to the Bi/vacuum interface and becomes spin-split.

Refs. [119,120] have investigated Bi/Ag surface alloys grown on thin Ag(111) quantum well films on Si(111). Similar to the thin Bi films the authors have observed a coexistence of spin-degenerate Ag(111) quantum well states and spin-split surface states originating from the 2D Bi/Ag surface alloy. At the points where surface states and quantum well states cross energy gaps open in the surface state band structure and the quantum well states become spin-polarized inside the surface state band gap.

Recently, it was shown with spin-resolved ARPES that the quantum well states in thin Pb films on Si(111) show a small RB-type spin splitting of about $k_R = 0.035\text{\AA}^{-1}$ with $\alpha_R = 0.04\text{eV\AA}$ [117]. The origin of this splitting has been attributed to the phase shift that the wave function experiences when reflected at both the Si/Pb and Pb/vacuum interfaces. This phase shift will induce asymmetries in the wave functions near the atomic nuclei, resulting in a nonvanishing local contribution to the Rashba constant. Each atomic layer makes its own contribution to the RB-type spin splitting which is proportional to the negative derivative of the envelope function (see Fig. 10 in Ref. [133]). There is no contribution to the spin splitting if the gradient of the envelope function is zero which results in a symmetric charge distribution around the nucleus. A nonzero gradient of the envelope function leads to an asymmetric charge distribution around the nucleus which gives a finite contribution to the spin splitting. The sign of this contribution is then determined by the slope of the envelope function. If the slope is positive the contribution to the spin splitting is negative and vice versa. The total Rashba constant is obtained

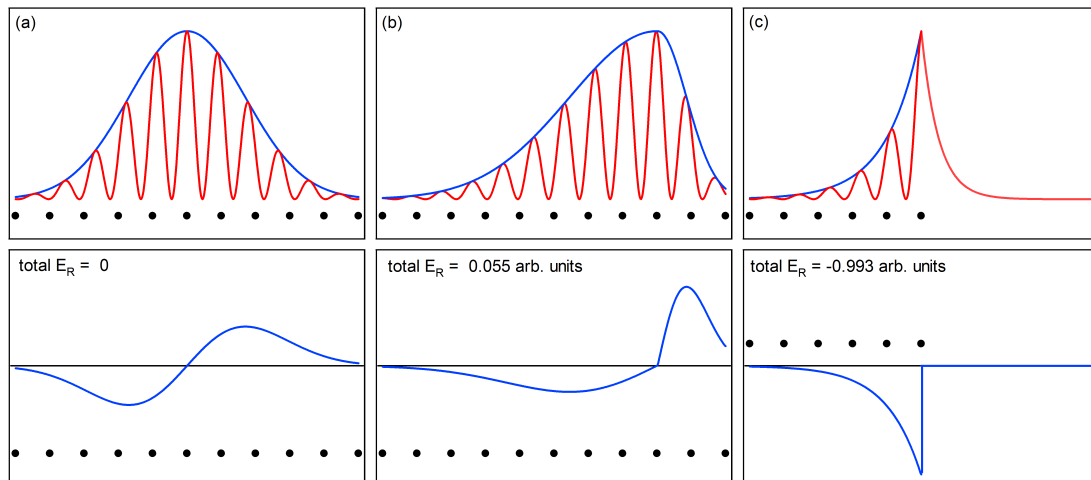


Figure 6.2: The red lines represent the electron density for a symmetric quantum well (a), an asymmetric quantum well (b) and a surface state (c). Blue lines indicate the envelope functions and black dots mark the positions of the atoms. The lower panel shows the negative derivative of the envelope functions. Each atomic layer makes its own contribution to the RB-type spin splitting which is proportional to the negative derivative of the envelope function. The total Rashba constant is obtained by the sum over all atomic layers.

by the sum over all atomic layers. For thin Pb films on Si(111) the influence of the two interfaces is opposite and the measured spin splitting is the resulting net effect [117, 133]. This is illustrated in Fig. 6.2. Panel (a) sketches the electron density for a symmetrically confined quantum well (upper panel) together with the negative derivative of the envelope function (lower panel). The atomic positions are indicated by black dots. Although every single atomic layer gives a nonzero contribution to the spin splitting, the net splitting obtained by the sum over all atomic layers is zero. For an asymmetric quantum well a finite net Rashba splitting remains [Fig. 6.2 (b)].

This model can also be applied to surface states [see Fig. 6.2 (c)]. For a surface state the asymmetric charge distribution around the nucleus is induced by the structural inversion asymmetry at the surface (in Ref. [98] this was expressed by mixing different l -components in the 2D wave function). Similar to the quantum well states the total Rashba splitting is obtained by the sum over all atomic layers. In contrast to quantum well states that are confined between two interfaces, surface states are only subjected to the crystal vacuum interface. This means that the contributions from the single atomic layers have the same sign and the total Rashba effect is — in general — larger than in quantum wells.

6.8 Summary

We will conclude this chapter with a short summary of the most important ingredients for a large RB-type spin splitting on surfaces. There is no spin splitting without inversion symmetry breaking and without strong atomic electric fields. Apart from that we have

seen that the corrugation of the surface plays an important role. From a microscopic point of view we have learned that an asymmetric charge distribution around the nucleus (characterized by mixing l - with $(l \pm 1)$ - and p_{xy} - with p_z -orbitals in the 2D wave function) lies at the heart of the RB-type spin splitting. This means that without detailed structural knowledge it is impossible to predict the size of the spin splitting correctly. When looking for a new material with a large RB-type spin splitting one should look for a 2D structure containing heavy atoms with both in-plane and perpendicular inversion asymmetry. The corrugation of the surface should be in the range that allows for optimum overlap between p_{xy} - and p_z -orbitals on neighboring atoms, and the 2D states should be localized close to heavy nuclei where the potential gradients are largest.

Chapter 7

Graphene

Graphene is an excellent candidate for the next generation of electronic materials due to the strict two-dimensionality of its electronic structure as well as the extremely high carrier mobility [8, 20, 179]. In order to achieve this ambitious goal several obstacles have to be overcome. Graphene is a semimetal with the conduction and valence band touching at the \bar{K} -point of the 2D Brillouin zone where they form a Dirac cone. The absence of a band gap leads to comparatively low on-off ratios in graphene-based FETs. Therefore, one important issue is to open up a band gap at the Dirac point [75, 180–184]. Such a band gap will be present in graphene nanoribbons due to quantum confinement of the charge carriers. Recently, it has been shown that graphene nanoribbons with smooth edges and controllable widths can be obtained by unzipping multi-walled carbon nanotubes by plasma etching [185]. Furthermore, Ref. [13] has presented self-organized growth of graphene nanoribbons on a templated SiC substrate. Another prerequisite for the development of graphene based electronics is the reliable control of the type and density of the charge carriers by external (gate) and internal (doping) means. While gating has been successfully demonstrated for graphene flakes [8, 28, 186] and epitaxial graphene on silicon carbide [187, 188], the development of reliable chemical doping methods turns out to be a real challenge. The most important task, however, is to find a method for graphene growth suitable for large scale production. The best way to achieve this is by growing graphene on the Si-face of SiC. This growth process offers the advantage of growing graphene directly on a semiconducting substrate and of precise thickness control. Unfortunately, the presence of the substrate alters the electronic properties of graphene and reduces its carrier mobility. Therefore, it is necessary to find a way to decouple the graphene layer from the SiC substrate.

Sample preparation Our graphene samples were prepared according to the description given in section 2.1.3. The 4H- or 6H-SiC(0001) crystals were hydrogen-etched prior to insertion into UHV. Subsequent Si deposition at 800°C sample temperature has been applied to remove oxygen impurities. After this process a homogeneous and sharp (3×3) LEED pattern appeared. The first carbon monolayer (ZL) is formed after annealing the samples at 1100°C for five minutes. Further annealing at 1150°C for five minutes leads to the formation of a graphene monolayer.

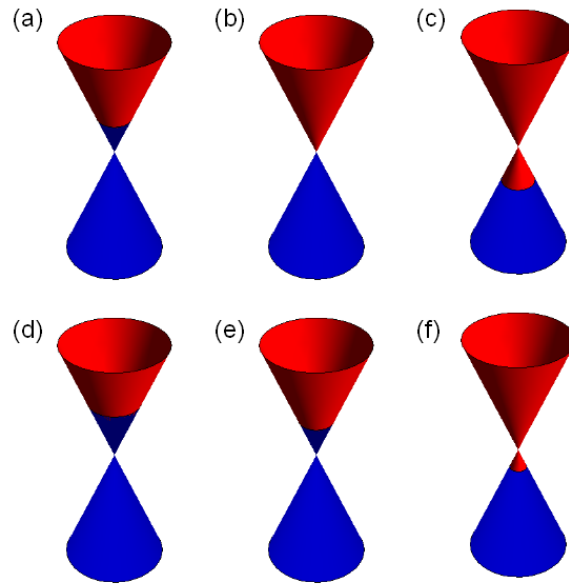


Figure 7.1: Doping graphene: position of the Dirac point and the Fermi level of pristine (upper panel) and epitaxial graphene on SiC (lower panel) as a function of doping. The left and right panels visualize n-type and p-type doping, respectively, while the center panels show the pure graphene layers. For the epitaxial graphene a natural substrate induced n-type doping is present. Occupied (unoccupied) states are shown in blue (red)

7.1 Atomic hole doping of graphene

Graphene's band structure provides great potential for electronic devices, and one of the key questions is how to dope the electronic structure with electrons or holes appropriately for the different devices. The conical shape of the bands results from a delicate balance between the electrons and the lattice. The challenge here is to interact with the system just enough to add or remove electrons but not too much so as to modify or even collapse the electronic structure. Therefore, it is not an option to replace atoms within the graphene layer, as is common practice when doping e. g. silicon.

For graphene the doping is usually realized by adsorbing atoms and/or molecules on its surface, i. e. surface transfer doping [189–192]. For n-type (p-type) doping the electrons have to be released into (extracted out of) the graphene layer. A schematic sketch that compares the doping-behavior of free-standing graphene with that of epitaxial graphene on SiC is displayed in Fig. 7.1. The most significant difference between free-standing and epitaxial graphene on SiC is that epitaxial graphene is naturally n-doped due to charge transfer from the substrate [see Fig. 7.1 (b) and (e)].

As alkali atoms easily release their valence electron, they very effectively induce n-type doping [74, 75] [see Fig. 7.1 (a) and (d)]. In the case of epitaxial graphene, the Dirac point, where the apices of the two conically shaped bands meet, is shifted further into the occupied states away from the Fermi level. However, aside from the fact that epitaxial

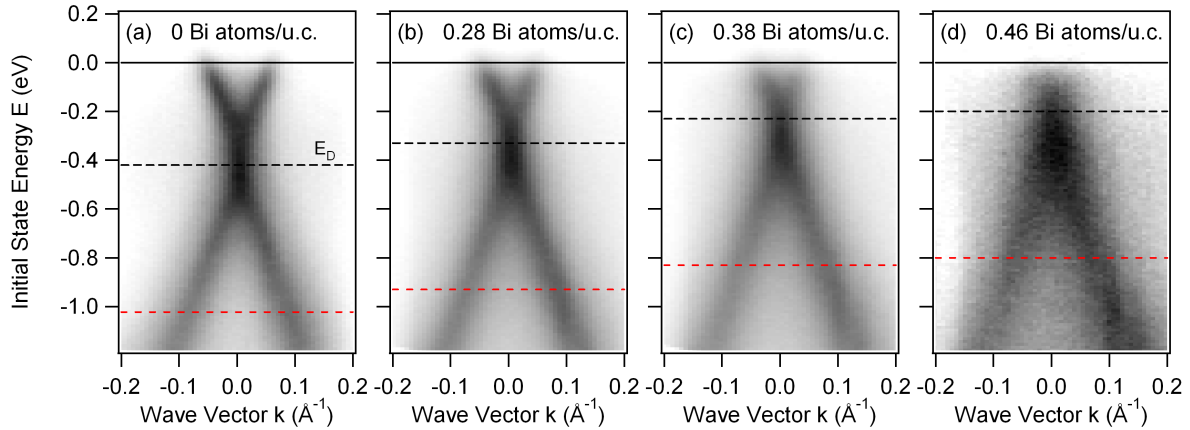


Figure 7.2: Experimental band structure of epitaxial graphene doped with bismuth atoms. (a) pristine graphene layer, (b)-(d) increasing amounts of bismuth atoms have been deposited.

graphene on silicon carbide is naturally n-doped, alkali atoms are very reactive and their suitability in electronic devices is more than questionable.

P-type doping for graphene [see Fig. 7.1 (c) and (f)] is quite a bit more challenging. Many of the elements with a high electronegativity — e. g. nitrogen, oxygen, or fluorine — form strong dimer bonds. They would not likely form a stable adlayer on the graphene surface. Therefore, different molecules such as NO_2 , H_2O , NH_3 , or the charge transfer complex tetrafluoro-tetracyanoquinodimethane (F4-TCNQ) have been used to induce p-type doping in graphene [193–196]. However, NO_2 , H_2O and NH_3 are very reactive chemicals and therefore not suitable for use in an electronic material. F4-TCNQ on the other hand plays an important role in optimizing the performance in organic light emitting diodes [197,198] but would be incompatible with high temperature processes. In the following we will show by ARPES that substantial hole doping in the conical band structure of epitaxial graphene monolayers can be achieved by simple atomic doping via the adsorption of bismuth, antimony, or gold.

Bi and Sb were deposited on a room temperature sample using a commercial electron beam evaporator which was calibrated with the help of the $(\sqrt{3} \times \sqrt{3})$ reconstruction that is formed for $1/3$ monolayer coverage of both Bi and Sb on Ag(111). Au was deposited at room temperature with a commercial Knudsen cell which was calibrated using a quartz crystal microbalance. After Au deposition the sample was annealed at a minimum temperature of 700°C for 5min.

Fig. 7.2 shows the experimental band structure of an epitaxial graphene monolayer on SiC(0001) doped with successively higher amounts of Bi atoms. The initial state energy E of the bands is plotted as a function of the electron wave vector k ¹. The intensity scale is linear with light and dark areas corresponding to low and high photoelectron current, respectively. Fig. 7.2 (a) shows the pristine graphene layer. The linear dispersion of the

¹The measurements were taken at the $\bar{\text{K}}$ -point with the wave vector axis perpendicular to the $\bar{\Gamma\text{K}}$ high symmetry line.

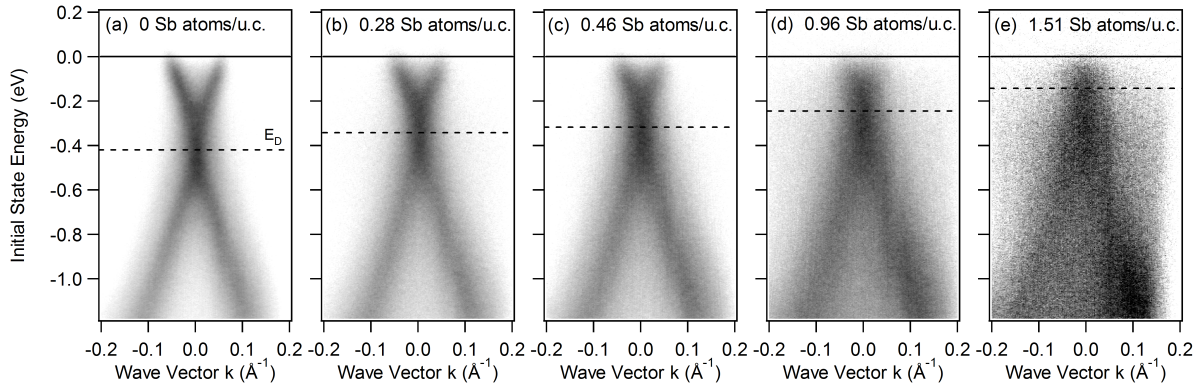


Figure 7.3: Experimental band structure of epitaxial graphene doped with antimony atoms. (a) pristine graphene layer, (b)–(e) increasing amounts of antimony atoms have been deposited.

valence and conduction bands is clearly visible. Due to the charge transfer with the SiC-substrate, the Dirac cone of the conduction band is partially filled shifting the Dirac point into the occupied states by about 420 meV [74,76]. Figs. 7.2 (b)–(d) display the evolution of the band structure when successively higher amounts of bismuth atoms per graphene unit cell (u.c.) as indicated in each panel are deposited on the graphene layer². As the bismuth coverage increases the Dirac point clearly shifts towards the Fermi level. Otherwise, the band structure remains unaltered by the bismuth adatoms, i. e. the linear dispersion is preserved. With increasing Bi coverage the number of free charge carriers decreases as a successively smaller cross section of the conduction band intersects the Fermi level.

At higher bismuth coverage the line width of the bands as well as the background increases. This is shown in more detail in Fig. 7.4. The graph shows momentum distribution curves for different Bi coverages at an energy of 600 meV below the Dirac point (see dashed lines in Fig. 7.2). The full widths at half maximum (FWHM) are given on the right side. They indicate that the line width increases with increasing Bi coverages. This is probably related to the fact that Bi atoms do not form an ordered structure but rather tend to form clusters on the surface, which leads to broadening of the photoemission features.

Very similar results have been obtained for antimony atoms deposited on the graphene layer. Antimony is also located in group V of the periodic table just above bismuth, so that a very similar doping behavior is expected. The experimental band structure is shown in Fig. 7.3, and looks very much like the data obtained for bismuth on graphene except that it takes a higher antimony coverage to reach the same doping level.

A more quantitative analysis of the bismuth and antimony doping is displayed in Fig. 7.5. Panel (a) shows the evolution of the Dirac point as a function of the coverage, which is given in number of atoms per graphene unit cell. The Dirac point clearly approaches the Fermi level with increasing doping indicating that there is charge transfer from the graphene layer to the adatoms. A simple theoretical model based on the linear density of states for the graphene layer has been used to estimate the doping effect of the bismuth

²The graphene unit cell has a lattice constant of 2.46 Å and contains two carbon atoms.

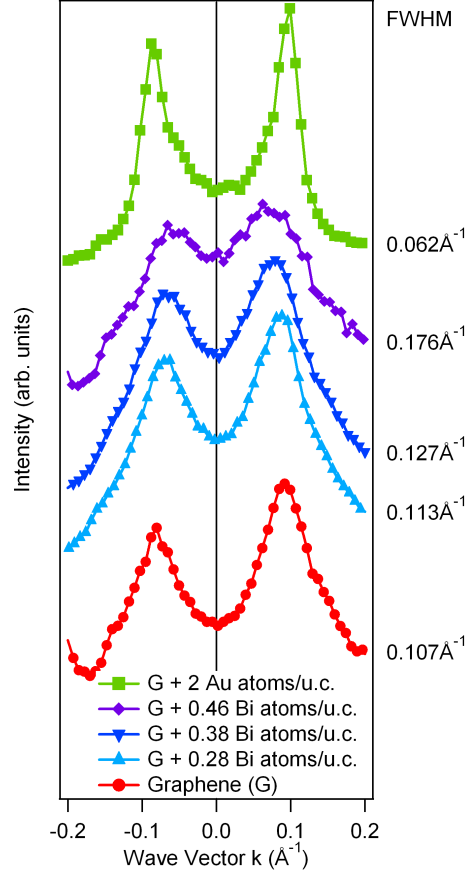


Figure 7.4: Momentum distribution curves for graphene and different adatom quantities. The cuts were taken 600 meV below the Dirac point (see dashed red lines in Fig. 7.2 and 7.6). The full widths at half maximum (FWHM) for the corresponding spectra are given at the right side of the panel. The spectra have been shifted with respect to each other.

atoms assuming that the charge transfer is proportional to the amount of dopant atoms:

$$E_D = -\sqrt{\pi}\hbar v_F \sqrt{N_0 - N_h} \quad (7.1)$$

Here E_D is the Dirac point, with the zero of the energy scale referenced to the Fermi level. The Fermi velocity $\hbar v_F = 6.73 \text{ eV}\text{\AA}$ was determined experimentally from the slope of the linear band structure for monolayer graphene and agrees well with values given in literature [20, 74], N_0 is the number of electrons in the conduction band for zero doping, and N_h is the number of holes doped into the graphene layer. Using Eq. (7.1) we find that about 0.01 electrons per bismuth atom and 0.0036 electrons per antimony atom are extracted from the graphene layer. The Dirac point follows the respective solid lines plotted in Fig. 7.5 (a). It would reach the Fermi level for a coverage of 0.61 bismuth atoms and 1.65 antimony atoms per unit cell. The experiment shows, however, that for higher coverages the bands become broader and less well-defined. At this point the average distance between

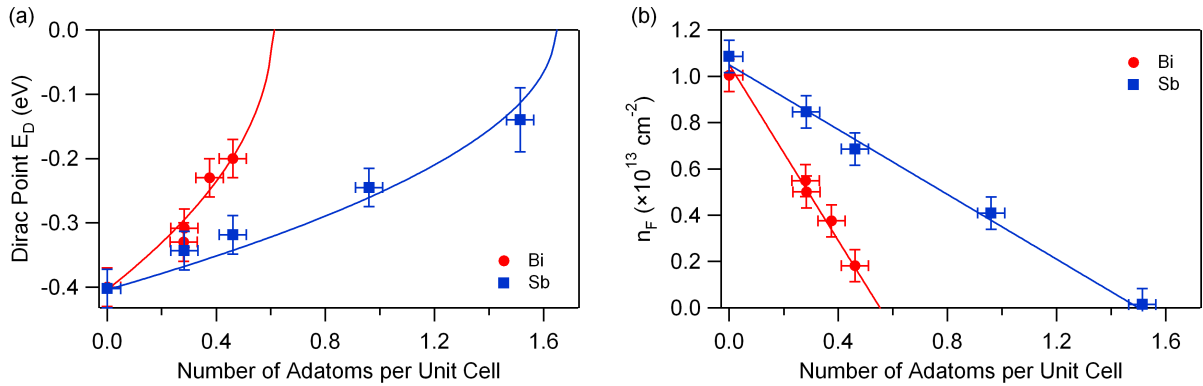


Figure 7.5: Doping parameters of Bi and Sb: (a) position of the Dirac point E_D and (b) free charge carrier density n_F as a function of doping with bismuth atoms (red circles) and antimony atoms (blue squares) measured in adatoms per graphene unit cell. The solid lines represent a simple model calculation assuming an electron transfer of 0.01 and 0.0036 electrons per Bi and Sb atom, respectively.

adatoms approaches the one of monolayer coverage which makes a cluster formation of the Bi atoms very likely, so that the photoelectrons will interact and scatter in the Bi clusters.

In Fig. 7.5 (b), the free charge carrier density n_F of the graphene layer is plotted as a function of adatoms per unit cell. n_F is proportional to the area enclosed by the Fermi surface and therefore can be extracted from the experimental data through the Fermi wave vector k_F . Here we assume a circular Fermi surface with an area of πk_F^2 and take into account that the density of states in momentum space is constant. Including the spin and valley degeneracy the free charge carrier density is given by $n_F = k_F^2/\pi$. The charge carrier density is clearly reduced as the number of adatoms increases, indicating hole doping. The solid lines in Fig. 7.5 (b) show a linear dependence of the charge carrier density as a function of bismuth/antimony coverage with a very good correspondence to the experimental data assuming the same values for the electron transfer per adatom as above.

For actual p-type doping with holes as charge carriers, the Dirac point has to shift into the unoccupied states. A further increase of the electron transfer from the graphene layer to the adatoms is desirable. The natural starting point would be an element with a higher electron affinity than bismuth or antimony. Motivated by this, we have deposited gold atoms on epitaxial graphene, as its electron affinity is about twice as high as for bismuth and as recent phototransport experiments indicated that gold contacts induce p-doping in graphene [199]. The experimental band structure for about two gold atoms per graphene unit cell shown in Fig. 7.6 clearly displays p-type doping. Both branches of the valence band cone clearly cross the Fermi level close to the \bar{K} -point leaving the valence band partially unoccupied. By extrapolating the linear band structure into the unoccupied states we estimate the Dirac point to be about 100 meV above the Fermi level. The free charge carrier density of the holes is about $5 \times 10^{11} \text{ cm}^{-2}$. This means that the Dirac point is shifted by about 520 meV compared to the pristine graphene layer.

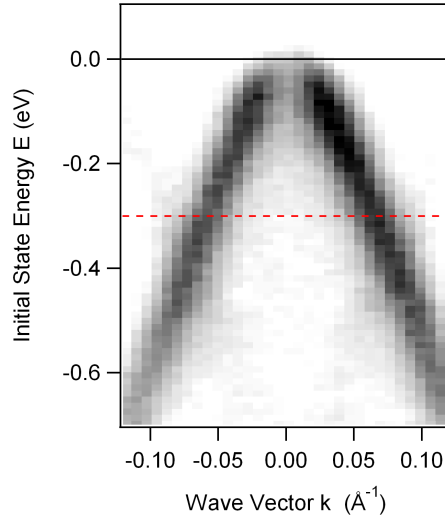


Figure 7.6: Hole doping with Au: experimental band structure of Au atoms on epitaxial graphene. The bands are well defined with the Dirac point at about 100 meV above the Fermi level and a charge carrier density for the holes of about $5 \times 10^{11} \text{ cm}^{-2}$.

We can compare these experimental findings with theoretical calculations in the literature for graphene doped by metal contacts [200] as well as metal adlayers on graphene [201]. There is a good qualitative agreement as hole doping is predicted for both the gold adlayer as well as the gold contact. Quantitatively, Ref. [200] predicts that the Dirac point should be located about 200 meV above the Fermi level for graphene doped by gold contacts which is slightly larger than the value we find. However, Ref. [200] also shows that the doping behavior critically depends on the graphene to metal distance. Upon decreasing the distance between graphene and metal layer the Dirac point shifts downwards which could explain the difference between the predicted and the experimentally observed doping behavior. The work function shift calculated for a gold adlayer in Ref. [201] cannot be directly compared to the experimental data, because both the position of the Fermi level as well as the core level shift are influenced by a number of different contributions, such as charge transfer or the local chemical environment.

The bands in Fig. 7.6 are much narrower than for the bismuth adatoms in Fig. 7.2 (d) even though the gold coverage is much higher than the bismuth coverage. This can be seen in the momentum distribution curve in Fig. 7.4. The line width decreases substantially by about 40% compared to the clean graphene layer. The sharp band structure suggests that gold forms an ordered structure with respect to the graphene layer. Furthermore, the scattering rate is decreased because of the lower charge carrier density according to Refs. [74, 194]. Interestingly, the p-type doping in Fig. 7.6 is only induced after a post-annealing of the sample to at least 700°C. In the following section we will show that the Au atoms actually intercalate below the graphene layer. This clearly goes beyond the idea of surface transfer doping. Nevertheless, the peculiar band structure of graphene with its linear dispersion remains intact. Our findings demonstrate that for a coverage of about

two gold atoms per graphene unit cell the Dirac point can be shifted above the Fermi level leaving the valence band partially unoccupied. Surprisingly, the estimated electron transfer is only 0.0024 electrons per gold atom, which is only a quarter of the value found for bismuth.

Our results demonstrate that p-type doping of an epitaxial graphene layer is possible by means of simple atoms. While bismuth and antimony are only able to shift the Dirac point in the direction of the Fermi level, i. e. reduce the natural n-type doping of the substrate, gold actually shifts the Dirac point into the unoccupied states thereby inducing p-type doping. Epitaxial graphene on silicon carbide becomes a feasible alternative to conventional electronic materials as n-type doping is naturally induced and p-type doping can be achieved by doping with gold atoms, which are easily processed.

7.2 Electronic decoupling of epitaxial graphene

The application of graphene in electronic devices requires large scale epitaxial growth either by cracking organic molecules on catalytic metal surfaces [44, 48, 49, 53, 202] or by thermal graphitization of SiC [71, 74–76, 203]. Unfortunately, the presence of the substrate alters the electronic properties of the graphene layer on the surface and reduces the carrier mobility. Therefore, in order to preserve its unique properties, it is necessary to decouple the graphene layer from the substrate. Even though it has been shown that the graphene layer can be decoupled from a metallic substrate [41–44] the system remains unsuitable for device applications. The ideal solution would be to grow graphene on the Si-face of SiC (which allows for a precise thickness control and provides a semiconducting substrate at the same time) and to subsequently decouple the graphene layer from the substrate [77].

We have grown graphene on SiC(0001), i. e. the Si-face, where the comparatively strong graphene-to-substrate interaction results in uniform, long-range ordered layer-by-layer growth. Annealing the sample at 1100°C for five minutes in UHV leads to the formation of the ZL. The partial sp^3 -hybridization of the ZL prevents the formation of π -bands and, therefore, the ZL has no graphene properties. Instead, its band structure consists of two non-dispersing bands at about -0.3 eV and -1.2 eV initial state energy. This can be seen in the first panel of Fig. 7.7 (a), where the experimental band structure of the ZL (black) measured by ARPES near the \bar{K} -point of the surface Brillouin zone is shown.

Upon further annealing at 1150°C for five minutes a purely sp^2 -hybridized carbon layer forms on top of the ZL which shows the linear band structure characteristic of massless charge carriers in graphene. The band structure of this “conventionally” grown graphene monolayer (cML) near the \bar{K} -point is shown in the second panel of Fig. 7.7 (a). The cML is influenced considerably by the underlying SiC substrate. It is n-doped with the crossing point of the two linear bands (Dirac point) at $E_D = -420$ meV due to charge transfer from the substrate [74–76], the possibility of a substrate-induced band gap opening has been discussed [71, 76, 80, 204, 205], and in addition to that, the strong substrate influence reduces the carrier mobility considerably [12].

The $(6\sqrt{3} \times 6\sqrt{3})R30^\circ$ reconstruction of the ZL diffracts the outgoing photoelectrons giving rise to the formation of replica bands [71]. This is nicely seen in the measured Fermi surface of the cML around \bar{K} in the left panel of Fig. 7.7 (b). The size of the Fermi surface is determined by the charge carrier density $n = k_F^2/\pi$, where k_F is the Fermi wave vector with respect to the \bar{K} -point. The values are summarized in Table 7.1. The intensity distribution on the Fermi surface is not symmetric with respect to the \bar{K} -point. Only one of the two linearly dispersing π -bands is visible along the $\bar{\Gamma}\bar{K}$ direction (i.e. along k_y) because of interference effects in the photoemission process related to the two carbon atoms per unit cell [206].

To reduce the influence of the substrate we developed a new method for the epitaxial growth of graphene on the Si-face of SiC. We start with the preparation of the ZL exploiting the strong substrate influence for uniform growth. On top of the ZL, we deposit Au atoms from a commercial Knudsen cell at room temperature. The gold coverage was calibrated

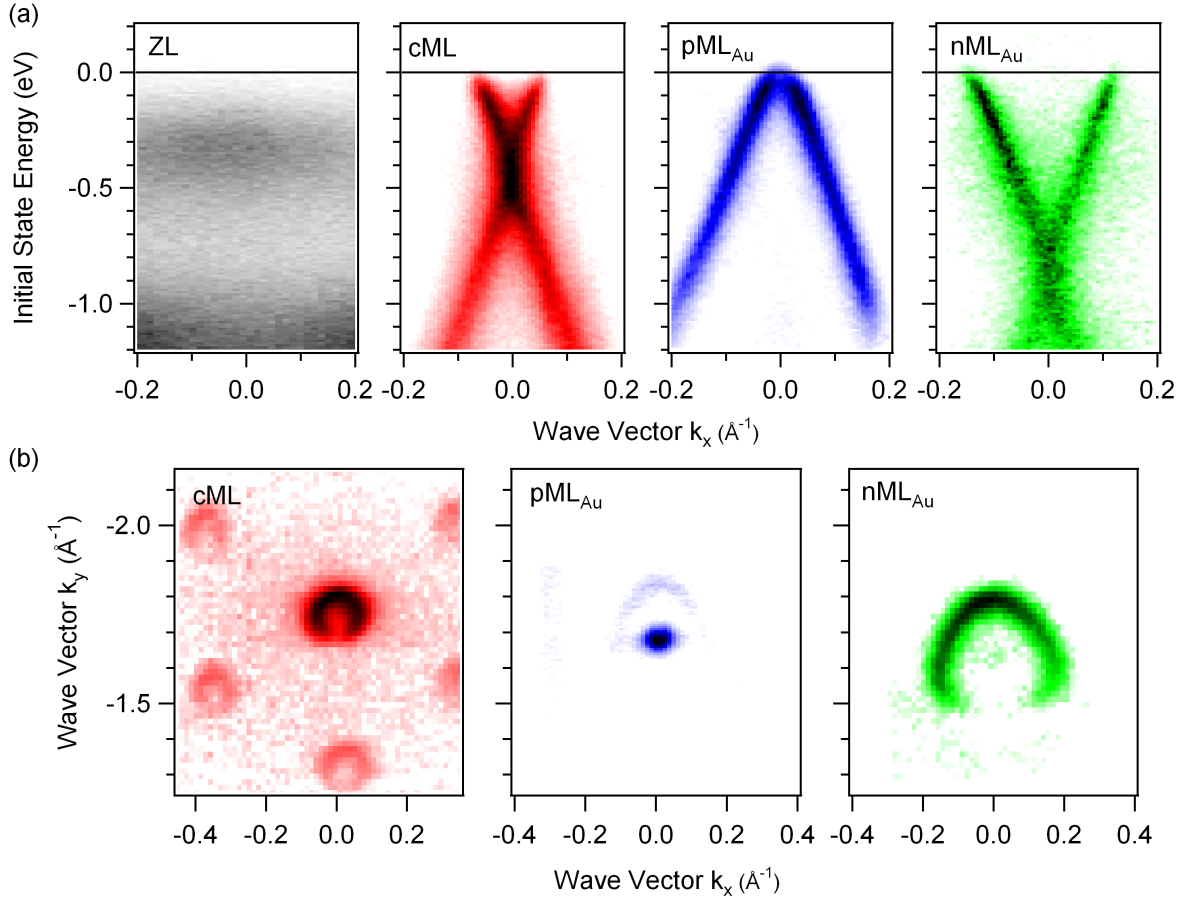


Figure 7.7: Comparison of ARPES data for conventional graphene on SiC and graphene intercalated with Au: panel (a) shows the band structure measured in the direction perpendicular to the $\overline{\Gamma\text{K}}$ direction near the $\overline{\text{K}}$ -point of the surface Brillouin zone of the zero layer (black), the conventional graphene monolayer (red), the p-doped graphene monolayer intercalated with gold (blue) and the n-doped graphene monolayer intercalated with gold (green) together with the corresponding Fermi surfaces in panel (b). The Fermi surfaces are plotted on a logarithmic color scale to enhance weak features. The Fermi surfaces for the cML and nML_{Au} were measured with a step size of 0.25° along the $\overline{\Gamma\text{K}}$ direction. As the line width for the pML_{Au} is narrower than for the cML and the nML_{Au} we had to reduce the stepsize to 0.1° to allow for reasonable accuracy. k_y is along the $\overline{\Gamma\text{K}}$ direction, k_x is perpendicular to the $\overline{\Gamma\text{K}}$ direction. The Fermi surface for the p-doped graphene monolayer shows a weak contribution of the n-doped phase due to an inhomogeneous Au coverage on the sample.

	cML	pML _{Au}	nML _{Au}
Au coverage (ML)	0	1	1/3
Au-Si 4f_{5/2} (eV)		88.20	89.05
Au-Si 4f_{7/2} (eV)		84.54	85.41
Au-Au 4f_{5/2} (eV)		87.82	88.32
Au-Au 4f_{7/2} (eV)		84.15	84.68
charge carrier	1×10^{13}	7×10^{11}	5×10^{13}
density (cm⁻²)	electrons	holes	electrons
Dirac point (meV)	-420	+100	-850

Table 7.1: Characteristic parameters for cML, pML_{Au} and nML_{Au} determined from the photoemission experiments.

using a quartz oscillator. After subsequent annealing of the sample at 800°C the linear dispersion typical for graphene appears. Because graphitization of SiC only takes place for temperatures higher than 1000°C we can exclude additional graphene growth at 800°C. Depending on the gold coverage (about one third or one monolayer, respectively), either a strongly n-doped (nML_{Au}) or a p-doped (pML_{Au}) graphene layer is formed. The band structures for the pML_{Au} and the nML_{Au} are compared in Fig. 7.7 (a). In contrast to the ZL, both the pML_{Au} (blue) and the nML_{Au} (green) clearly show two linearly dispersing π -bands. The Dirac point for the pML_{Au} is about 100 meV above the Fermi level. This band structure looks similar to the one shown in Fig. 7.6. However, there the graphene monolayer was prepared by depositing Au directly on a cML and not on a ZL. For the nML_{Au} the bands cross at about -850 meV. The band structure of the cML is a superposition of the band structure of the underlying ZL and the graphene monolayer. Both pML_{Au} and nML_{Au}, however, are formed directly from the ZL. There is no additional carbon layer between the graphene layer and the substrate, and the band structure around the \bar{K} -point is given by the pML_{Au} and nML_{Au} alone. The charge carrier densities deduced from the size of the Fermi surface [see middle and right panel of Fig. 7.7 (b)] are listed in Table 7.1.

Comparing the Fermi surfaces for the cML (red), the pML_{Au} (blue), and the nML_{Au} (green) in Fig. 7.7 (b), the most striking difference is the absence of replica bands for the pML_{Au} and nML_{Au}. Even on the logarithmic color scale of Fig. 7.7 (b) the replica bands are invisible, indicating a reduced influence of the $(6\sqrt{3} \times 6\sqrt{3})R30^\circ$ reconstruction.

This finding is supported by the LEED images shown in Fig. 7.8. They were recorded at 126 eV electron energy because this energy is particularly sensitive to the graphene coverage [208]. The image for the cML shows the graphene (10) spot surrounded by satellite peaks from the $(6\sqrt{3} \times 6\sqrt{3})R30^\circ$ reconstruction. The graphene (10) spot and the two lower left satellite spots have roughly the same intensity. For the ZL there is no graphene spot visible, only the satellite spots are there. The pML_{Au} has a very bright graphene spot, whereas the satellite peaks are considerably reduced in intensity. Furthermore, the distance between the satellite peaks and the graphene peak is smaller than for the cML indicating a larger lattice constant of the superstructure. This can be related to an increase of the

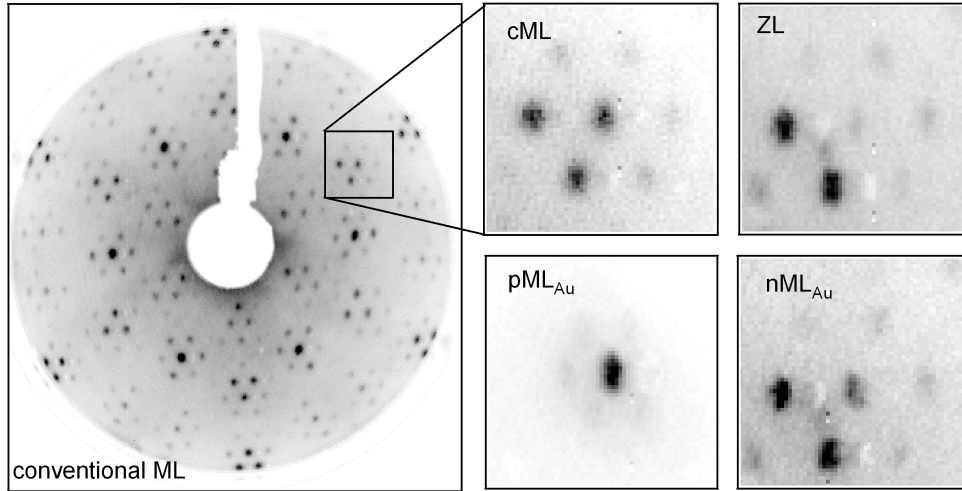


Figure 7.8: LEED images taken at 126 eV for the conventional graphene monolayer (cML), the zero layer (ZL), the p-doped graphene monolayer (pML_{Au}) and the n-doped graphene monolayer (nML_{Au}). The relative intensity between graphene spot and satellite spots is a measure for the strength of the substrate influence on the graphene layer.

lattice constant in the pML_{Au}. The LEED image for the nML_{Au} is very similar to that of the cML indicating a similar influence of the underlying substrate in both cases. We conclude that only the pML_{Au} is less influenced by the underlying substrate. We attribute this to an increased graphene-to-substrate distance as will be discussed later.

To analyze the band structure in more detail and gain access to the relevant scattering mechanisms we determined the full width at half maximum (FWHM) of the bands by fitting momentum distribution curves (MDCs) along the $\bar{\Gamma}\bar{K}$ direction with Lorentzian line shapes and a constant background. The FWHM as a function of the initial state energy for the cML (red), the pML_{Au} (blue) and the nML_{Au} (green) are shown in Fig. 7.9 (a). From the data in Fig. 7.9 (a) a constant offset of 0.023 \AA^{-1} (cML), 0.027 \AA^{-1} (pML_{Au}), and 0.041 \AA^{-1} (nML_{Au}) has been subtracted. For both cML and pML_{Au} this offset is mainly determined by the experimental resolution. For the nML_{Au}, however, the line width offset is significantly larger than the limit set by the experimental resolution. In this case the offset is determined by impurity scattering which gives a constant contribution to the line width at all energies.

There are three main contributions to the quasiparticle lifetime in graphene [71, 74]. The increase in line width around 200 meV is caused by electron-phonon coupling which depends on the size of the Fermi surface. Therefore, its influence is largest for strongly n-doped graphene (nML_{Au}). The pronounced maximum near the Dirac point is attributed to electron-plasmon scattering. The third contribution to the line width is electron-electron scattering, which has been found to be proportional to $|E - E_F|^\alpha$, where $1 < \alpha < 2$ [74]. The FWHM for our cML is in good agreement with the data reported in Ref. [71, 74]. Also, the cML and the nML_{Au} have a similar line width. The main difference between the two is the position of the plasmon peak which is determined by the position of the Dirac

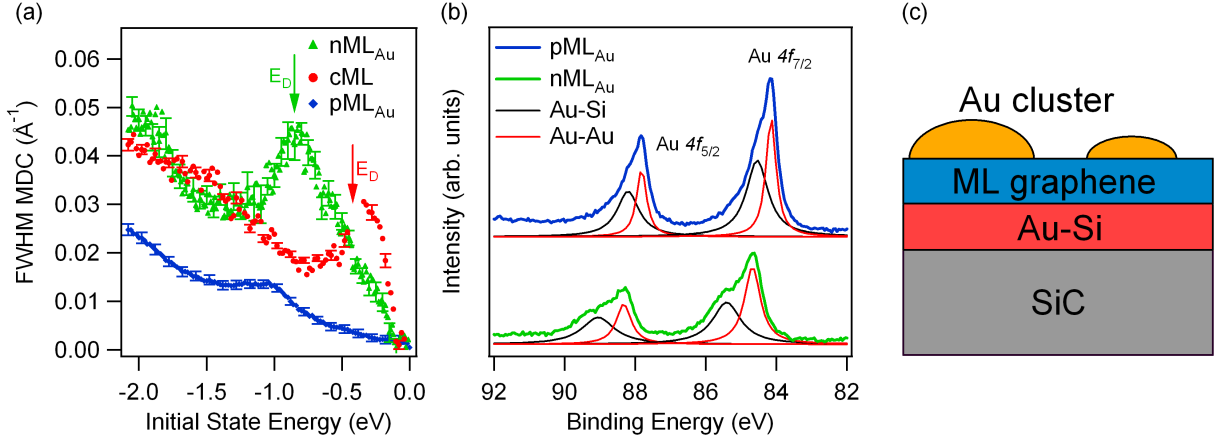


Figure 7.9: line width analysis, Au 4*f* core level spectra and schematic: Panel (a) shows the full width at half maximum (FWHM) of momentum distribution curves obtained from Fig. 7.7 (a) for the conventional graphene monolayer (red), the p-doped graphene monolayer intercalated with Au (blue) and the n-doped graphene monolayer intercalated with Au (green). A constant background was subtracted from the data so that the plotted line width is determined by electron-phonon, electron-plasmon and electron-electron scattering alone. Panel (b) shows the Au 4*f* core level spectra recorded with an incident photon energy of 150 eV for the p-doped monolayer (blue) and the n-doped monolayer (green). The core level spectra indicate the presence of Au-Si bonds (black lines) for both the p- and the n-doped monolayer which is consistent with the schematic (not to scale) shown in panel (c).

point and hence the doping level. The pML_{Au} , however, has a much lower line width over the whole range of energies indicating a reduced electron-electron scattering. As the Fermi surface for the pML_{Au} is rather small [see Fig. 7.7 (b)] the electron-phonon contribution to the line width is negligible. The local maximum in line width around -1 eV initial state energy for the pML_{Au} is not located at the Dirac point. Therefore, we do not interpret this as originating from plasmons within the graphene layer according to [71, 74]. Varykhalov *et al.* [44] found a similar feature for graphene/Au/Ni(111) which they attributed to a residual interaction between Au and graphene. The overall much smaller line width for the pML_{Au} corroborates the conclusion from LEED that the pML_{Au} is decoupled from the substrate. As mentioned before, the measured line width for the pML_{Au} near the Fermi level is mainly determined by the experimental momentum resolution of $\Delta k = 0.023 \text{ \AA}^{-1}$. This allows us to estimate a lower limit for the carrier lifetime using $\tau = \hbar / (\hbar v_F \Delta k)$. With $\hbar v_F = 7.06 \text{ eV \AA}$, we find that $\tau \leq 4 \text{ fs}$ which is the same order of magnitude as the value reported for multilayer graphene on the C-face of SiC [64].

To gain a deeper insight into the structure of the pML_{Au} and nML_{Au} , we measured the Au 4*f* core level spectra using a photon energy of 150 eV at the SRC. The data was fitted with Lorentzian peaks including a Shirley background. The spectra in Fig. 7.9 (b) for the pML_{Au} (blue) and the nML_{Au} (green) show two different contributions to the Au 4*f* core level. The doublet at higher binding energy was attributed to a gold-silicide (Au-

Si) configuration in earlier experiments with Au-deposition on SiC(0001) [209, 210]. The doublet at lower binding energy belongs to Au-Au bonds [134]. The peak positions are summarized in Table 7.1. The ratio between the integrated intensities for the gold-silicide doublet in the nML_{Au} and pML_{Au} is $Au-Si(nML_{Au}):Au-Si(pML_{Au})=0.39$ indicating that the amount of gold-silicide in the pML_{Au} is roughly three times larger than in the nML_{Au} .

Combining these observations with the band structures in Fig. 7.7, we can deduce a schematic (not to scale) as depicted in Fig. 7.9 (c). The appearance of a linear dispersion typical for graphene implies that the C-Si bonds between ZL and substrate break and a completely sp^2 -hybridized carbon monolayer is created. The core level spectra show the existence of gold-silicide for both the nML_{Au} and the pML_{Au} . We conclude that the Au atoms intercalate between the ZL and the substrate breaking the C-Si bonds to form gold-silicide. From the core level peak intensity for the nML_{Au} , we find about one third monolayer of Au intercalated (one monolayer corresponds to two Au atoms per graphene unit cell). We note that about every third carbon atom in the ZL forms a C-Si bond [11]. In view of the recovery of the sharp linear π -band structure this suggests that the intercalated gold sufficiently coordinates the Si atoms of the topmost SiC bilayer to completely suppress the covalent interface bonding. For the pML_{Au} , about one monolayer of gold is intercalated. From atomic force microscopy (AFM) and STM measurements (see Fig. 7.10), we find that additional Au atoms are not intercalated, but form Au clusters on top of the graphene layer which leads to the appearance of the Au-Au doublet in the Au $4f$ core levels. The ratio between the integrated intensities for the Au-Au and the Au-Si component is close to one for both pML_{Au} and nML_{Au} . Despite the fact that a complete monolayer of gold is intercalated for the pML_{Au} the substrate does not become metallic. Apart from the graphene bands, there are no other states visible at the Fermi energy.

The doping behavior for different Au coverages has been addressed by the theoretical work of Giovannetti *et al.* [200] who predicted p-type doping for graphene on a Au substrate. Reducing the Au-graphene distance to $d_{AuG} < 3.2 \text{ \AA}$, however, will lead to n-type doping. The larger amount of intercalated Au for the pML_{Au} should increase the distance between graphene and substrate. This is consistent with the observed doping behavior as well as the reduced influence of the $(6\sqrt{3} \times 6\sqrt{3})R30^\circ$ interface reconstruction on the Fermi surface and the LEED images of the pML_{Au} .

The peak position for the Au $4f$ doublet associated with gold-silicide shifts by about 860 meV from nML_{Au} to pML_{Au} . This can be related to the observed difference in the doping and a small change of the work function. The Au-Au component, on the other hand, shifts only by about 520 meV. We attribute the Au-Au bonds to Au clusters on top of the graphene layer. These clusters have an average height of a few nanometers [see Fig. 7.10 (b)]. For such nanoparticles the position of the core levels depends rather sensitively on the size of the particle [211, 212]. Thus, the shift of the Au-Au component of the Au $4f$ core level is most likely related to the size of the particular Au clusters.

As both LEED and ARPES average over a rather large area on the sample surface, we used STM to gain access to the structure of the surface on an atomic scale. The images in Fig. 7.10 (a) were measured with a room temperature scanning tunneling microscope. The SiC samples with a ZL or cML on top were transferred to the STM chamber in air.

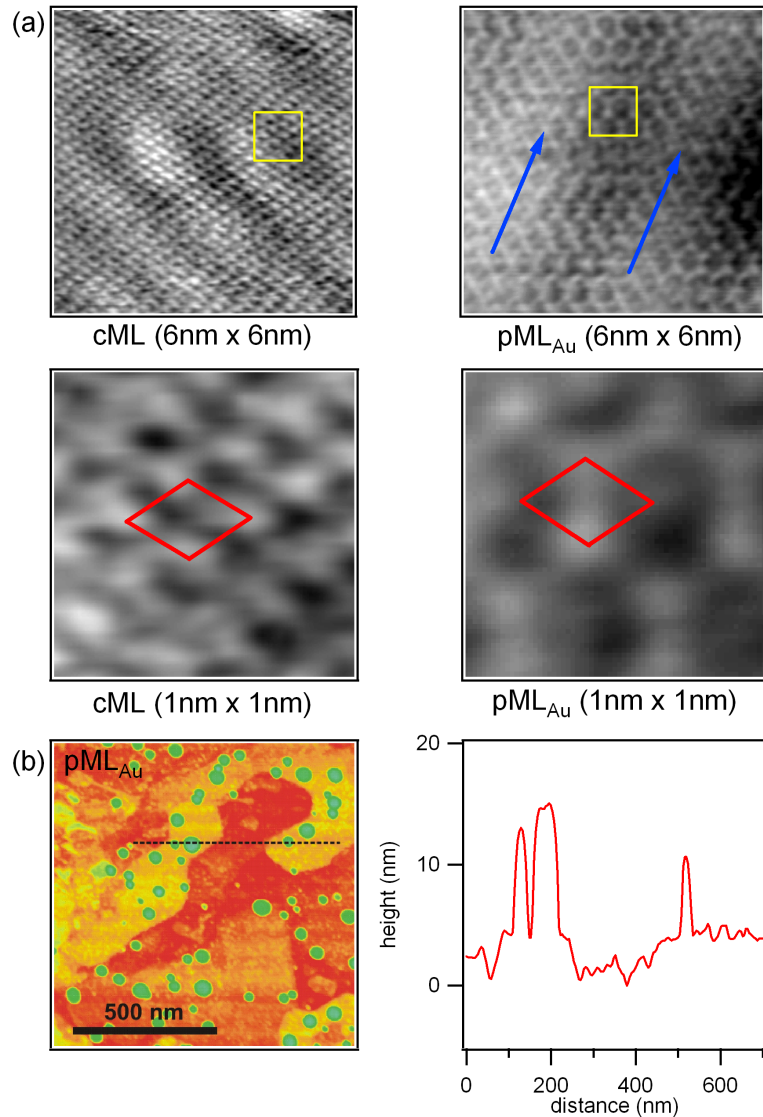


Figure 7.10: Panel (a) shows topographic STM images for the conventional graphene monolayer (left) and the p-doped graphene monolayer intercalated with Au (right). The lower panel shows a zoom-in into the regions marked by a yellow square. The red diamond indicates the graphene unit cell. The images for the conventional monolayer and p-doped monolayer were recorded at a tunneling current of 0.2 nA and a bias of -0.5 V and -0.4 V, respectively. Panel (b) shows a large scale AFM image for the p-doped graphene monolayer intercalated with Au together with a line profile extracted along the dashed line in the image. The AFM data clearly reveals the presence of Au clusters (green) on top of the graphene layer.

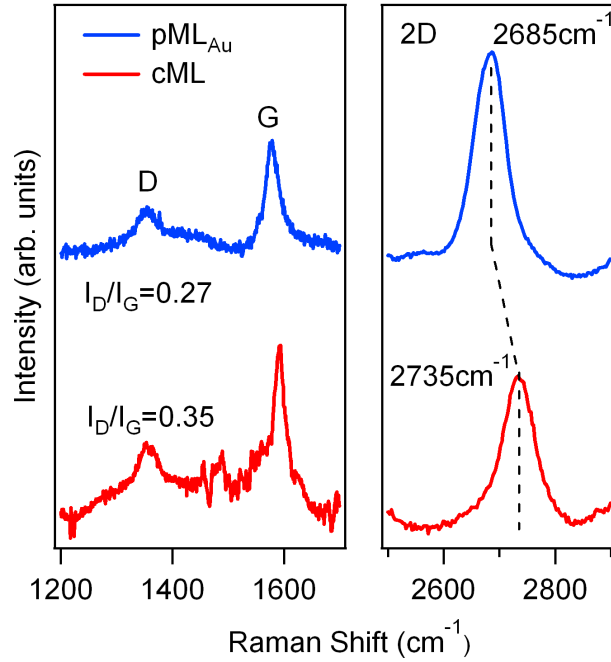


Figure 7.11: Comparison of the Raman scattering results for the conventional (red) and the p-doped (blue) graphene monolayer.

Annealing of the samples at 800°C was sufficient to remove any adsorbates from the surface. Au was deposited *in situ* from a commercial electron beam evaporator. The images for the cML and pML_{Au} were recorded at a tunneling current of 0.2 nA and a bias voltage of -0.5 V and -0.4 V , respectively. The upper panel of Fig. 7.10 (a) shows topographic images of the cML and the pML_{Au} together with a zoom-in of the area marked by a yellow square in the lower panel. The graphene unit cell is indicated by red lines. The cML shows a honeycomb lattice with a $(6\sqrt{3} \times 6\sqrt{3})R30^{\circ}$ modulation imposed by the ZL. The graphene lattice of the pML_{Au} is well ordered and shows a superstructure of parallel stripes with a width of about 3 nm as marked by blue arrows. This superstructure could be of similar origin as the one reported in [213] despite the fact that the samples in [213] were prepared by depositing Au on a cML. The change of the lattice constant of the superstructure between cML and pML_{Au} is also visible in LEED measurements in Fig. 7.8. Fig. 7.10 (b) shows a large scale $1\mu\text{m} \times 1\mu\text{m}$ AFM image for the pML_{Au} together with a line profile extracted along the dashed line in the image. The AFM data clearly reveals the presence of Au clusters (green) on top of the graphene layer. The gold clusters have a broad size distribution with a maximum height of about 15 nm.

To further investigate the degree of decoupling of the pML_{Au}, Fig. 7.11 shows Raman scattering data measured for the cML and the pML_{Au}. The Raman spectra were measured under ambient conditions using an Argon ion laser with a wavelength of 488 nm. The laser spot size was 400 nm in diameter and the laser power was 4 mW. The measured

graphene signal is rather weak and superimposed onto the signal from the SiC substrate. We subtracted the substrate contribution so that the graphene peaks become clearly visible [214]. The Raman spectra are characterized by three main graphene contributions: The G peak corresponds to an in-plane vibration of the two sublattices with respect to each other. The D and 2D peak come from a double resonance scattering process [215]. The 2D peak is always visible, whereas the D peak only appears in the presence of defects. Both G and 2D peaks shift as a function of doping [216–218] and strain [219,220]. Therefore, it is difficult to determine charge carrier concentration and strain directly from the Raman data. However, the doping induced shift is strongest for the G peak [217,218], whereas the effect of strain is more pronounced for the 2D peak [219]. If the effect of the charge carrier concentration can be determined by another procedure (in this case ARPES data), the Raman data provide useful information about strain. The Raman spectrum for the ZL (not shown here) does not show any graphene related features. The 2D peak of the pML_{Au} (blue) appears at 2685 cm⁻¹. It is red-shifted by 50 cm⁻¹ as compared to the 2D peak of the cML. As the 2D peak position is only weakly dependent on charge doping [217], we attribute the shift of the 2D peak to an increase of the lattice constant in agreement with the LEED data (see Fig. 7.9). The compressive strain present in the cML is apparently released in the pML_{Au}. This confirms the strongly reduced interactions observed in the analysis of the ARPES line width. The data in Fig. 7.11 also suggest that the D:G peak intensity ratio has decreased for the pML_{Au} (blue). As the D peak only exists in the presence of defects a reduced D:G peak intensity ratio therefore indicates an improved crystalline quality.

We have presented a new method for the epitaxial growth of decoupled graphene monolayers on the semiconducting SiC(0001) substrate. ARPES and Raman measurements reveal that the resulting slightly p-doped graphene monolayer is of higher crystalline quality than the conventionally grown graphene monolayer. The decoupling from the substrate in combination with the high crystalline quality of the pML_{Au} are expected to result in a considerable increase in carrier mobility.

7.3 Illuminating the dark corridor

ARPES measurements on graphene are characterized by the suppression of photoemission intensity on part of the Fermi surface (‘dark corridor’ [206,221,224]) due to the interference of photoelectrons emitted from the two equivalent carbon atoms per unit cell of graphene’s honeycomb lattice. The effect was verified many times in ARPES experiments using p-polarized light [62,71,74,222,223] and the presence of this dark corridor was never questioned. Unfortunately, the dark corridor effectively prevents the experimental verification of the spin rotation upon quasiparticle to photoelectron conversion in graphene predicted in [224], because of the lack of photoemission intensity in the region of interest. In this section we will show that by using s-polarized light it is possible to illuminate this dark corridor and thereby access the complete Fermi surface of graphene in an ARPES experiment. While the dark corridor has been addressed theoretically before [206,221]

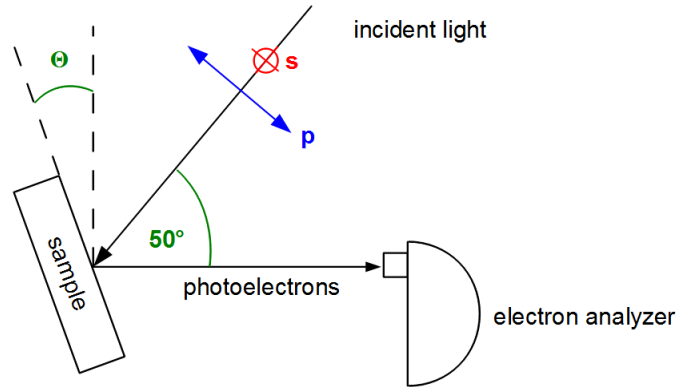


Figure 7.12: Sketch of the experimental setup: k_y corresponds to a rotation of the sample around θ . k_x is the direction perpendicular to the paper plane, it corresponds to the dispersion direction in the 2D detector. For s(p)-polarized light the electric field vector lies perpendicular to the plane of incidence (in the plane of incidence) spanned by the sample normal and the direction of incidence of the light.

the polarization dependence of the intensity modulation on the Fermi surface cannot be accounted for by the single free-electron final state used in this model. We show that this problem is overcome in our first principles photoemission calculations where we use time-reversed spin-polarized low energy electron diffraction (SPLEED) states as final states. In addition, the first-principles photoemission calculations reveal that the observed effect persists in the low photon energy regime.

A sketch of the experimental setup is displayed in Fig. 7.12. The measurements were done at the Synchrotron Radiation Center (SRC) in Stoughton, WI at the variable polarization VLS-PGM beamline. This beamline is equipped with an elliptically polarized Apple II undulator that delivers p- and s-polarization of photons in an energy range from 15 eV to 250 eV. For s(p)-polarized light the electric field vector lies perpendicular to the plane of incidence (in the plane of incidence) spanned by the sample normal and the direction of incidence of the light. In order to measure the photoemission current as a function of k_y (along the $\overline{\Gamma\text{K}}$ -direction) the sample was rotated by an angle θ (see Fig. 7.12) which was varied around $\theta_0 = 36.7^\circ$ for $h\nu = 35$ eV and around $\theta_0 = 28.7^\circ$ for $h\nu = 52$ eV. k_x (direction perpendicular to the paper plane in Fig. 7.12 corresponds to the dispersion direction in the 2D detector).

Figure 7.13 shows the measured band structure for an epitaxial graphene monolayer on SiC(0001) along the $\overline{\Gamma\text{KM}}$ -direction. The data in Fig. 7.13 was recorded at a photon energy of $h\nu = 35$ eV and $h\nu = 52$ eV with p- and s-polarized light. The gray scale is linear with black (white) corresponding to high (low) photoemission intensities. For p-polarized photons [Fig. 7.13 (a) and (c)] the intensity for one of the two branches is completely suppressed due to interference effects in the photoemission process [206, 221], only the branch dispersing upwards (towards the Fermi level) along $\overline{\Gamma\text{KM}}$ is visible in agreement with previous photoemission results [62, 71, 74, 222, 223]. For $h\nu = 35$ eV and s-polarized

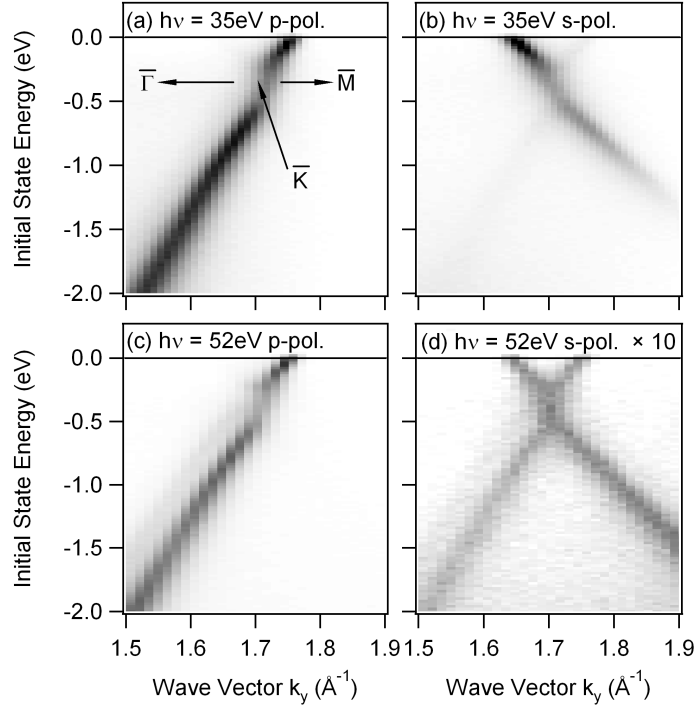


Figure 7.13: Band structure measured along $\bar{\Gamma}\bar{K}$ for an epitaxial graphene monolayer on SiC(0001) for two different photon energies (a,b: 35 eV; c,d: 52 eV) for both p- (a,c) and s-polarized (b,d) light. The gray scale is linear with black (white) corresponding to high (low) photoemission intensities.

light [Fig. 7.13 (b)] the photoemission intensity shifts to the second branch dispersing downwards (away from the Fermi level) along $\bar{\Gamma}\bar{K}\bar{M}$ that was invisible when using p-polarized light. When using s-polarized light at $h\nu = 52$ eV [Fig. 7.13 (d)] both π -bands are visible. In this case the overall intensity is reduced by about one order of magnitude as compared to the other measurements.

Figure 7.14 shows the corresponding Fermi surfaces around \bar{K} for $h\nu = 35$ eV and $h\nu = 52$ eV with both p-polarized and s-polarized light. For p-polarized radiation [Fig. 7.14 (a) and (c)] there is no photoemission intensity at spot 1 in agreement with Fig. 7.13 (a) and (c). This situation changes drastically when using s-polarized photons with $h\nu = 35$ eV in Fig. 7.14 (b). In this case, there is no photoemission intensity at the opposite side of the Fermi surface at spot 2. Changing the photon energy to $h\nu = 52$ eV leads to a homogeneous illumination of the complete Fermi surface with s-polarized light [Fig. 7.14 (d)]. As in Fig. 7.13 (d), the photocurrent is one order of magnitude lower than for p-polarized radiation. As can be seen, the dark corridor at spot 1 as introduced by Refs. [206, 221, 224] can be illuminated using s-polarized light.

The origin of the dark corridor has been explained by calculating the photoemission matrix element in dipole approximation using atomic orbitals for the initial state and a single plane wave for the final state [206]. It has been shown that the photoemission

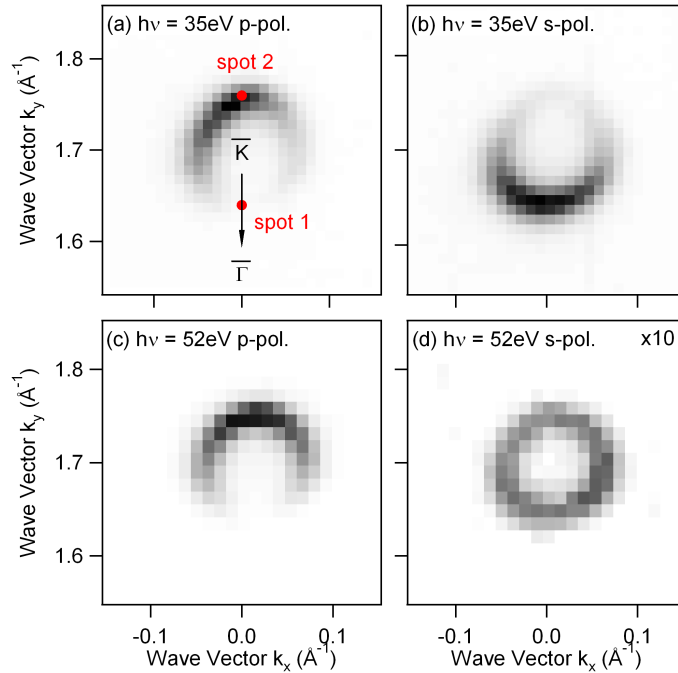


Figure 7.14: Fermi surface of epitaxial graphene on SiC(0001) measured with p-polarized light (a,c) and s-polarized light (b,d) for two different photon energies [(a,b) 35 eV; (c,d) 52 eV]. The gray scale is linear with black (white) corresponding to high (low) photoemission intensities.

intensity around \bar{K} can be separated into a polarization factor and an interference term related to the crystal structure. The interference term (see Fig. 7.15) is responsible for the suppression of the photocurrent at spot 1 at the Fermi energy. The polarization factor ($\vec{k}\hat{\lambda}$) implies that the photoemission intensity vanishes completely for $\vec{k} \perp \hat{\lambda}$, i. e. for s-polarized radiation.

However, our results show that this simple picture does not hold. For better agreement with the experimental findings we have used time-reversed spin-polarized LEED states as final states. First-principles electronic-structure calculations have been performed for a free-standing graphene layer. Many-body effects are incorporated via the complex self-energy Σ . The imaginary part of Σ is taken as 1.5 eV for the final state and as 0.01 eV for the initial state (graphene orbitals); its real part is assumed zero. Including a non-zero real part of the self-energy would shift the final states to higher energies. Furthermore, the final state in experiment is scattered by the SiC substrate, so that deviations between the theoretical and the experimental final state are possible. These deviations may include slight changes in the final state composition as well as the band dispersion. Nevertheless, trends in experiment are fully accounted for, in particular the photon energy dependence of the intensities. For a direct comparison between experiment and theory the theoretical photon energies $h\nu_{\text{th}}$ have been shifted by 8.6 eV towards higher photon energies. Figure 7.16

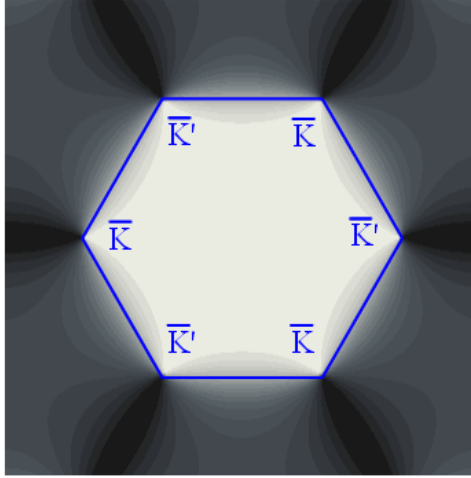


Figure 7.15: Interference term for $E > E_D$ from Ref. [206] that is responsible for the suppression of photoemission intensity on part of the Fermi surface. Black (white) corresponds to high (low) photoemission intensities.

shows the calculated Fermi surface for p-polarized and s-polarized light with $h\nu = 35$ eV and $h\nu = 52$ eV. The calculation is in good agreement with the experimental results in Fig. 7.14. The dark corridor lies at spot 1 (spot 2) for p-polarized (s-polarized $h\nu = 35$ eV) light. For s-polarized light at $h\nu = 52$ eV the Fermi surface is completely illuminated. To complete the picture, Fig. 7.16 (e) shows the intensity asymmetry between spot 1 and spot 2 defined as $A = (I_{spot1} - I_{spot2}) / (I_{spot1} + I_{spot2})$ as a function of photon energy. For $A = \pm 1$, the dark corridor lies at spot 1 or spot 2, respectively. For $A = 0$, spot 1 and spot 2 are equally illuminated, which is the case for $h\nu = 52$ eV and s-polarized light. The effect that spot 1 can be illuminated using s-polarized light persists for photon energies between $h\nu = 24$ eV and $h\nu = 52$ eV. The disappearance of the effect for $h\nu > 52$ eV is attributed to a change in the final states. Decomposing the time-reversed SPLEED final states into angular-momentum partial waves, we find that for $h\nu < 52$ eV s-like partial waves dominate the photoemission process while for $h\nu > 52$ eV the contributions from d-like partial waves dominate.

In order to compare our calculations with the results from Ref. [206], we project the time-reversed SPLEED final states onto free-electron final states. This decomposition shows that the photoemission process is dominated by up to twelve different plane waves in contrast to the single plane wave used in Ref. [206]. The weight of the different plane waves depends on the photon energy. As for the partial wave decomposition there is a transition between different plane wave contributions around $h\nu = 52$ eV. Our plane wave decomposition reveals that the plane wave $e^{i\vec{k}\vec{x}}$ used in Ref. [206] contributes at all photon energies. This explains the success of the model for p-polarized light. However, in order to explain the experimental results for s-polarized light within a tight-binding calculation, it is necessary to employ more than just one plane wave final state. The honeycomb lattice

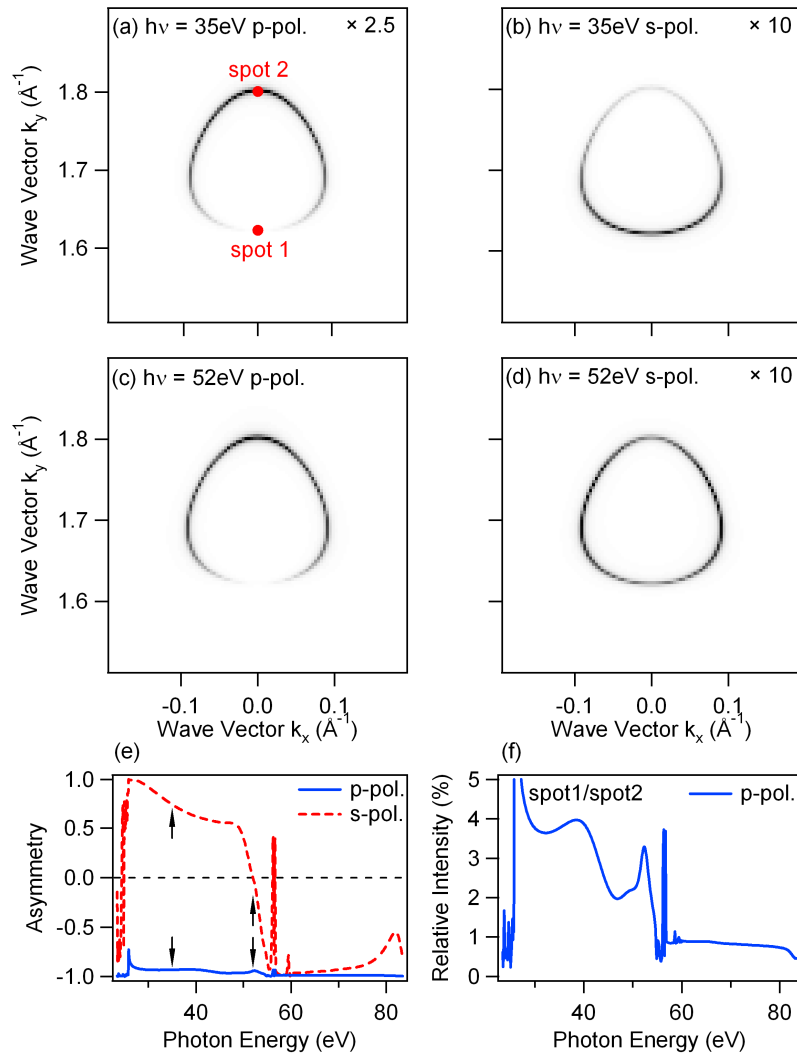


Figure 7.16: Photoemission calculations of the Fermi surfaces for p-polarized (a,c) and s-polarized (b,d) radiation for $h\nu = 35\text{ eV}$ (a,b) and $h\nu = 52\text{ eV}$ (c,d). Panel (e) shows the intensity asymmetry of spot 1 and spot 2 as a function of photon energy (blue: p-pol. light; red: s-pol. light). Panel (f) shows the intensity ratio of spot 1 compared to spot 2 for p-polarized light as a function of photon energy. The theoretical photon energies have been shifted by 8.6 eV to allow for a direct comparison with experiment.

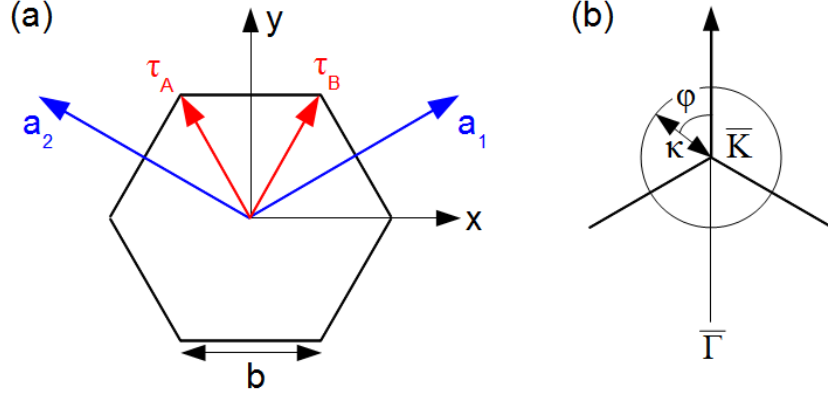


Figure 7.17: (a) Graphene lattice (black) with real space lattice vectors \vec{a}_1 and \vec{a}_2 (blue). The positions of the atoms inside the unit cell are given by $\vec{\tau}_A$ and $\vec{\tau}_B$, respectively. b is the bond length. (b) Circle around \bar{K} with radius κ . $\varphi = 0$ corresponds to the $\Gamma\bar{K}$ -direction.

of graphene is defined by the lattice vectors [Fig. 7.17 (a)]

$$\begin{aligned}\vec{a}_1 &= \frac{3}{2}b\vec{x} + \frac{\sqrt{3}}{2}b\vec{y}, \\ \vec{a}_2 &= -\frac{3}{2}b\vec{x} + \frac{\sqrt{3}}{2}b\vec{y},\end{aligned}$$

where b is the binding length, and the positions of the carbon atoms within the unit cell

$$\begin{aligned}\vec{\tau}_A &= \vec{a}_2 + b\vec{x} = -\frac{b}{2}\vec{x} + \frac{\sqrt{3}}{2}b\vec{y}, \\ \vec{\tau}_B &= \vec{a}_1 - b\vec{x} = \frac{b}{2}\vec{x} + \frac{\sqrt{3}}{2}b\vec{y}.\end{aligned}$$

The reciprocal lattice vectors are given by

$$\begin{aligned}\vec{b}_1 &= \frac{2\pi}{b} \left(\frac{1}{3}\vec{x} + \frac{1}{\sqrt{3}}\vec{y} \right), \\ \vec{b}_2 &= \frac{2\pi}{b} \left(-\frac{1}{3}\vec{x} + \frac{1}{\sqrt{3}}\vec{y} \right),\end{aligned}$$

The electronic structure of graphene close to the Dirac point can be described using a four-level Hamiltonian. The intrinsic spin-orbit coupling (SOC) of strength Δ_{SO} is modeled as $\Delta_{SO}\Psi^\dagger\sigma_z s_z\Psi$ where σ_z specifies the sublattice (pseudospin) and s_z is the spin operator (Pauli matrix). The total Hamiltonian has thus the matrix form

$$H = \begin{pmatrix} \epsilon + \Delta_{SO} & 0 & t(\vec{k}) & 0 \\ 0 & \epsilon - \Delta_{SO} & 0 & t(\vec{k}) \\ t(\vec{k})^* & 0 & \epsilon - \Delta_{SO} & 0 \\ 0 & t(\vec{k})^* & 0 & \epsilon + \Delta_{SO} \end{pmatrix},$$

where the elements are arranged as $A \uparrow, A \downarrow, B \uparrow, B \downarrow$. $t(\vec{k})$ is the matrix element for hopping from an A site to all nearest-neighbor B sites: $t(\vec{k}) = t_0 \sum_{NN} \exp(i\vec{k} \cdot \vec{r}_{NN})$. The dispersion relation is readily obtained as

$$E(\vec{k}) = \epsilon \pm \sqrt{|t(\vec{k})|^2 + \Delta_{SO}^2}.$$

In order to address photoemission, we expand the final state in plane waves

$$\phi \propto \sum_{\vec{g}} \alpha_{\vec{g}} e^{i(\vec{k}_f + \vec{g}) \cdot \vec{r}}.$$

The photocurrent is then proportional to the absolute square of the matrix element

$$M \propto \int \phi(\vec{r})^* \vec{A} \cdot \vec{p} \psi(\vec{r}) dV,$$

where ψ is an initial state, $\vec{A} \cdot \vec{p}$ is the dipole operator and \vec{A} is the field vector of the incident light. The initial state at a given \vec{k} is given by a Bloch sum of p_z -orbitals,

$$\Psi(\vec{r}) = \frac{1}{\sqrt{N}} \sum_{\vec{R}} e^{i\vec{k} \cdot \vec{R}} \sum_{X=A,B} \sum_{\sigma=\uparrow,\downarrow} c_{X\sigma}(\vec{k}) p_z(\vec{r} - \vec{r}_X - \vec{R}).$$

It is straightforward to arrive at an expression for $\vec{A} \parallel \vec{y}$ (s-polarized light) and $\vec{A} \parallel \vec{x}$ (p-polarized light ¹):

$$M_{\sigma}(\vec{A} \parallel \vec{y}) = \sum_{nm} \alpha_{nm}^* \vec{k}_{nm} \cdot \vec{A} \tilde{p}_z(\vec{k}_{nm}) (c_{A\sigma} + c_{B\sigma}) \cdot \left(e^{-i\vec{k}_{nm} \cdot \vec{r}_A} + e^{-i\vec{k}_{nm} \cdot \vec{r}_B} \right).$$

and

$$M_{\sigma}(\vec{A} \parallel \vec{x}) = \sum_{nm} \alpha_{nm}^* \vec{k}_{nm} \cdot \vec{A} \tilde{p}_z(\vec{k}_{nm}) (c_{A\sigma} - c_{B\sigma}) \cdot \left(e^{-i\vec{k}_{nm} \cdot \vec{r}_A} - e^{-i\vec{k}_{nm} \cdot \vec{r}_B} \right).$$

Here, $\vec{g} = n\vec{b}_1 + m\vec{b}_2$ and $\vec{k}_{nm} = \vec{k} + \vec{g}$. \tilde{p}_z is the Fourier-transformed initial-state p_z orbital. Note that for $\Delta_{SO} = 0$ $M_{\sigma}(\vec{A} \parallel \vec{y}) = 0$ for odd initial states ($c_{A\sigma} = -c_{B\sigma}$) and $M_{\sigma}(\vec{A} \parallel \vec{x}) = 0$ for even initial states ($c_{A\sigma} = c_{B\sigma}$), which readily explains the dark corridor and its switching from spot 1 ($\phi = 0$) to spot 2 ($\phi = \pi$) upon switching the light polarization. This is illustrated in Fig. 7.18 where the photocurrent for valence (red) and conduction band (blue) is plotted along a circle with radius κ around \bar{K} [see Fig. 7.17 (b)].

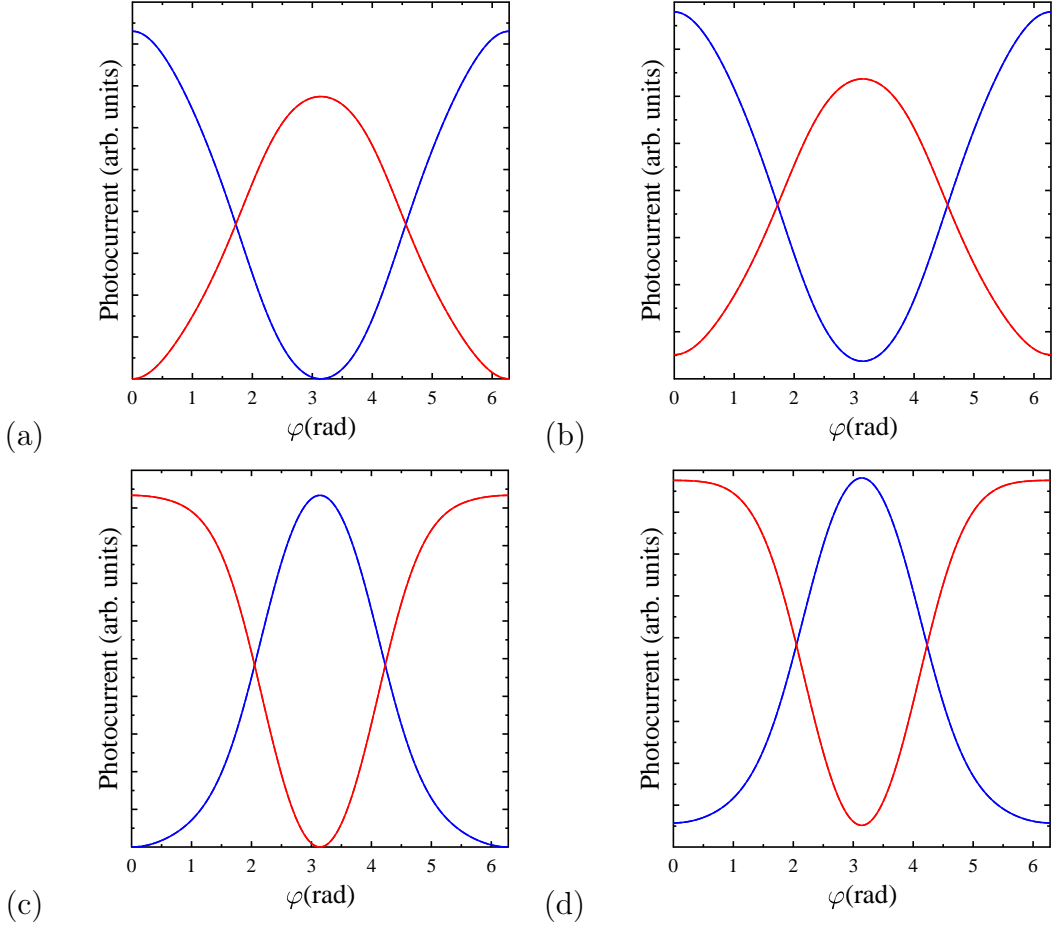


Figure 7.18: Photocurrent along a circle with radius κ around \bar{K} ($t = 1.0$, $\kappa = 0.02$) for $\vec{A} \parallel \vec{y}$ (a,b) and $\vec{A} \parallel \vec{x}$ (c,d). (a,c) without SOC; (b,d): with SOC ($\Delta_{SO} = 0.1$) The spin-up photocurrent equals the spin-down photocurrent. Note that the photocurrent vanishes for an odd initial state without SOC but remains finite with SOC. Blue: conduction band with $E = \epsilon + \sqrt{|t|^2 + \Delta_{SO}^2}$; red: valence band with $E = \epsilon - \sqrt{|t|^2 + \Delta_{SO}^2}$.

For Fig. 7.18, we have deliberately chosen $\alpha_{nm} = 1$ and the 9 plane waves with the smallest $|\vec{g}|$. The qualitative picture does not change when including even more plane waves.

For a direct comparison with the model from Ref. [206] we plot the photocurrent on a circle around \bar{K} assuming a single plane wave as final state ($n = m = 0$). The results for $\vec{A} \parallel \vec{x}$ (p-polarization) and $\vec{A} \parallel \vec{y}$ (s-polarization) are displayed in Fig. 7.19 (a) and (b), respectively. Note that the photocurrent for s-polarized light is a factor of 1×10^5 lower

¹ $\vec{A} \parallel \vec{y}$ correctly describes s-polarized light. P-polarized light, however, has two contributions $\vec{A} \parallel \vec{x}$ and $\vec{A} \parallel \vec{z}$, respectively. Their relative weight depends on the angle between the sample and the direction of the incident light. The matrix elements for $\vec{A} \parallel \vec{x}$ and $\vec{A} \parallel \vec{z}$ behave similarly. Therefore, the main idea is visualized assuming that p-polarized light is described by $\vec{A} \parallel \vec{x}$ alone. The calculations in Fig. 7.16, however, were calculated using the correct weight between $\vec{A} \parallel \vec{x}$ and $\vec{A} \parallel \vec{z}$ to describe p-polarized light.

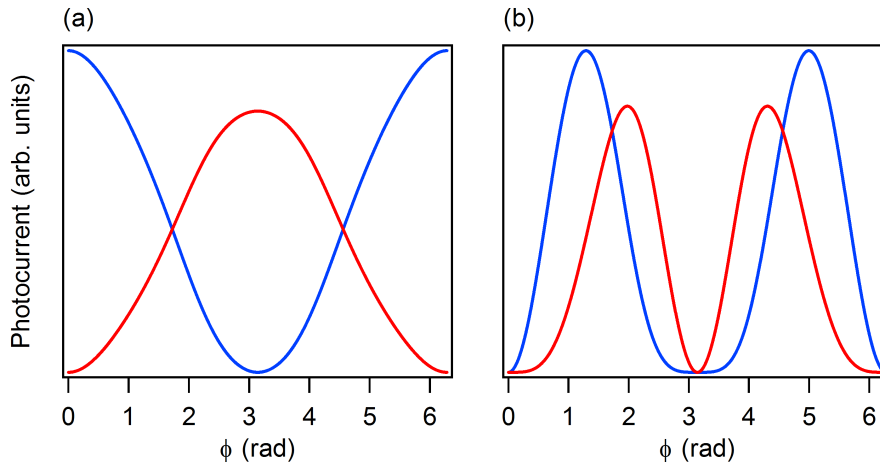


Figure 7.19: Photocurrent along a circle with radius κ around \bar{K} ($t = 1.0$, $\kappa = 0.02$) for $\vec{A} \parallel \vec{x}$ (a) and $\vec{A} \parallel \vec{y}$ (b) without SOC for the conduction band with $E = \epsilon + \sqrt{|t|^2 + \Delta_{SO}^2}$ (blue) and the valence band with $E = \epsilon - \sqrt{|t|^2 + \Delta_{SO}^2}$ (red) using a single plane wave for the final state. Note that the photocurrent for $\vec{A} \parallel \vec{y}$ is a factor of 1×10^5 lower than for $\vec{A} \parallel \vec{x}$.

than for p-polarized light. From Fig. 7.19 it is obvious that using a single plane wave for the final state allows us to describe the photocurrent for p-polarized light correctly, whereas the model fails when considering s-polarized light. Using a single plane wave for the final state leads to complete suppression of the photocurrent for s-polarized light along the $\bar{\Gamma}\bar{K}\bar{M}$ -direction (i. e. at both point 1 and point 2) and a significant reduction of the photocurrent in any other direction, which is in clear contrast to the experimental findings in Fig. 7.13 and 7.14.

Fig. 7.16 (f) shows the relative intensity of spot 1 compared to spot 2 as a function of photon energy. The photoemission intensity at spot 1 does not go to zero but remains at a few percent for p-polarized light, even though perfect AB sublattice symmetry is assumed. This is in contrast to the tight-binding calculation in Ref. [206], where perfect AB sublattice symmetry leads to zero intensity in the dark corridor. This discrepancy can be understood by including the spin-orbit interaction (SOI) in the tight-binding model. As a result, the wave function coefficients c_A and c_B of the p_z -orbitals centered at the A and B sublattice, respectively, are not equal in magnitude anymore, which leads to a nonzero photocurrent inside the dark corridor [see Fig. 7.18 (b) and (d)]. As a consequence, the degree of AB sublattice symmetry breaking cannot be deduced from the intensity inside the dark corridor as was suggested in Refs. [62, 71], unless the influence of the SOI is precisely known. Nevertheless, as the SOI in graphene is small, the same is to be expected for the corresponding photoemission intensity.

Furthermore, Ref. [224] predicts a giant spin rotation during quasiparticle to photoelectron conversion in graphene due to spin-pseudospin interference in the photoemission

process. Inside the dark corridor (at spot 1) the spin orientation of the photoelectron differs from the spin of the quasiparticle in the initial state by 180° . However, up to now this effect was believed not to be accessible in a spin-resolved ARPES measurement because of the lack of photoemission intensity inside the region of interest. Using s-polarized radiation in a spin-resolved ARPES experiment should allow for the experimental verification of the predicted spin rotation.

7.4 Conclusion

In this chapter we have addressed two important issues concerning future device application of epitaxial graphene: appropriate means for p-type doping and decoupling of the graphene layer from the substrate. First, we have shown that simple atomic p-type doping of graphene using bismuth, antimony, or gold is possible. Epitaxial graphene on silicon carbide becomes a feasible alternative to conventional electronic materials as n-type doping is naturally induced and p-type doping can be achieved by doping with gold atoms, which are easily processed.

In the second part we have shown that it is possible to decouple the graphene ZL formed on the Si-face of SiC from the substrate by Au intercalation. This new slightly p-doped graphene has an improved quality and is only weakly influenced by the underlying substrate. Our ARPES measurements for the pML_{Au} reveal a considerable reduction in line width. Our estimation for the carrier lifetime is of the same order of magnitude as the value for multilayer graphene on the C-face of SiC. Therefore, we expect a considerable increase in carrier mobility for the pML_{Au} and correspondingly the transport properties of our pML_{Au} to be closer to those for multilayer graphene on the C-face of SiC.

In the last part we have show that it is possible to illuminate the dark corridor on the measured Fermi surface of graphene using s-polarized synchrotron radiation. This effect is not included in the theoretical model from Ref. [206] that is based on a single free electron final states. Our first principles photoemission calculations use time-reversed SPLEED final states and result in good agreement with the measured Fermi surfaces. In addition, the calculations reveal that the observed effect persists in the low photon energy regime up to about $h\nu = 52$ eV. Furthermore, our findings open up a new pathway to access the giant spin rotation predicted in Ref. [224] experimentally in a spin-resolved ARPES measurement.

Chapter 8

Summary and outlook

8.1 Summary

We investigated the electronic and structural properties of different 2D electron systems — surface alloys on Ag(111), bismuth trimers on Si(111) and graphene. In the first part of this thesis we developed a better understanding about the origin of the RB-type spin splitting at surfaces by comparing the 2D band structure for the (Bi,Pb,Sb)/Ag(111) surface alloys. In addition, we determined the outward relaxation of the alloy atoms (Bi,Pb,Sb) with $I(V)$ -LEED and concluded that the large size of the spin splitting in the (Bi,Pb,Sb)/Ag(111) surface alloys has to be attributed to the interplay of the atomic spin-orbit interaction with structural parameters, especially the outward relaxation. By mixing Bi, Pb and Sb in binary and ternary surface alloys an independent tuning of the Fermi level and the Rashba energy is possible, which allows us to engineer a Fermi surface with the desired spin structure. Furthermore, we were able to transfer the concept of the giant spin splitting in surface alloys to a semiconducting substrate, which is an important step towards the application of the RB-type spin splitting in spintronics devices.

In the second part we focused on one of the few ideally 2D crystals available today — graphene. We have investigated the influence of adatom adsorption and intercalation on the linear band structure around the \bar{K} -point of the Brillouin zone. We found that both Bi and Sb atoms are able to extract electrons from the naturally n-doped graphene layer on SiC(0001). Upon Au deposition and post annealing of the sample the Dirac point is further shifted into the unoccupied states, and the graphene layer becomes a hole conductor. Subsequent experiments revealed that the gold intercalates between the graphene layer and the substrate. We have shown that the ZL can be decoupled from the substrate by Au intercalation and that — depending of the amount of intercalated Au — either a strongly n-doped or a slightly p-doped graphene layer is formed. ARPES, LEED and Raman experiments reveal that the influence of the substrate on this p-doped graphene monolayer is reduced considerably due to the Au intercalation which we expect to lead to improved electronic properties. Finally, we have shown that it is possible to illuminate the Fermi surface of graphene completely using s-polarized light with an energy of $h\nu = 52$ eV,

which was believed not to be possible according to previous theoretical models. We have extended these models by including multiple plane waves for the final state and obtained excellent agreement with measured Fermi surfaces as well as first principles calculations.

8.2 Outlook

8.2.1 Rashba effect at surfaces

Many fundamental aspects concerning the Rashba effect at surfaces have been investigated. We have gained a better understanding about the origin of the RB-type spin splitting, and different systems with an especially large spin splitting have been identified. What remains to be done now is proving the applicability of the RB-type spin splitting in these system in actual devices.

Recently, Ref. [225] has predicted that the RB-type spin splitting in the $6p$ states of a Bi adlayer on $\text{BaTiO}_3(001)$ can be manipulated by the electric polarization in the ferroelectric substrate. The relative change in the spin splitting of about 5% upon polarization reversal in the substrate turned out to be small. The total size of the spin splitting of about 0.24\AA^{-1} , however, is huge. Although the ultimate spin-electric coupling where the sign of the Rashba parameter α_R changes upon polarization reversal of the substrate was not observed for a Bi adlayer on $\text{BaTiO}_3(001)$ the idea of a RB-type spin splitting on a ferroelectric substrate opens up new pathways for spintronics devices.

In order to realize some of the device proposals that were introduced in section 2.2.3 one needs a system where all the states that cross the Fermi level are spin-polarized. Such a system was recently presented in [226]. There, the authors have shown that the electronic states of a Ge(111) surface covered with a Pb monolayer are metallic and exhibit a large Rashba spin splitting of 200 meV at the Fermi level. Due to the semiconducting Ge(111) substrate this system is ideally suited to measure the transport properties of a 2D spin-split electron system located at a surface, to build a Datta-Das spin field effect transistor or even measure the spin Hall effect.

8.2.2 Graphene

Superconductivity in graphene

The light mass of the carbon atom enhances the phonon frequency ($\omega_{ph} \propto M^{-1/2}$) which is beneficial for a high transition temperature T_c into a superconducting state. Following this idea superconducting currents have been observed in graphite intercalation compounds ($T_c = 0.55\text{ K}$ in C_8K [227], $T_c = 6.5\text{ K}$ in C_6Yb [228] and $T_c = 11.5\text{ K}$ in C_6Ca [228]), in K-doped C_{60} ($T_c = 18\text{ K}$ [229]) and in carbon nanotubes ($T_c = 20\text{ K}$ for carbon nanotubes embedded in a zeolite matrix [230] and $T_c = 12\text{ K}$ for B-doped carbon nanotubes [231]).

Graphite intercalation compounds The superconductivity in graphite intercalation compounds has been attributed to the occupation of a 2D state localized between neighbor-

ing carbon layers (interlayer state) due to charge transfer from the intercalating atoms [232]. The presence of the interlayer band and its hybridization with the π band has been related to the observed diminished normal state resistance anisotropy observed in C_6Yb [228] and indicates the significance of partially occupied 2D graphite π bands and 3D interlayer bands for superconductivity. The π bands are only weakly coupled to both the out-of-plane and the in-plane lattice vibrations of the graphene sheets. The interlayer band, however, is expected to couple to the lattice vibrations of the metal ions. Via the hybridization between the interlayer band and the graphite π band this electron-phonon coupling might be transferred to the π bands. The authors could show that in those compounds with a low transition temperature, the interlayer band remains nearly orthogonal to the π bands, whereas in C_6Yb and C_6Ca the hybridization is strong.

The authors of Ref. [233] measured the Fermi surface of C_6Ca and found that this interlayer band produces a small free-electron-like spherical Fermi surface at the $\bar{\Gamma}$ point in addition to the Fermi surface derived from the π band of graphene centered around the \bar{K} point. When cooling the sample below T_c a superconducting gap opens up in the vicinity of the $\bar{\Gamma}$ point, whereas the gap is small (or absent) around \bar{K} . Energy distribution curves measured at normal emission show a drop in intensity at 80 meV which corresponds to the energy of out-of-plane vibrations of the carbon atoms. Apparently, the interlayer band strongly couples to the out-of-plane phonons of the graphene layer, which is expected to be responsible for the observed superconductivity. This suggests a conventional electron-phonon coupling mediated pairing mechanism in graphite intercalation compounds.

Fullerenes Ref. [234] investigated why the electron-phonon interaction is much larger in doped Fullerenes than in doped graphite. Due to their non-planar geometry the orbitals near the Fermi energy in Fullerenes have a significant σ admixture in contrast to graphite where the Fermi surface is formed by pure π bands. The highest lying C_{60} phonon modes involve C-C bond-stretching. As the C-C σ bonds are much stronger than the π bonds they couple more strongly to the C-C bond-stretching phonons. This results in a comparatively high T_c in Fullerenes as compared to graphite.

Carbon nanotubes Before the discovery of intrinsic superconductivity in carbon nanotubes [230] the authors of Ref. [235] have shown that it is possible to induce superconductivity in carbon nanotubes via superconducting contacts. The critical field in isolated single-walled carbon nanotubes was found to be 10 times larger than the measured critical field of the superconducting contact. Furthermore, the product of the normal state resistance R_N and the critical current i_c at $T = 0$ K was found to be a factor of 40 larger than expected assuming that the superconducting gap in the nanotube is of the same size like in the superconducting contacts. The authors concluded that their data could be explained by the existence of superconducting fluctuations intrinsic to single-walled carbon nanotubes. They suggested that the coupling of the electrons to the fundamental bending mode of the suspended nanotube can drive the system towards a superconducting phase which is then stabilized by the superconductivity of the contacts.

Ref. [230] reported the observation of a superconducting state in single-walled small-diameter carbon nanotubes embedded in a zeolite matrix. They argued that the superconducting state is favored locally at $T < 20$ K. However, due to the strong correlations in the 1D system there is always some probability that fluctuations would locally drive the superconducting state to the normal state so that zero resistance can only be achieved at $T = 0$ K. Nevertheless, between $T = 0$ and $T = T_c$ the superconductivity is not totally destroyed but can manifest superconducting behavior which is strongly modified by fluctuation effects [230].

Similar to Fullerenes the curvature of a carbon nanotube resulting from a small diameter is known to increase T_c due to a strong electron-phonon coupling between the σ bonds and the radial breathing mode of the nanotube [231]. An additional increase in T_c is expected if the Fermi level is aligned with a van Hove singularity in the density of states. This situation can be achieved in B-doped carbon nanotubes when 1.5% to 2% of the carbon atoms are replaced with B atoms, resulting in a T_c of 12 K [231].

Superconductivity in graphene After examining the origin of superconductivity in graphene related materials we have to consider in which way the proposed mechanisms might apply to graphene itself. The coupling of the π bands to the breathing mode of the graphene lattice is weak. σ admixture due to a non-planar geometry of the graphene sheet is expected to result in a stronger electron-phonon coupling in analogy to Fullerenes and carbon nanotubes [231, 234]. Similar to the graphite intercalation compounds epitaxial graphene grown on different substrates can be intercalated by (earth) alkali atoms which might result in superconductivity. Furthermore, a high density of states at the Fermi level enhances the electron-phonon coupling. Therefore, aligning the Fermi level with a van Hove singularity in the density of states of the graphene band structure by chemical doping or gating is also expected to enhance T_c similar to Ref. [231]

Using the proximity effect it has been shown that graphene can indeed support supercurrents [236]. Recently, it has been demonstrated that the extended van Hove singularity at the \bar{M} point of the 2D graphene Brillouin zone can be shifted to the Fermi level by chemical doping which results in an attractive electron-electron coupling that is supposed to drive the system to a superconducting instability [237].

Apart from these experimental investigations several theoretical predictions for a superconducting state in graphene have been made. Ref. [238] predict two pairing states for graphene, a conventional s wave channel and a more exotic $p_x + ip_y$ phase. At half filling, the $p + ip$ phase is gapless and superconductivity is a hidden order. When the Fermi level is shifted away from the Dirac point by chemical doping or gating the $p_x + ip_y$ pairing might lead to superconductivity in graphene.

The interplay of the relativistic dispersion with interactions at half filling in graphene is expected to lead to a quantum phase transition between a semimetallic state at low interaction strengths and a Mott insulating state at high interaction strengths. In the intermediate regime a gapped, non-magnetic phase exists which is characterized by local correlations that correspond to a resonating valencebond state, as proposed in the context of high

temperature superconductivity [239]. The absence of superconductivity in free-standing graphene could be due to the vanishing density of states at the Fermi energy. Therefore, it would be interesting to investigate the influence of doping. A further enhancement of correlation effects can be expected by increasing graphene's lattice constant [239].

Recently, Ref. [240] suggested that p-doped fully hydrogenated graphene (graphane) is an electron-phonon superconductor with a critical temperature of $T_c \approx 90$ K, i.e. above the boiling point of liquid nitrogen.

In order to find a new mechanism for superconductivity in graphene a comparison with the structurally and electronically related MgB_2 ($T_c = 39$ K which is the highest T_c observed for a non-copper-oxide bulk superconductor [241, 242]) might be helpful. Graphene forms the same planar sp^2 -bonded structure like the B atoms in MgB_2 . Furthermore, MgB_2 and graphene are isoelectronic, and the light masses of both MgB_2 and C enhance the phonon frequency. Superconductivity in MgB_2 was attributed to hole doping of the covalent σ bands through the ionic, layered character of MgB_2 and the 2D character of the σ bands resulting in a large density of states at the Fermi level. Furthermore, the coupling of the σ band to the bond-stretching mode in MgB_2 is likely to be responsible for the experimentally observed T_c of 39 K [241].

The major difference between MgB_2 and graphene lies in the position of the σ band. In MgB_2 the σ band crosses the Fermi level because the layer of Mg^{2+} ions lowers the non-bonding B π bands relative to the bonding σ bands causing $\sigma \rightarrow \pi$ charge transfer and a σ band doping of 0.13 holes per unit cell [241]. In graphene, however, the σ bands are completely occupied. In order to transfer the MgB_2 -type superconductivity to graphene one has to significantly lower the unoccupied π bands to allow for $\sigma \rightarrow \pi$ charge transfer and hole doping of the σ bands.

We made a first step in this direction and intercalated Mg atoms below a graphene monolayer grown on SiC(0001). The Mg atoms donate their valence electrons to the graphene sheet, which becomes strongly n-doped. The resulting band structure is shown in Fig. 8.1. Whether this doping level is sufficient to induce $\sigma \rightarrow \pi$ charge transfer and hole doping of the σ bands remains unclear from the present preliminary data. This question can be answered by measuring the Fermi surface of Mg intercalated graphene over the whole Brillouin zone. Should it turn out that the n-type doping due to Mg intercalation is not sufficient, additional n-type doping can be achieved by depositing (earth) alkali atoms also on top of the graphene layer in analogy to Ref. [237].

Spin-orbit interaction in graphene

Due to the light mass of carbon atoms ($Z = 6$) the influence of the SOI on the band structure of graphene is considered to be negligible. In combination with the low hyperfine interaction of the electron spins with the carbon nuclei long spin lifetimes are expected and graphene might also be a promising material for the realization of spin q-bits. However, the measured spin relaxation length between 1.5 and $2\mu\text{m}$ at room temperature turned out to be unexpectedly short hinting towards a much stronger influence of the SOI [243]. It is known that the nonzero curvature and thickness of carbon nanotubes increases the SOI [244],

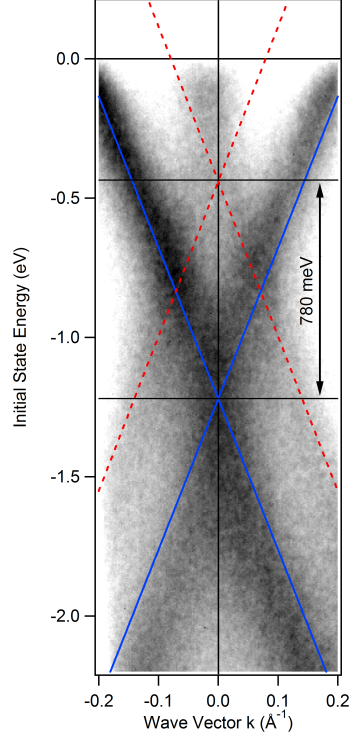


Figure 8.1: Epitaxial graphene monolayer on SiC(0001) with Mg intercalated. The Mg atoms donate their valence electrons to the graphene sheet and induce strong n-type doping. Blue lines are guides to the eye. The red dashed line indicates the position of the π bands for pristine graphene on SiC(0001).

and recently, a zero-field splitting of $\Delta_{SO} = 0.37$ meV was measured. Furthermore, sp^3 distortions of the graphene lattice induced by an impurity are expected to increase the spin-orbit coupling in graphene [245]. The RB splitting of 13 meV recently measured in graphene/Au/Ni(111) has been attributed to the intercalated Au and its high nuclear charge [44]. Recent first-principles calculations predict that the combination of buckling and an external electric field increases the SOI induced band gap at \bar{K} by two orders of magnitude resulting in a band gap of 40 meV for 5% buckling and an external field of $1\text{V}/\text{\AA}$ [246].

The electronic band structure of graphene in the vicinity of the Dirac point in the presence of the intrinsic spin-orbit coupling Δ_{SO} and RB-type SOI λ_R caused by a perpendicular electric field is given by [247–250]:

$$E(k) = \mu\lambda_R + \nu\sqrt{(\hbar v_F k)^2 + (\lambda_R - \mu\Delta_{SO})^2} \quad (8.1)$$

where $\nu = 1$ for the electron band, $\nu = -1$ for the hole band, and $\mu = \pm 1$. Current estimates for the size of the intrinsic SOI Δ_{SO} (0.1 meV [247,248], $0.5\mu\text{eV}$ [250], $12\mu\text{eV}$ [249]) and a Rashba-type SOI λ_R [1, 2] ($0.04\mu\text{eV}$ [247, 248], $11\mu\text{eV}$ [250]) in graphene are small and therefore the effect of the SOI is considered negligible. Figure 8.2 (a) shows the band

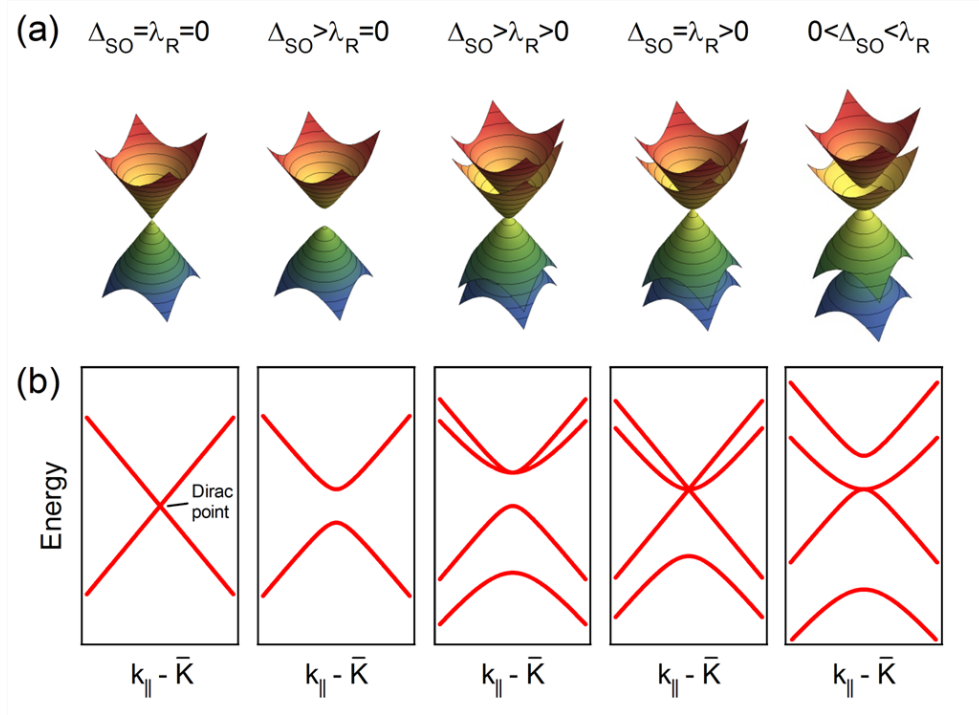


Figure 8.2: Spin-orbit interaction in graphene: Panels (a) and (b) show the band structure of graphene around the \bar{K} point of the surface Brillouin zone as a function of the intrinsic SOI Δ_{SO} and a Rashba-type SOI λ_R . For $\Delta_{SO} > \lambda_R$ a band gap between valence and conduction band opens up. For $\lambda_R > 0$ the linear π -bands become spin polarized.

structure around \bar{K} together with a 2D cut in panel (b) for two equivalent carbon atoms in the graphene unit cell. For $\Delta_{SO} > \lambda_R$ a small band gap ($E_G = 2(\Delta_{SO} - \lambda_R)$) between valence and conduction band opens. If $\lambda_R > 0$ the spin-degeneracy of the bands is lifted. Because the present theoretical models are isotropic around \bar{K} a constant energy contour below the Dirac point consists of two concentric circles where the spins rotate clockwise on the outer contour and counter-clockwise on the inner contour. In addition, the spin splitting remains finite in the limit $k \rightarrow \bar{K}$ because the \bar{K} point is not a time-reversal invariant momentum in the 2D Brillouin zone. In contrast to a conventional parabolic dispersion, where the energy separation between the spin-split bands increases linearly with momentum, this splitting is given by $2\lambda_R$ far away from the Dirac point [249] independent of momentum in the case of graphene's linear π -bands.

Although the effects of the intrinsic SOI in graphene are small, the presence of buckling, strain, defects or adsorbates is predicted to enhance the SOI. First experimental results indicate that the SOI in graphene might be larger than expected [44, 245] and further investigations in this direction are clearly desirable. Furthermore, the presence of the substrate breaks the inversion symmetry of an epitaxial graphene layer which is expected to result in a small RB-type spin splitting. The ideal tool to investigate such a small spin splitting is spin-resolved ARPES, where the spin of the emitted photoelectron is measured

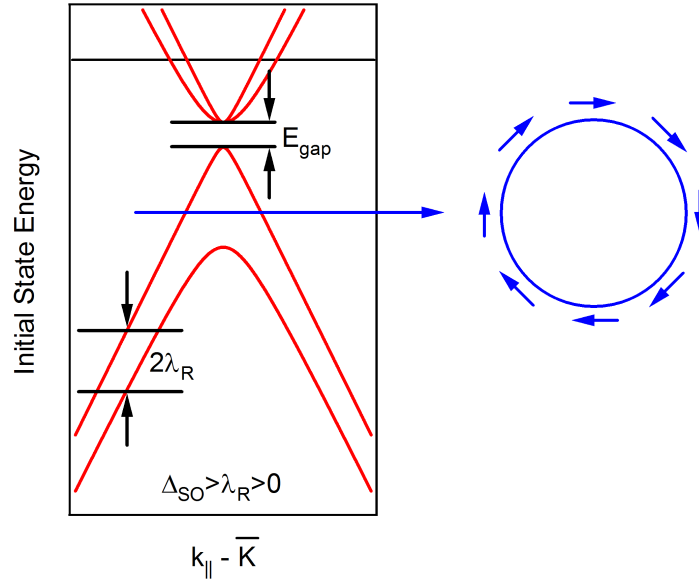


Figure 8.3: If $\lambda_R > \Delta_{SO} > 0$ a constant energy contour just below the Dirac point in graphene looks similar to the Fermi surface of a topological insulator.

in addition to its momentum and energy. In analogy to the measurements performed for graphene/Au/Ni(111) [44] we expect a similar spin splitting for gold-intercalated graphene on SiC(0001) (see section 7.2).

Majorana fermions

In this section we will argue that the combination of superconductivity and RB-type spin-orbit coupling in graphene allows for the existence of Majorana fermions.

The Dirac equation describes spin 1/2 particles, where positive/negative eigenvalues correspond to particles/antiparticles. Majorana disliked the negative eigenvalues of the Dirac equation for reasons of mathematical elegance and modified the Dirac equation to allow for positive eigenvalues only [251]. Interestingly, these ‘Majorana fermions’ are their own antiparticles. They obey non-Abelian exchange statistics and their discovery might — one day — enable fault-tolerant quantum computing [252].

The existence of such Majorana particles in solid state systems is intimately linked to the fields of superconductivity and topological insulators. A topological insulator is characterized by a bulk band gap and the presence of topological surface (or edge) states. The Fermi surface of a topological insulator consists of an odd number of 2D (1D) spin-polarized states between time-reversal invariant points of the Brillouin zone [253]. If only a single spin-polarized 2D (1D) state crosses the Fermi level, backscattering of the charge carriers is forbidden and they become insensitive to scattering by impurities [254]. Furthermore, the special spin topology of the Fermi surface in these systems allows for dissipationless spin

currents [255], and in combination with superconductivity such a spin topology allows for the existence of Majorana fermions. Consequently, Majorana fermions are believed to exist in topological superconductors (spin triplet $p_x + ip_y$ superconductors) [256], in topological insulators where superconductivity is induced by the proximity effect with a conventional singlet s -wave superconductor [252], or even for a conventional parabolic dispersion with RB-type SOI in contact with an s -wave superconductor when the spin-degeneracy at the $\bar{\Gamma}$ -point is lifted by an additional magnetic field [257, 258].

Both topological insulators as well as graphene are characterized by a Dirac type linear dispersion in the vicinity of the Fermi level. The only difference is that in graphene the Dirac cone is generally assumed to be spin-degenerate. In the presence of a RB-type SOI λ_R , however, the spin-degeneracy is lifted. In that case, the constant energy contour just below the Dirac point looks very similar to that of a topological insulator (see Fig. 8.3). Considering epitaxial graphene on SiC(0001) with a spin splitting of $2\lambda_R \approx 13$ meV one has to shift the Fermi level into the desired region just below the Dirac point by chemical doping and to induce superconductivity e.g. via the proximity effect [236]. Then, the graphene layer should fulfill the necessary preconditions in order to host Majorana fermions. These Majorana fermions could then be detected as a zero energy peak in the density of states via scanning tunneling spectroscopy.

Bibliography

- [1] Y. A. Bychkov, and E. I. Rashba *JETP Lett.* **39**, 78 (1984)
- [2] Y. A. Bychkov, and E. I. Rashba *J. Phys. C: Solid State Phys.* **17**, 6039 (1984)
- [3] D. Pacilé, C. R. Ast, M. Papagno, C. Da Silva, L. Moreschini, M. Falub, A. P. Seitsonen, and M. Grioni *Phys. Rev. B* **73**, 245429 (2006)
- [4] C. R. Ast, G. Wittich, P. Wahl, R. Vogelgesang, D. Pacilé, M. C. Falub, L. Moreschini, M. Papagno, M. Grioni, and K. Kern *Phys. Rev. B* **75**, 201401(R) (2007)
- [5] C. R. Ast, J. Henk, A. Ernst, L. Moreschini, M. C. Falub, D. Pacilé, P. Bruno, K. Kern, and M. Grioni *Phys. Rev. Lett.* **98**, 186807 (2007)
- [6] C. R. Ast, D. Pacilé, L. Moreschini, M. C. Falub, M. Papagno, K. Kern, and M. Grioni *Phys. Rev. B* **77**, 081407(R) (2008)
- [7] F. Meier, V. Petrov, S. Guerrero, C. Mudry, L. Patthey, J. Osterwalder, and J. H. Dil *Phys. Rev. B* **79**, 241408 (2009)
- [8] K. S. Novoselov, A. K. Geim, S. V. Morozov, D. Jiang, Y. Zhang, S. V. Dubonos, I. V. Grigorieva, A. A. Firsov *Science* **306**, 666 (2004)
- [9] A. J. Van Bommel, J. E. Crombeen, and A. Van Tooren *Surf. Sci.* **48**, 463 (1975)
- [10] C. Berger, Z. Song, T. Li, X. Li, A. Y. Ogbazghi, R. Feng, Z. Dai, A. N. Marchenkov, E. H. Conrad, P. N. First, and W. A. de Heer *J. Phys. Chem. B* **108**, 19912 (2004)
- [11] K. V. Emtsev, F. Speck, T. Seyller, L. Ley, and J. D. Riley *Phys. Rev. B* **77**, 155303 (2008)
- [12] J. A. Robinson, M. Wetherington, J. L. Tedesco, P. M. Campbell, X. Weng, J. Stitt, M. A. Fanton, E. Frantz, D. Snyder, B. L. VanMil, G. G. Jernigan, R. L. Myers-Ward, C. R. Eddy, and D. K. Gaskill *Nano Lett.* **9**, 2873 (2009)
- [13] M. Sprinkle, M. Ruan, Y. Hu, J. Hakinson, M. Rubio-Roy, B. Zhang, X. Wu, C. Berger, and W. A. de Heer *Nature Nanotech.* **5**, 727 (2010)
- [14] C. Kittel (2002) *Einführung in die Festkörperphysik* (Wien: Oldenburg)

- [15] I. Tamm *Z. Physik* **76**, 849 (1939)
- [16] W. Shockley *Phys. Rev.* **56**, 317 (1939)
- [17] K. Oura, V. G. Lifshits, A. A. Saranin, A. V. Zotov, and M. Katayama *Surface Science An Introduction* (Springer Berlin Heidelberg New York Hong Kong London Milan Paris Tokyo)
- [18] P. R. Wallace *Phys. Rev.* **71**, 622 (1947)
- [19] G. W. Semenoff *Phys. Rev. Lett.* **53**, 2449 (1984)
- [20] A. K. Geim, and K. S. Novoselov *Nature Mater.* **6**, 183 (2007)
- [21] M. V. Berry *Proc. R. Soc. Lond. A* **392**, 45 (1984)
- [22] T. Ando *J. Phys. Soc. Jpn.* **67**, 1704 (1998)
- [23] K. Y. Bliokh *Phys. Lett. A* **344**, 127 (2005)
- [24] S. V. Morozov, K. S. Novoselov, M. I. Katsnelson, F. Schedin, L. A. Ponomarenko, D. Jiang, and A. K. Geim *Phys. Rev. Lett.* **97**, 016801 (2006)
- [25] X. Wu, X. Li, Z. Song, C. Berger, and W. A. de Heer *Phys. Rev. Lett.* **98**, 136801 (2007)
- [26] I. Brihuega, P. Mallet, C. Bena, S. Bose, C. Michaelis, L. Vitali, F. Varchon, L. Magaud, K. Kern, and J. Y. Veuillen *Phys. Rev. Lett.* **101**, 206802 (2008)
- [27] K. S. Novoselov, A. K. Geim, S. V. Morozov, D. Jiang, M. I. Katsnelson, I. V. Grigorieva, S. V. Dubonos, and A. A. Firsov *Nature* **438**, 197 (2005)
- [28] Y. Zhang, Y.-W. Tan, H. L. Stormer, and P. Kim *Nature* **438**, 201 (2005)
- [29] X. Wu, Y. Hu, M. Ruan, N. K. Madiomanana, J. Hankinson, M. Sprinkle, C. Berger, and W. A. de Heer *Appl. Phys. Lett.* **95**, 223108 (2009)
- [30] M. I. Katsnelson, K. S. Novoselov, and A. K. Geim *Nature Phys.* **2**, 620 (2006)
- [31] P. San-Jose, E. Prada, E. McCann, and H. Schomerus *Phys. Rev. Lett.* **102**, 247204 (2009)
- [32] A. K. Geim *Science* **324**, 1530 (2009)
- [33] K. A. Mkhoyan, A. W. Contryman, J. Silcox, D. A. Stewart, G. Eda, C. Mattevi, S. Miller, and M. Chhowalla *Nano Lett.* **9**, 1058 (2009)
- [34] C. Gómez-Navarro, J. C. Meyer, R. S. Sundaram, A. Chuvilin, S. Kurasch, M. Burghard, K. Kern, and U. Kaiser *Nano Lett.* **10**, 1144 (2010)

-
- [35] C. F. McConville, D. P. Woodruff, and S. D. Kevan *Surf. Sci.* **171**, L447 (1986)
- [36] L. Papagno, M. Conti, L.S. Caputi, J. Anderson, and G.J. Lapeyre *Surf. Sci.* **219**, L565 (1989)
- [37] T. Aizawa, R. Souda, Y. Ishizawa, H. Hirano, T. Yamada, and K. Tanaka *Surf. Sci.* **237**, 194 (1990)
- [38] A. Nagashima, N. Tejima, and C. Oshima *Phys. Rev. B* **50**, 17487 (1994)
- [39] A. M. Shikin, D. Farías, and K. H. Rieder *Europhys. Lett.* **44**, 44 (1998)
- [40] A.M. Shikin, D. Farías, V.K. Adamchuk, and K.-H. Rieder *Surf. Sci.* **424**, 155 (1999)
- [41] D. Farías, A. M. Shikin, K.-H. Rieder, and Y. S. Dedkov *J. Phys.: Condens. Matter* **11**, 8453 (1999)
- [42] A. M. Shikin, G. V. Prudnikova, V. K. Adamchuk, F. Moresco, and K.-H. Rieder *Phys. Rev. B* **62**, 13202 (2000)
- [43] Y. S. Dedkov, A. M. Shikin, V. K. Adamchuk, S. L. Molodtsov, C. Laubschat, A. Bauer, and G. Kaindl *Phys. Rev. B* **64**, 035405 (2001)
- [44] A. Varykhalov, J. Sánchez-Barriga, A. M. Shikin, C. Biswas, E. Vescovo, A. Rybkin, D. Marchenko and O. Rader *Phys. Rev. Lett.* **101**, 157601 (2008)
- [45] K. S. Kim, Y. Zhao, H. Jang, S. Y. Lee, J. M. Kim, K. S. Kim, J.-H. Ahn, P. Kim, J.-Y. Choi, and B. H. Hong *Nature* **457**, 706 (2009)
- [46] N. A. Kholin, E. V. Rut'kov, and A. Y. Tontegode *Surf. Sci.* **139**, 155 (1984)
- [47] E. V. Rut'kov, and A. Y. Tontegode *Surf. Si.* **161**, 373 (1985)
- [48] I. Pletikosić, M. Kralj, P. Pervan, R. Brako, J. Coraux, A. T. N'Diaye, C. Busse, and T. Michely *Phys. Rev. Lett.* **102**, 056808 (2009)
- [49] A. B. Preobrajenski, M. L. Ng, A. S. Vinogradov, and N. Mårtensson *Phys. Rev. B* **78**, 073401 (2008)
- [50] H. Zi-pu, D.F. Ogletree, M.A. van Hove, and G.A. Somorjai *Surf. Sci.* **180**, 433 (1987)
- [51] T. Aizawa, Y. Hwang, W. Hayami, R. Souda, S. Otani, and Y. Ishizawa *Surf. Sci.* **260**, 311 (1992)
- [52] T. A. Land, T. Michely, R. J. Behm, J. C. Hemminger, and G. Comsa *Surf. Sci.* **264**, 261 (1992)
- [53] M. Sasaki, Y. Yamada, Y. Ogiwara, S. Yagyu, and S. Yamamoto *Phys. Rev. B* **61**, 15653 (2000)

- [54] X. Li, W. Cai, J. An, S. Kim, J. Nah, D. Yang, R. Piner, A. Velamakanni, I. Jung, E. Tutuc, S. K. Banerjee, L. Colombo, and R. S. Ruoff *Science* **324**, 1312 (2009)
- [55] S. Bae, H. Kim, Y. Lee, X. Xu, J.-S. Park, Y. Zheng, J. Balakrishnan, T. Lei, H. R. Kim, Y. I. Song, Y.-J. Kim, K. S. Kim, B. Özyilmaz, J.-H. Ahn, B. H. Hong, and S. Iijima *Nature Nanotech.* **5**, 574 (2010)
- [56] T. Aizawa, R. Souda, S. Otani, Y. Ishizawa, and C. Oshima *Phys. Rev. Lett.* **64**, 768 (1990)
- [57] T. Aizawa, R. Souda, S. Otani, Y. Ishizawa, and C. Oshima *Phys. Rev. B* **42**, 11469 (1990)
- [58] H. Itoh, T. Ichinose, C. Oshima, T. Ichinokawa, and T. Aizawa *Surf. Sci.* **254**, L437 (1991)
- [59] Y. Hwang, T. Aizawa, W. Hayami, S. Otani, Y. Ishizawa, and S.-J. Park *Surf. Sci.* **271**, 299 (1992)
- [60] A. Ismach, C. Druzgalski, S. Penwell, A. Schwartzberg, M. Zheng, A. Javey, J. Bokor, and Y. Zhang *Nano Lett.* **10**, 1542 (2010)
- [61] F. Varchon, R. Feng, J. Hass, X. Li, B. Ngoc Nguyen, C. Naud, P. Mallet, J.-Y. Veullen, C. Berger, E. H. Conrad, and L. Magaud *Phys. Rev. Lett.* **99**, 126805 (2007)
- [62] T. Seyller, A. Bostwick, K. V. Emtsev, K. Horn, L. Ley, J. L. McChesney, T. Ohta, J. D. Riley, E. Rotenberg, and F. Speck *Phys. Stat. Sol. B* **245**, 1436 (2008)
- [63] M. Orlita, C. Faugeras, P. Plochocka, P. Neugebauer, G. Martinez, D. K. Maude, A.-L. Barra, M. Sprinkle, C. Berger, W. A. de Heer, and M. Potemski *Phys. Rev. Lett.* **101**, 267601 (2008)
- [64] M. Sprinkle, D. Siegel, Y. Hu, J. Hicks, A. Tejada, A. Taleb-Ibrahimi, P. Le Fèvre, F. Bertran, S. Vizzini, H. Enriquez, S. Chiang, P. Soukiassian, C. Berger, W. A. de Heer, A. Lanzara, and E. H. Conrad *Phys. Rev. Lett.* **103**, 226803 (2009)
- [65] J. Jobst, D. Waldmann, F. Speck, R. Hirner, D. K. Maude, T. Seyller, and H. B. Weber *Phys. Rev. B* **81**, 195434 (2010)
- [66] F. Owman, C. Hallin, P. Mårtensson, and E. Janzén *J. of Cryst. Growth* **167**, 391 (1996)
- [67] V. Ramachandran, M.F. Brady, A.R. Smith, R.M. Feenstra, and D.W. Greve *J. Elec. Mater.* **27**, 308 (1998)
- [68] S. Soubatch, S. E. Sadow, S. P. Rao, W. Y. Lee, M. Konuma, and U. Starke *Mater. Sci. Forum* **483-485**, 761 (2005)

-
- [69] C. L. Frewin, C. Coletti, C. Riedl, U. Starke, and S. E. Sadow *Mater. Sci. Forum* **615-617**, 589 (2009)
- [70] I. Forbeaux, J.-M. Themlin, and J.-M. Debever *Phys. Rev. B* **58**, 16 396 (1998)
- [71] A. Bostwick, T. Ohta, J. L. McChesney, K. V. Emtsev, T. Seyller, K. Horn, and E. Rotenberg *New J. Phys.* **9**, 385 (2007)
- [72] C. Riedl, U. Starke, J. Bernhardt, M. Franke, and K. Heinz *Phys. Rev. B.* **76**, 245406 (2007)
- [73] P. Mallet, F. Varchon, C. Naud, L. Magaud, C. Berger, and J.-Y. Veillen *Phys. Rev. B* **76**, 041403(R) (2007)
- [74] A. Bostwick, T. Ohta, T. Seyller, K. Horn, and E. Rotenberg *Nature Phys.* **3**, 36 (2007)
- [75] T. Ohta, A. Bostwick, T. Seyller, K. Horn, and E. Rotenberg *Science* **313**, 951 (2006)
- [76] S. Y. Zhou, G.-H. Gweon, A. V. Fedorov, P. N. First, W. A. de Heer, D.-H. Lee, F. Guinea, A. H. Castro Neto, and A. Lanzara *Nature Mater.* **6**, 770 (2007)
- [77] C. Riedl, C. Coletti, T. Iwasaki, A. A. Zakharov, and U. Starke *Phys. Rev. Lett.* **103**, 246804 (2009)
- [78] E. Rotenberg, A. Bostwick, T. Ohta, J. L. McChesney, T. Seyller, and K. Horn *Nature Mater.* **7**, 258 (2007)
- [79] S.Y. Zhou, D.A. Siegel, A.V. Fedorov, F. El Gabaly, A. K. Schmid, A.H. Castro Neto, D.-H. Lee, and A. Lanzara *Nature Mater.* **7**, 259 (2007)
- [80] S. Kim, J. Ihm, H. J. Choi, and Y.-W. Son *Phys. Rev. Lett.* **100**, 176802 (2008)
- [81] K. V. Emtsev, A. Bostwick, K. Horn, J. Jobst, G. L. Kellogg, L. Ley, J. L. McChesney, T. Ohta, S. A. Reshanov, J. Röhrl, E. Rotenberg, A. K. Schmid, D. Waldmann, H. B. Weber, and T. Seyller *Nature Mater.* **8**, 203 (2009)
- [82] T. Mayer-Kuckuk (1997) *Atomphysik* (B. G. Teubner Stuttgart)
- [83] R. Winkler (2003) *Spin-Orbit Coupling Effects in Two-Dimensional Electron and Hole Systems* ed J. Kühn, Th. Müller, A. Ruckenstein, F. Steiner, J. Trümper, P. Wölfle (Springer Berlin Heidelberg New York Hong Kong London Milan Paris Tokyo)
- [84] G. Dresselhaus *Phys. Rev.* **100**(2), 580 (1955)
- [85] L. Petersen, and P. Hedegård *Surf. Sci.* **459**, 49 (2000)
- [86] S. Datta, and B. Das *Appl. Phys. Lett.* **56**, 665 (1990)

- [87] J. Ohe, M. Yamamoto, T. Ohtsuki, and J. Nitta *Phys. Rev. B* **72**, 041308(R) (2005)
- [88] J. Sinova, D. Culcer, Q. Niu, N. A. Sinitsyn, T. Jungwirth, and A. H. MacDonald *Phys. Rev. Lett.* **92**, 126603 (2004)
- [89] J. Wunderlich, B. Kaestner, J. Sinova, and T. Jungwirth *Phys. Rev. Lett.* **94**, 047204 (2005)
- [90] E. Cappelluti, C. Grimaldi, and F. Marsiglio *Phys. Rev. Lett.* **98**, 167002 (2007)
- [91] E. I. Rashba *Phys. Rev. B* **68**, 241315(R) (2003)
- [92] M. König, S. Wiedmann, C. Brüne, A. Roth, H. Buhmann, L. W. Molenkamp, X.-L. Qi, and S.-C. Zhang *Science* **318**, 766 (2007)
- [93] S. LaShell, B. A. McDougall, and E. Jensen *Phys. Rev. Lett.* **77**, 3419 (1996)
- [94] F. Reinert, G. Nicolay, S. Schmidt, D. Ehm, and S. Hufner *Phys. Rev. B* **63**, 115415 (2001)
- [95] Y. M. Koroteev, G. Bihlmayer, J. E. Gayone, E. V. Chulkov, S. Blügel, P. M. Echenique, and P. Hofmann *Phys. Rev. Lett.* **93**, 046403 (2004)
- [96] K. Sugawara, T. Sato, S. Souma, T. Takahashi, M. Arai, and T. Sasaki *Phys. Rev. Lett.* **96**, 046411 (2006)
- [97] E. Rotenberg, J. W. Chung, and S. D. Kevan *Phys. Rev. Lett.* **82**, 4066 (1999)
- [98] G. Bihlmayer, Y. M. Koroteev, P. M. Echenique, E. V. Chulkov, and S. Blügel *Surf. Sci.* **600**, 3888 (2006)
- [99] F. Forster, S. Hufner, and F. Reinert *J. Phys. Chem. B* **108**, 14692 (2004)
- [100] F. Forster, A. Bendounan, F. Reinert, V. G. Grigoryan, and M. Springborg *Surf. Sci.* **601**, 5595 (2007)
- [101] O. Krupin, G. Bihlmayer, K. Starke, S. Gorovikov, J. E. Prieto, K. Döbrich, S. Blügel, and G. Kaindl *Phys. Rev. B* **71**, 201403 (2005)
- [102] H. Cercellier, Y. Fagot-Revurat, B. Kierren, F. Reinert, D. Popović, and D. Malterre *Phys. Rev. B* **70**, 193412 (2004)
- [103] D. Popović, F. Reinert, S. Hufner, V. G. Grigoryan, M. Springborg, H. Cercellier, Y. Fagot-Revurat, B. Kierren, and D. Malterre *Phys. Rev. B* **72**, 045419 (2005)
- [104] H. Cercellier, C. Didiot, Y. Fagot-Revurat, B. Kierren, L. Moreau, and D. Malterre *Phys. Rev. B* **73**, 195413 (2006)

-
- [105] L. Moreschini, A. Bendounan, C. R. Ast, F. Reinert, M. Falub, and M. Grioni *Phys. Rev. B* **77**, 115407 (2008)
- [106] H. Bentmann, F. Forster, G. Bihlmayer, E. V. Chulkov, L. Moreschini, M. Grioni, and F. Reinert *Eur. Phys. Lett.* **87**, 37003 (2009)
- [107] F. Meier, V. Petrov, H. Mirhosseini, L. Patthey, J. Henk, J. Osterwalder, and J. H. Dil, arXiv:1001.4927 (2010)
- [108] L. Moreschini, A. Bendounan, H. Bentmann, M. Assig, K. Kern, F. Reinert, J. Henk, C. R. Ast, and M. Grioni *Phys. Rev. B* **80**, 135438 (2009)
- [109] G. Bihlmayer, S. Blügel, and E. V. Chulkov *Phys. Rev. B* **75**, 195414 (2007)
- [110] F. Meier, H. Dil, J. Lobo-Checa, L. Patthey, and J. Osterwalder *Phys. Rev. B* **77**, 165431 (2008)
- [111] J. Premper, M. Trautmann, J. Henk, and P. Bruno *Phys. Rev. B* **76**, 073310 (2007)
- [112] T. Hirahara, T. Nagao, I. Matsuda, G. Bihlmayer, E. V. Chulkov, Y. M. Koroteev, P. M. Echenique, M. Saito, and S. Hasegawa *Phys. Rev. Lett.* **97**, 146803 (2006)
- [113] T. Hirahara, T. Nagao, I. Matsuda, G. Bihlmayer, E. V. Chulkov, Y. M. Koroteev, and S. Hasegawa *Phys. Rev. B* **75**, 035422 (2007)
- [114] T. Hirahara, K. Miyamoto, I. Matsuda, T. Kadono, A. Kimura, T. Nagao, G. Bihlmayer, E. V. Chulkov, S. Qiao, K. Shimada, H. Namatame, M. Taniguchi, and S. Hasegawa *Phys. Rev. B* **76**, 153305 (2007)
- [115] T. Hirahara, K. Miyamoto, A. Kimura, Y. Niinuma, G. Bihlmayer, E. V. Chulkov, T. Nagao, I. Matsuda, S. Qiao, K. Shimada, H. Namatame, M. Taniguchi, and S. Hasegawa *New J. Phys.* **10**, 083038 (2008)
- [116] Y. M. Koroteev, G. Bihlmayer, E. V. Chulkov, and S. Blügel *Phys. Rev. B* **77**, 045428 (2008)
- [117] J. H. Dil, F. Meier, J. Lobo-Checa, L. Patthey, G. Bihlmayer, and J. Osterwalder *Phys. Rev. Lett.* **101**, 266802 (2008)
- [118] T. Hirahara, T. Komorida, A. Sato, G. Bihlmayer, E. V. Chulkov, K. He, I. Matsuda, and S. Hasegawa *Phys. Rev. B* **78**, 035408 (2008)
- [119] K. He, T. Hirahara, T. Okuda, S. Hasegawa, A. Kabizaki, and I. Matsuda *Phys. Rev. Lett.* **101**, 107604 (2008)
- [120] E. Frantzeskakis, S. Pons, H. Mirhosseini, J. Henk, C. R. Ast, and M. Grioni *Phys. Rev. Lett.* **101**, 196805 (2008)

- [121] K. Sakamoto, T. Oda, A. Kimura, K. Miyamoto, M. Tsujikawa, A. Imai, N. Ueno, H. Namatame, M. Taniguchi, P. E. J. Eriksson, and R. I. G. Uhrberg *Phys. Rev. Lett.* **102**, 096805 (2009)
- [122] K. J. Wan, T. Guo, W. K. Ford, and J. C. Hermanson *Surf. Sci.* **261**, 69 (1992)
- [123] T. Kinoshita, S. Kono, and H. Nagayoshi *J. Phys. Soc. Jpn.* **56**, 2511 (1987)
- [124] Y. Kim, J.-S. Kim, C.-C. Hwang, S. P. Shrestha, K.-S. An, and C.-Y. Park *J. Korean Phys. Soc.* **39**, 1032 (2001)
- [125] F. Reinert *J. Phys.: Condens. Matter* **15**, S693 (2003)
- [126] A. M. Shikin, A. Varykhalov, G. V. Prudnikova, D. Usachov, V. K. Adamchuk, Y. Yamada, J. D. Riley, and O. Rader *Phys. Rev. Lett.* **100**, 057601 (2008)
- [127] H. Hertz *Ann. Phys.* **31**, 983 (1887)
- [128] A. Einstein *Ann. Phys.* **17**, 132 (1905)
- [129] S. Huefner (2003) *Photoelectron Spectroscopy — Principles and Applications* (Springer Berlin Heidelberg New York)
- [130] M. P. Seah, and W. A. Dench *Surf. Interface Anal.* **1**, 2 (1979)
- [131] N. W. Ashcroft, and N. D. Mermin (2003) *Solid State Physics* (USA)
- [132] G. Grimvall (1981) *The Electron-Phonon Interaction in Metals, Selected Topics in Solid State Physics* ed E. Wohlfarth (New York: North-Holland)
- [133] J. H. Dil *J. Phys.: Condens. Matter* **21**, 403001 (2009)
- [134] J. F. Moulder, W. F. Stickle, P. E. Sobol, and K. D. Bomben (1995) *Handbook of X-ray Photoelectron Spectroscopy* ed J. Chastain and R. C. King Jr. (Physical Electronics, Inc., Minnesota, USA)
- [135] W. Nolting (2004) *Grundkurs Theoretische Physik 5/2: Quantenmechanik — Methoden und Anwendungen* (Springer Berlin Heidelberg New York)
- [136] J. B. Pendry *J. Phys. C: Solid St. Phys.* **13**, 937 (1980)
- [137] A. Barbieri and M. A. Van Hove, Symmetrized Automated Tensor LEED package, available from M. A. Van Hove
- [138] A. Barbieri and M. A. Van Hove, private communication
- [139] G. Kresse, and J. Furthmüller, *Phys. Rev. B* **54**, 11169 (1996)

-
- [140] J. Henk in *Handbook of Thin Film Materials* **2**, 479 (2002)(Academic Press, ed. H. S. Nalwa)
- [141] J. Zabloudil, R. Hammerling, L. Szunyogh, and P. Weinberger *Electron Scattering in Solid Matter* Springer (2005)
- [142] J. P. Perdew, and Y. Wang *Phys. Rev. B* **45**, 13244 (1992)
- [143] J. Braun *Rep. Prog. Phys.* **59**, 1267 (1996)
- [144] P. D. Quinn, D. Brown, D. P. Woodruff, P. Bailey, and T. C. Q. Noakes *Surf. Sci.* **511**, 43 (2002)
- [145] D. P. Woodruff, and J. Robinson *Appl. Surf. Sci.* **219**, 1 (2003)
- [146] I. Gierz, B. Stadtmüller, J. Vuorinen, M. Lindroos, F. Meier, J. H. Dil, K. Kern, and C. R. Ast *Phys. Rev. B* **81**, 245430 (2010)
- [147] J. Henk, M. Hoesch, J. Osterwalder, A. Ernst, and P. Bruno *J. Phys.: Condens. Matter* **16**, 7581 (2004)
- [148] K. Wittel, and R. Manne *Theoret. Chim. Acta.* **33**, 347 (1974)
- [149] S. A. de Vries, W. J. Huisman, P. Goettkindt, M. J. Zwanenburg, S. L. Bennett, I. K. Robinson, and E. Vlieg *Surf. Sci.* **414**, 159 (1998)
- [150] E. A. Soares, C. Bittencourt, V. B. Nascimento, V. E. de Carvalho, C. M. C. de Castilho, C. F. McConville, A. V. de Carvalho, and D. P. Woodruff *Phys. Rev. B* **61**, 13983 (2000)
- [151] J. Henk, A. Ernst, and P. Bruno *Phys. Rev. B* **68**, 165416 (2003)
- [152] D. Huertas-Hernando, F. Guinea, and A. Brataas *Phys. Rev. B* **74**, 155426 (2006)
- [153] D. Hsieh, Y. Xia, L. Wray, D. Qian, A. Pal, J. H. Dil, J. Osterwalder, F. Meier, G. Bihlmayer, C. L. Kane, Y. S. Hor, R. J. Cava, and M. Z. Hasan *Science* **323**, 919 (2009)
- [154] C. E. Moore *Atomic Energy Levels* Natl. Bur. Stand. (U.S.) Circ. No. 467 (U.S. GPO, Washington, D.C.,1949, 1952), Vols. II & III
- [155] Y. Liu, and R. E. Allen *Phys. Rev. B* **52**, 1566 (1995) and references therein
- [156] C. R. Ast, and H. Höchst *Phys. Rev. Lett.* **87**, 177602 (2001)
- [157] J.-S. Jeong, and H.-W. Lee *Phys. Rev. B* **80**, 075409 (2009)

- [158] L. Moreschini, A. Bendounan, I. Gierz, C. R. Ast, H. Mirhosseini, H. Höchst, K. Kern, J. Henk, A. Ernst, S. Ostanin, F. Reinert, and M. Grioni *Phys. Rev. B* **79** 075424 (2009)
- [159] D. P. Woodruff, and J. Robinson *J. Phys.: Condens. Matter* **12**, 7699 (2000)
- [160] J. Dalmas, H. Oughaddou, C. Léandri, J.-M. Gay, G. Le Lay, G. Tréglia, B. Aufray, O. Bunk, and R. L. Johnson *Phys. Rev. B* **72**, 155424 (2005)
- [161] D. Kaminski, P. Poodt, E. Aret, N. Radenovic, and E. Vlieg *Surf. Sci.* **575**, 233 (2005)
- [162] P. Bailey, T. C. Q. Noakes, and D. P. Woodruff *Surf. Sci.* **426**, 358 (1999)
- [163] H. Mirhosseini, J. Henk, A. Ernst, S. Ostanin, C.-T. Chiang, P. Yu, A. Winkelmann, and J. Kirschner *Phys. Rev. B* **79**, 245428 (2009)
- [164] H. Mirhosseini, A. Ernst, S. Ostanin, and J. Henk *J. Phys.: Condens. Matter* **22**, 385501 (2010)
- [165] I. Gierz, F. Meier, J. H. Dil, K. Kern, and C. R. Ast arXiv:1011.1829v1 (2010)
- [166] B. A. Bernevig, S.-C. Zhang, *Phys. Rev. Lett.* **95**, 016801 (2005)
- [167] R. H. Miwa, T. M. Schmidt, and G. P. Srivastava *J. Phys.: Condens. Matter* **15**, 2441 (2003)
- [168] R. Shioda, A. Kawazu, A. A. Baski, C. F. Quate, and J. Nogami, *Phys. Rev. B* **48**, 4895 (1993)
- [169] I. Gierz, T. Suzuki, E. Frantzeskakis, S. Pons, S. Ostanin, A. Ernst, J. Henk, M. Grioni, K. Kern, and C. R. Ast *Phys. Rev. Lett.* **103**, 046803 (2009)
- [170] J. Nitta, T. Akazaki, H. Takayanagi, and T. Enoki, *Phys. Rev. Lett.* **78**, 1335 (1997)
- [171] M. Schultz, F. Heinrichs, U. Merkt, T. Colin, T. Skauli, and S. Løvold *Semicond. Sci. Technol.* **11**, 1168 (1996)
- [172] X. C. Zhang, A. Pfeuffer-Jeschke, K. Ortner, V. Hock, H. Buhmann, C. R. Becker, and G. Landwehr *Phys. Rev. B* **63**, 245305 (2001)
- [173] K. Sakamoto, H. Kakuta, K. Sugawara, K. Miyamoto, A. Kimura, T. Kuzumaki, N. Ueno, E. Annese, J. Fujii, A. Kodama, T. Shishidou, H. Namatame, M. Taniguchi, T. Sato, T. Takahashi, and T. Oguchi *Phys. Rev. Lett.* **103**, 156801 (2009)
- [174] A. Mugarza, A. Mascaraque, V. Repain, S. Rousset, K. N. Altmann, F. J. Himpsel, Y. M. Koroteev, E. V. Chulkov, F. J. García de Abajo, and J. E. Ortega *Phys. Rev. B* **66**, 245419 (2002)

-
- [175] J. Lobo-Checa, F. Meier, J. H. Dil, T. Okuda, M. Corso, V. N. Petrov, M. Hengsberger, L. Patthey, and J. Osterwalder *Phys. Rev. Lett.* **104**, 187602 (2010)
- [176] F. Kuemmeth, S. Ilani, D. C. Ralph, and P. L. McEuen *Nature* **452**, 448 (2008)
- [177] F. Herman, and S. Skillman *Atomic Structure Calculations* (Prentice-Hall, Englewood Cliffs, NJ, 1983)
- [178] S. Mathias, A. Ruffing, F. Deicke, M. Wiesenmayer, I. Sakar, G. Bihlmayer, E. V. Chulkov, Y. M. Koroteev, P. M. Echenique, M. Bauer, and M. Aeschlimann *Phys. Rev. Lett.* **104**, 066802 (2010)
- [179] W. A. de Heer, C. Berger, X. Wu, P. N. First, E. H. Conrad, X. Li, T. Li, M. Sprinkle, J. Hass, M. L. Sadowski, M. Potemski, and G. Martinez *Solid State Commun.* **143**, 92 (2007)
- [180] Y.-W. Son, M. L. Cohen, and S. G. Louie *Nature* **444**, 347 (2006)
- [181] Y. Zhang, T.-T. Tang, C. Girit, Z. Hao, M. C. Martin, A. Zettl, M. F. Crommie, Y. R. Shen, and F. Wang *Nature* **459**, 820 (2009)
- [182] L. Ci, L. Song, C. Jin, D. Jariwala, D. Wu, Y. Li, A. Srivastava, Z. F. Wang, K. Storr, L. Balicas, F. Liu, and P. M. Ajayan *Nature Mater.* **9**, 430 (2010)
- [183] R. Balog, B. Jørgensen, L. Nilsson, M. Andersen, E. Rienks, M. Bianchi, M. Fanetti, E. Lægsgaard, A. Baraldi, S. Lizzit, Z. Sljivancanin, F. Besenbacher, B. Hammer, T. G. Pedersen, P. Hofmann, and L. Hornekær *Nature Mater.* **9**, 315 (2010)
- [184] Z. Wei, D. Wang, S. Kim, S.-Y. Kim, Y. Hu, M. K. Yakes, A. R. Laracuente, Z. Dai, S. R. Marder, C. Berger, W. P. King, W. A. de Heer, P. E. Sheehan, and E. Riedo *Science* **328**, 1373 (2010)
- [185] L. Jiao, L. Zhang, X. Wang, G. Diankov, and H. Dai *Nature* **458**, 877 (2009)
- [186] J. B. Oostinga, H. B. Heersche, X. Liu, A. F. Morpurgo, and L. M. K. Vandersypen *Nature Mater.* **7**, 151 (2008)
- [187] J. Kedzierski, P.-L. Hsu, P. Healey, P. W. Wyatt, C. L. Keast, M. Sprinkle, C. Berger, and W. A. de Heer *IEEE Trans. Electron Devices* **55**, 2078 (2008)
- [188] G. Gu, S. Nie, W. J. Feenstra, R. P. Devaty, and W. J. Choyke *Appl. Phys. Lett.* **90**, 253507 (2007)
- [189] F. Maier, B. Riedel, J. Mantel, and J. Ristein *Phys. Rev. Lett.* **85**, 3472 (2000)
- [190] V. Chakrapani, J. C. Angus, A. B. Anderson, S. D. Wolter, B. R. Stoner, and G. U. Sumanasekera *Science* **318**, 1424 (2007)

- [191] J. Ristein *Science* **313**, 1057 (2006)
- [192] S. J. Sque, R. Jones, and P. R. Briddon *Phys. Stat. Sol. (a)* **204**, 3078 (2007)
- [193] W. Chen, S. Chen, D. C. Qui, X. Y. Gao, and A. T. S. Wee *J. Am. Chem. Soc.* **129**, 10419 (2007)
- [194] E. H. Hwang, S. Adam, and S. Das Sarma *Phys. Rev. B* **76**, 195421 (2007)
- [195] T. O. Wehling, K. S. Novoselov, S. V. Morozov, E. E. Vdovin, M. I. Katsnelson, A. K. Geim, and A. I. Lichtenstein *Nano Lett.* **8**, 173 (2008)
- [196] S. Y. Zhou, D. A. Siegel, A. V. Fedorov, and A. Lanzara *Phys. Rev. Lett.* **101**, 086402 (2008)
- [197] J. Blochwitz, M. Pfeiffer, T. Fritz, and K. Leo *Appl. Phys. Lett.* **73**, 729 (1998)
- [198] X. Zhou, M. Pfeiffer, J. Blochwitz, A. Werner, A. Nollau, T. Fritz, and K. Leo *Appl. Phys. Lett.* **78**, 410 (2001)
- [199] E. J. H. Lee, K. Balasubramanian, R. T. Weitz, M. Burghard, and K. Kern *Nature Nanotech.* **3**, 486 (2008)
- [200] G. Giovannetti, P. A. Khomyakov, G. Brocks, V. M. Karpan, J. van der Brink, and P. J. Kelly *Phys. Rev. Lett.* **101**, 026803 (2008)
- [201] K. T. Chan, J. B. Neaton, and M. L. Cohen *Phys. Rev. B* **77**, 235430 (2008)
- [202] P. W. Sutter, J.-I. Flege, and E. A. Sutter *Nature Mater.* **7**, 406 (2008)
- [203] C. Berger, Z. Song, X. Li, X. Wu, N. Brown, C. Naud, D. Mayou, T. Li, J. Hass, A. N. Marchenkov, E. H. Conrad, P. N. First, and W. A. de Heer *Science* **312**, 1191 (2006)
- [204] E. Rotenberg, A. Bostwick, T. Ohta, J. L. McChesney, T. Seyller, and K. Horn *Nature Mater.* **7**, 258 (2008)
- [205] S. Y. Zhou, D. A. Siegel, A. V. Fedorov, F. El Gabaly, A. K. Schmid, A. H. Castro Neto, D.-H. Lee, and A. Lanzara *Nature Mater.* **7**, 259 (2008)
- [206] E. L. Shirley, L. J. Terminello, A. Santoni, and F. J. Himpsel *Phys. Rev. B* **51**, 13614 (1995)
- [207] I. Gierz, C. Riedl, U. Starke, C. R. Ast, and K. Kern *Nano Lett.* **8**, 4603 (2008)
- [208] C. Riedl, A. A. Zakharov, and U. Starke *Appl. Phys. Lett.* **93**, 033106 (2008)
- [209] C. Virojanadara, and L. I. Johansson, *Surf. Sci.* **600**, 436 (2006)

-
- [210] D. Stoltz, S. E. Stoltz, and L. S. O. Johansson, *J. Phys. Condens. Matter* **19**, 266006 (2007)
- [211] H.-G. Boyen, A. Ethirajan, G. Kästle, F. Weigl, P. Ziemann, G. Schmid, M. G. Garnier, M. Büttner, and P. Oelhafen *Phys. Rev. Lett.* **94**, 016804 (2005)
- [212] P. Torelli, L. Giordano, S. Benedetti, P. Luches, E. Annese, S. Valeri, and G. Paccioni *J. Phys. Chem. C* **113**, 19957 (2009)
- [213] B. Premlal, M. Cranney, F. Vonau, D. Aubel, D. Casterman, M. M. De Souza, and L. Simon *Appl. Phys. Lett.* **94**, 263115 (2009)
- [214] D. S. Lee, C. Riedl, B. Krauss, K. von Klitzing, U. Starke, and J. H. Smet *Nano Lett.* **8**, 4320 (2008)
- [215] S. Reich, and C. Thomsen *Phil. Trans. R. Soc. Lond. A* **362**, 2271 (2004)
- [216] S. Pisana, M. Lazzeri, C. Casiraghi, K. S. Novoselov, A. K. Geim, A. C. Ferrari, and F. Mauri *Nature Mater.* **6**, 198 (2007)
- [217] J. Yan, Y. B. Zhang, P. Kim, and A. Pinczuk *Phys. Rev. Lett.* **98**, 166802 (2007)
- [218] C. Stampfer, F. Molitor, D. Graf, K. Ensslin, A. Jungen, C. Hierold, and L. Wirtz *Appl. Phys. Lett.* **91**, 241907 (2007)
- [219] M. Huang, H. Yan, C. Chen, D. Song, T. F. Heinz, and J. Hone *PNAS* **106**, 7304 (2009)
- [220] Z. H. Ni, H. M. Wang, Y. Ma, J. Kasim, Y. H. Wu, and Z. X. Shen *ACS Nano* **2**, 1033 (2008)
- [221] H. Daimon, S. Imada, H. Nishimoto, and S. Suga *J. Electron. Spectrosc. Relat. Phenom.* **76**, 487 (1995)
- [222] M. Mucha-Kruczyński, O. Tsypliyatyev, A. Grishin, E. McCann, V. I. Falko, A. Bostwick, and E. Rotenberg *Phys. Rev. B* **77**, 195403 (2008)
- [223] I. Gierz, T. Suzuki, R. T. Weitz, D. S. Lee, B. Krauss, C. Riedl, U. Starke, H. Höchst, J. H. Smet, C. R. Ast, and K. Kern *Phys. Rev. B* **81**, 235408 (2010)
- [224] F. Kuemmeth, and E. I. Rashba *Phys. Rev. B* **80**, 241409(R) (2009)
- [225] H. Mirhosseini, I. V. Maznichenko, S. Abdelouahed, S. Ostanin, A. Ernst, I. Mertig, and J. Henk *Phys. Rev. B* **81**, 073406 (2010)
- [226] K. Yaji, Y. Ohtsubo, S. Hatta, H. Okuyama, K. Miyamoto, T. Okuda, A. Kimura, H. Namatame, M. Taniguchi, and T. Aruga *Nat. Commun.* 1:17 doi:10.1038/ncomms1016 (2010)

- [227] N. B. Hannay, T. H. Geballe, B. T. Matthias, K. Andres, P. Schmidt, and D. MacNair *Phys. Rev. Lett.* **14**, 225 (1965)
- [228] T. E. Weller, M. Ellerby, S. S. Saxena, R. P. Smith, and N. T. Skipper *Nature Phys.* **1**, 39 (2005)
- [229] A. F. Hebard, M. J. Rosseinsky, R. C. Haddon, D. W. Murphy, S. H. Glarum, T. T. M. Palstra, A. P. Ramirez, and A. R. Kortan *Nature* **350**, 600 (1991)
- [230] Z. K. Tang, L. Zhang, N. Wang, X. X. Zhang, G. H. Wen, G. D. Li, J. N. Wang, C. T. Chan, and P. Sheng *Science* **292**, 2462 (2001)
- [231] N. Murata, J. Haruyama, J. Reppert, A. M. Rao, T. Koretsune, S. Saito, M. Matsu-daira, and Y. Yagi *Phys. Rev. Lett.* **101**, 027002 (2008)
- [232] G. Csányi, P. B. Littlewood, A. H. Nevidomskyy, C. J. Pickard, and B. D. Simons *Nature Phys.* **1**, 42 (2005)
- [233] K. Sugawara, T. Sato, and T. Takahashi *Nature Phys.* **5**, 40 (2009)
- [234] C. M. Varma, J. Zaanen, and K. Raghavachari *Science* **254**, 989 (1991)
- [235] A. Y. Kasumov, R. Deblock, M. Kociak, B. Reulet, H. Bouchiat, I. I. Khodos, Yu. B. Gorbatov, V. T. Volkov, C. Journet, and M. Burghard *Science* **284**, 1508 (1999)
- [236] H. B. Heersche, P. Jarillo-Herrero, J. B. Oostinga, L. M. K. Vandersypen, and A. F. Morpurgo *Nature* **446**, 56 (2007)
- [237] J. L. McChesney, A. Bostwick, T. Ohta, T. Seyller, K. Horn, J. González, and E. Rotenberg *Phys. Rev. Lett.* **104**, 136803 (2010)
- [238] B. Uchoa, and A. H. Castro Neto *Phys. Rev. Lett.* **98**, 146801 (2007)
- [239] Z. Y. Meng, T. C. Lang, S. Wessel, F. F. Assaad, and A. Muramatsu *Nature* **464**, 847 (2010)
- [240] G. Savini, A. C. Ferrari, and F. Giustino *Phys. Rev. Lett.* **105**, 037002 (2010)
- [241] J. M. An, and W. E. Pickett *Phys. Rev. Lett.* **86**, 4366 (2001)
- [242] J. Nagamatsu, N. Nakagawa, T. Muranaka, Y. Zenitani, and J. Akimitsu *Nature* **410**, 63 (2001)
- [243] N. Tombros, C. Jozsa, M. Popinciuc, H. T. Jonkman, and B. J. van Wees *Nature* **448**, 571 (2007)
- [244] T. Ando *J. Phys. Soc. Jpn.* **69**, 1757 (2000)
- [245] A. H. Castro Neto, and F. Guinea *Phys. Rev. Lett.* **103**, 026804 (2009)

- [246] S. Abdelouahed, A. Ernst, J. Henk, I. V. Maznichenko, and I. Mertig *Phys. Rev. B* **82**, 125424 (2010)
- [247] C. L. Kane, and E. J. Mele *Phys. Rev. Lett.* **95**, 146802 (2005)
- [248] C. L. Kane, and E. J. Mele *Phys. Rev. Lett.* **95**, 226801 (2005)
- [249] M. Gmitra, S. Konschuh, C. Ertler, C. Ambrosch-Draxl, and J. Fabian *Phys. Rev. B* **80**, 235431 (2009)
- [250] H. Min, J. E. Hill, N. A. Sinitsyn, B. R. Sahu, L. Kleinman, and A. H. MacDonald *Phys. Rev. B* **74**, 165310 (2006)
- [251] E. Majorana *Nuovo Cimento* **5**, 171 (1937)
- [252] L. Fu, and C. L. Kane *Phys. Rev. Lett.* **100**, 096407 (2008)
- [253] D. Hsieh, D. Qian, L. Wray, Y. Xia, Y. S. Hor, R. J. Cava, and M. Z. Hasan *Nature* **452**, 970 (2008)
- [254] Y. Xia, D. Qian, D. Hsieh, L. Wray, A. Pal, H. Lin, A. Bansil, D. Grauer, Y. S. Hor, R. J. Cava, and M. Z. Hasan *Nature Phys.* **5**, 398 (2009)
- [255] A. Roth, C. Brüne, H. Buhmann, L. W. Molenkamp, J. Maciejko, X.-L. Qi, and S.-C. Zhang *Science* **325**, 294 (2009)
- [256] S. Das Sarma, C. Nayak, and S. Tewari *Phys. Rev. B* **73**, 220502 (R) (2006)
- [257] J. D. Sau, R. M. Lutchyn, S. Tewari, and S. Das Sarma *Phys. Rev. Lett.* **104**, 040502 (2010)
- [258] J. Alicea *Phys. Rev. B* **81**, 125318 (2010)

Curriculum Vitae

Name

Name	Isabella Gierz
Date of Birth	March 24, 1982
Place of Birth	Freiburg im Breisgau, Germany
Nationality	German

School Education

1988-1992	Primary School in Freiburg, Germany
1992-2001	St. Ursula Gymnasium in Freiburg, Germany

University Education

2001-2007	Studies of Physics at the Julius-Maximilians-Universität Würzburg, Germany
2004-2005	Studies of Physics at the Université Joseph Fourier in Grenoble, France

Professional Experience

2005	Trainee at the European Synchrotron Radiation Facility in Grenoble, France; Work on x-ray diffraction topography on single crystal CVD diamonds
2006-2007	Diploma thesis ‘Strukturuntersuchungen an CdSe/ZnSe-Quantenpunkten und Zn(Cr)Se-Halbleiterschichtsystemen mit Hilfe von oberflächensensitiver Röntgenbeugung’ in the Group of Prof. Eberhard Umbach at the Julius-Maximilians-Universität Würzburg, Germany
2007-2010	PhD Student in the Group of Prof. Klaus Kern at the Max Planck Institute for Solid State Research in Stuttgart, Germany Topic: ‘Investigation of two-dimensional electron gases with angular resolved photoemission spectroscopy’

Publications

I. Gierz, C. Riedl, U. Starke, C. R. Ast, and K. Kern
'Atomic Hole Doping of Graphene'
Nano Lett. **8**, 4603 (2008)

L. Moreschini, A. Bendounan, I. Gierz, C. R. Ast, H. Mirhosseini, H. Höchst, K. Kern, J. Henk, A. Ernst, S. Ostanin, F. Reinert, and M. Grioni
'Assessing the atomic contribution to the Rashba spin-orbit splitting in surface alloys: Sb/Ag(111)'
Phys. Rev. B **79**, 075424 (2008)

I. Gierz, T. Suzuki, E. Frantzeskakis, S. Pons, S. Ostanin, A. Ernst, J. Henk, M. Grioni, K. Kern, and C. R. Ast
'Silicon Surface with Giant Spin Splitting'
Phys. Rev. Lett. **103**, 046803 (2009)

I. Gierz, T. Suzuki, R. T. Weitz, D. S. Lee, B. Krauss, C. Riedl, U. Starke, H. Höchst, J. H. Smet, C. R. Ast, and K. Kern
'Electronic decoupling of an epitaxial graphene monolayer by gold intercalation'
Phys. Rev. B **82**, 235408 (2010)

I. Gierz, B. Stadtmüller, J. Vuorinen, M. Lindroos, F. Meier, J. H. Dil, K. Kern, and C. R. Ast
'Structural influence on the Rashba-type spin splitting in surface alloys'
Phys. Rev. B **81**, 245430 (2010)

I. Gierz, J. Henk, H. Höchst, C. R. Ast, and K. Kern
'Illuminating the dark corridor in graphene: polarization dependence of angle-resolved photoemission spectroscopy on graphene'
arXiv:1010.1618 (2010)

I. Gierz, F. Meier, J. H. Dil, K. Kern, and C. R. Ast
'Tuning the spin texture in binary and ternary surface alloys on Ag(111)'
arXiv:1011.1829 (2010)

Acknowledgements

Many people contributed to the success of the present thesis. I would like to thank

Prof. Klaus Kern for the opportunity to work as a PhD student in his department at the Max Planck Institute for Solid State Research in Stuttgart. I always had everything I needed to do a good job.

Dr. Christian Ast for advice, guidance and many discussions, for taking me seriously and for being a good supervisor and friend.

Dr. Takayuki Suzuki who contributed the STM data.

Dr. Thomas Weitz for the AFM measurements and his great interest in the transport properties of Au-intercalated graphene.

Benjamin Stadtmüller who did an excellent job measuring $I(V)$ -LEED spectra.

Dr. Dong Su Lee, Benjamin Krauss and **Dr. Jurgen Smet** for the Raman experiments, for the successful collaboration on gold intercalation and many fruitful discussions.

Dr. Harmut Höchst for his good mood and incredible sense of humor and for a lot of moral, technical and scientific support during our beamtimes in Madison.

Dr. Hugo Dil, Fabian Meier, Bartosz Slomski and **Prof. Jürg Osterwalder** for a lot of help with the SARPES experiments at the Swiss Light Source in Villigen and the subsequent data analysis, for many patient explanations and a lot of scientific discussions. Dr. Hugo Dil and Fabian Meier contributed the SARPES results in section 4.3.

Dr. Jürgen Henk, Dr. Hossein Mirhosseini, Dr. Sergey Ostanin and **Dr. Arthur Ernst** for the first principles calculations presented in this work, for many discussions and the joint effort to understand what is going on.

Johannes Vuorinen and **Dr. Matti Lindroos** for the $I(V)$ -LEED calculations.

Dr. Ulrich Starke and **Dr. Christian Riedl** for introducing me to the graphene growth on SiC, for the successful collaborations concerning doping and decoupling of epitaxial graphene, for a lot of advice about the $I(V)$ -LEED experiments and many fruitful discussions.

Dr. Christopher Frewin, Christopher Locke, Prof. Stephen Sadow, Dr. Camilla Coletti, Dr. Konstantin Emtsev, Dr. Ulrich Starke and **PD Dr. Thomas Seyller** for high-quality H-etched, Ar-annealed and H-intercalated

graphene samples.

Dr. Chariya Virojanadara for giving me a very patient introduction to the photoemission and sample preparation setup in 7B15.

All the users of the lab in 7B15 for a nice time and friendly atmosphere during work and **Tolga Acartürk** and **Axel Köhler** for their technical support.

Prof. Roland Winkler for many discussions about the origin of the Rashba splitting in graphene.

Everyone in the Emmy-Noether group (Max Assig, Carola Straßer, Fabian Zinser, Dr. Hadj Benia and Dr. Markus Etzkorn) for a great time in Stuttgart.